

**System Tests,
Initial Operation and First Data
of the AMIGA Muon Detector
for the Pierre Auger Observatory**

Dissertation

zur Erlangung des akademischen Grades eines
Doktors der Naturwissenschaften

vorgelegt von

Master of Science Michael Pontz,
geboren am 17. September 1982 in Mainz,

dem Department Physik
der Naturwissenschaftlich-Technischen Fakultät
der Universität Siegen

Siegen, Dezember 2012

Berichte aus der Physik

Michael Pontz

**System Tests, Initial Operation and
First Data of the AMIGA Muon Detector
for the Pierre Auger Observatory**

Shaker Verlag
Aachen 2013

Bibliographic information published by the Deutsche Nationalbibliothek

The Deutsche Nationalbibliothek lists this publication in the Deutsche Nationalbibliografie; detailed bibliographic data are available in the Internet at <http://dnb.d-nb.de>.

Zugl.: Siegen, Univ., Diss., 2013

Copyright Shaker Verlag 2013

All rights reserved. No part of this publication may be reproduced, stored in a retrieval system, or transmitted, in any form or by any means, electronic, mechanical, photocopying, recording or otherwise, without the prior permission of the publishers.

Printed in Germany.

ISBN 978-3-8440-1758-8

ISSN 0945-0963

Shaker Verlag GmbH • P.O. BOX 101818 • D-52018 Aachen

Phone: 0049/2407/9596-0 • Telefax: 0049/2407/9596-9

Internet: www.shaker.de • e-mail: info@shaker.de

Abstract

Investigating the energy region between 10^{17} eV and 4×10^{18} eV for primary cosmic particles will lead to a deeper understanding of the origin of cosmic rays. Effects of the transition from galactic to extragalactic origin are expected to be visible in this region. The knowledge of the composition of cosmic rays strongly depends on the hadronic interaction models, which are applied in the air shower reconstruction. Directly determining the number of muons from an air shower on ground level will improve the precision of the composition measurements by reducing the dependence on the models.

The Pierre Auger Observatory is facing these challenges with an upgrade of the original detector setup. A denser sub-array of water Cherenkov detectors and a dedicated muon detector (MD) array constitute the AMIGA enhancement (Auger Muon and Infill for the Ground Array). Additional fluorescence telescopes constitute HEAT (High Elevation Auger Telescopes).

Seven MD modules have been installed until mid 2012 in a first hexagon at the site of the Pierre Auger Observatory in Malargüe, Argentina. The corresponding readout electronics, and 19 more of these setups, were assembled and tested in Siegen to assure correct functionality. The detectors were incorporated in the trigger structure of the original surface detector (SD) array of the Pierre Auger Observatory and are now taking data synchronously.

In the framework of this thesis, system tests have been developed, a pre-unitary cell (PUC) of seven modules has been successfully operated and their trigger has been synchronised with the SD trigger. First data from the MD have been analysed and have been combined with data from the SD.

Zusammenfassung

Die Erforschung der primären kosmischen Strahlung im Energiebereich von 10^{17} eV bis 4×10^{18} eV wird zu einem tieferen Verständnis ihrer Herkunft führen. Effekte, verursacht durch den Übergang von galaktischem zu extragalaktischem Ursprung der Strahlung, werden in diesem Bereich als beobachtbar erwartet. Die Erkenntnisse über die Zusammensetzung der kosmischen Strahlung hängen dabei stark vom hadronischen Interaktionsmodell ab, welches in der Luftschauerrekonstruktion verwendet wird. Ein direkter Nachweis der Anzahl der Myonen auf Bodenniveau in einem solchen Luftschauer wird die Präzision der Messungen zur Zusammensetzung der Strahlung verbessern, da er die bestehenden Abhängigkeiten von den Modellen reduzieren wird.

Das Pierre Auger Observatorium begegnet diesen Herausforderungen mit einer Erweiterung des ursprünglichen Detektoraufbaus. Ein dichter gesetztes Detektorfeld von Wasser-Cherenkov-Detektoren und zusätzliche, spezielle Myon-Detektoren bilden die AMIGA Erweiterung (Auger Muon and Infill for the Ground Array). Zusätzliche Fluoreszenz-Teleskope bilden HEAT (High Elevation Auger Telescopes).

Sieben Module des Myon-Detektors wurden bis Mitte 2012 in einem ersten Hexagon am Pierre Auger Observatorium in Malargüe in Argentinien installiert. Die dazugehörige Ausleseelektronik, und 19 weitere dieser Systeme, wurden in Siegen zusammengesetzt und getestet um korrekte Funktionalität zu garantieren. Die Module wurden in die Trigger-Struktur des bestehenden Oberflächen-Detektorfeldes eingebunden und nehmen nun Daten in einem synchronisierten Modus.

Im Rahmen dieser Arbeit wurden Systemtests entwickelt, die ersten Module des Myon-Detektors erfolgreich in Betrieb genommen und ihr Trigger mit dem bestehenden Triggersystem synchronisiert. Erste resultierende Daten wurden mit den Daten des Oberflächen-Detektors kombiniert und analysiert.

Gutachter der Dissertation: Prof. Dr. Peter Buchholz
Prof. Dr. Markus Risse

Datum der Disputation: 01. Februar 2013

Contents

1	Introduction	1
2	Astroparticle Physics	3
2.1	Historical Remarks	3
2.2	Cosmic Rays	4
2.2.1	The Energy Spectrum of Cosmic Rays	4
2.2.2	The Knees in the Spectrum	5
2.2.3	The Ankle in the Spectrum	7
2.2.4	The GZK Suppression	8
2.2.5	Composition of Primary Cosmic Rays	8
2.3	Extensive Air Showers	10
2.3.1	A simple Model for Electromagnetic Cascades	10
2.3.2	A simple Model for Hadronic Cascades	11
2.4	Detection Techniques in Astroparticle Physics	13
2.4.1	Array Detectors	13
2.4.2	Cherenkov Detectors	13
2.4.3	Fluorescence Detectors	14
2.4.4	Radio Detectors	14
3	The Pierre Auger Observatory	17
3.1	Introduction	17
3.2	Physics Aims	19
3.3	The Surface Detector Array	20
3.4	The Fluorescence Detectors	22
3.5	The Trigger System	23
3.5.1	SD Trigger	23
3.5.2	FD Trigger	26
3.6	Enhancements of the Pierre Auger Observatory	27
3.7	Results of the Pierre Auger Observatory	32
4	The Muon Detector of the AMIGA Enhancement	43
4.1	Physics Aims of the AMIGA Enhancement	43
4.2	The Muon Detector Array	45
4.2.1	Deployment of the Muon Detector Array	46
4.3	The Muon Detector Modules	47
4.3.1	Scintillator Unit	47
4.3.2	The Photomultiplier Tube	49

4.4	The Muon Detector Electronics	50
4.4.1	The Underground Electronics	50
4.4.2	The Surface Electronics	54
5	System Tests	57
5.1	Test Stand Setup	58
5.2	Configuration of the Microcontroller	61
5.3	Communication via CAN	61
5.4	Configuration of the FPGA	62
5.5	Read and Write Access to Registers of the FPGA	63
5.6	Channeltest	63
5.7	Crosstalk Test	65
5.8	External Trigger Acceptance	66
5.9	Threshold Scan	68
5.10	High Voltage Characterisation	72
5.11	Monitoring Voltages and Temperatures	74
5.12	Temperature Dependence	77
5.13	Triggers to the AMIGA MD Modules	77
5.13.1	Internal Trigger	77
5.13.2	External Trigger	78
5.14	Detector Calibration	82
6	Results	85
6.1	Test Stand	86
6.2	Results of the Full System Tests	88
6.2.1	Channeltest and Crosstalk Test	88
6.2.2	Threshold Scans	89
6.2.3	Monitoring Voltages and Temperatures	92
6.2.4	High Voltage Characterisation	94
6.2.5	Power Consumption of the Electronics	95
6.2.6	Addressing of Individual Channels	96
6.3	Advanced Trigger Tests	97
6.3.1	Event Request Efficiency	97
6.3.2	Local Timestamp Identity in the Trigger Signals	100
6.4	Results of the Detector Calibration	104
6.5	Temperature Dependence of the High Voltage	110
6.6	Combined Analysis of SD and MD Data	113
6.6.1	Datasets and Event Selection for the SD	113
6.6.2	Reconstructed Energy and Arrival Direction of the SD Events	113
6.6.3	Reconstructed Signal Strength in the SD Stations	114
6.6.4	Data Taking Periods of the MD	114
6.6.5	Analysis of the MD Data	115
6.6.6	Event Layout of the MD Data	117
6.6.7	Definition of N_{Trig}	118
6.6.8	Combination of Data	119
7	Conclusions and Outlook	129

Acronyms	133
List of Figures	137
List of Tables	141
Components and Devices	143
List of Software	145
Bibliography	147
Acknowledgements	155

Chapter 1

Introduction

In 2012, the 100th anniversary of the discovery of cosmic rays by Victor Franz Hess is celebrated. One century later, cosmic rays still haven't lost their fascination. They are studied to answer fundamental questions about their origin, their propagation mechanisms, their energy spectrum, and their composition.

With the Pierre Auger Observatory, built in the Pampa Amarilla in Argentina, the largest air shower experiment ever was installed to contribute answers to these questions. Accessing ultra-high-energy cosmic rays (UHECRs) with high statistics was the overall aim of the observatory since the start of data acquisition in 2004. However, during the years, the wish to extend the observed energy range to lower values arose and the enhancements AMIGA (Auger Muon and Infill for the Ground Array) and HEAT (High Elevation Auger Telescopes) were installed. Besides the possibility to compare the results of the Pierre Auger Observatory with those obtained in other experiments, which measure in the low energy region, the precise determination of the composition of cosmic rays becomes possible.

The muon detector (MD) array as part of the AMIGA enhancement will measure the number of muons in an extensive air shower (EAS) on ground level. This observable will serve as a good indicator of the mass number of the primary particle.

A prototype array of MD modules has been developed, tested and installed during the last years. The tests of the readout electronics for this prototype array, a calibration routine, and the analysis of first data recorded synchronously with the existing surface detector (SD) of the Pierre Auger Observatory are presented here.

This thesis is structured in the following way: Chapter 2 gives an overview on the subject of astroparticle physics including a historical review, a discussion of the properties of cosmic rays, the features of EAS and an overview on the different measurement techniques. Chapter 3 introduces the Pierre Auger Observatory with its enhancements and the hitherto obtained results. Special focus is put on the AMIGA enhancement in Chapter 4. The physics aims of the MD array and the setup of the three parts of each MD module (scintillator, photo multiplier tube (PMT) and readout electronics) as well as their operation principle, are described. Chapter 5 introduces the system tests of the readout electronics of the MD modules, the concept of synchronisation with the SD array and the principle of the detector calibration for

an MD module. In Chapter 6, the results of the system tests and of the calibration procedure are presented. A first analysis of data taken synchronously with the SD array and the prototype MD array is described and the results are presented. Observables connected to the signal strength in the two types of detectors are defined and compared with each other. Since particles at ground level are mainly muons to which both, the SD and the MD, are sensitive, a correlation is expected, which could serve as a proof of principle for the new prototype detector array. The thesis ends with conclusions and an outlook on possible further studies and a strategy to proceed from the prototype array to the full MD array in Chapter 7.

Chapter 2

Astroparticle Physics

2.1 Historical Remarks

After the discoveries of X-rays by Wilhelm Conrad Röntgen in 1895 and of radioactivity in 1896 by Henri Becquerel, particle physics evolved quickly. One of the subjects of studies in that time was the conductivity of air e.g. by Julius Elster and Hans Geitel in 1900 and independently by Charles Wilson. In 1903, Ernest Rutherford discovered that shielding an electroscope with non radiating metal reduces the remnant conductivity of air and led to a slower discharging in the measurement device. It was concluded that the shielding was a shielding against radioactivity from certain terrestrial elements [Gru05].

Studies by Franz Linke in 1902 dealt with ionisation measurements at increasing altitudes [Lin04]. These studies already hinted at a cosmic component, which, however, was not yet recognised [Wal12a]. Theodor Wulf, in 1910, climbed the Eiffel Tower with a self-made electroscope, which would soon become a standard device in the young field of cosmic ray physics. It was expected that the rate of discharge would decrease with increasing distance to ground. However, Wulf found the reduction to be much smaller than expected. He concluded that emanations in the atmosphere were responsible. Independent measurements by Albert Gockel [Goc10] and Domenico Pacini in 1910 [Pac10] confirmed the existence of ionising radiation in the atmosphere of altitudes up to 2000 m.

Two years later, Victor Franz Hess set out to even higher altitudes in balloon flights and clearly discovered an increase of ionising radiation with increasing height. Given that the absorption law by Arthur Steward Eve was correct, which was proven by Hess beforehand [Wal12a], the terrestrial component must have thinned out with altitude and he deduced that an additional component of radiation must exist [Hes12]. This “Höhenstrahlung” was confirmed in 1914 by Werner Kolhörster in further balloon-borne experiments at altitudes up to 9000 m [Kol14].

In 1926, Gerhard Hoffmann observed particle multiplication under absorbing layers of lead [Hof25]. As often happens, applying a new measurement technique, in this case nuclear emulsion layers, led to new discoveries. This technique was applied in the following years in many more experiments.

Robert Millikan called the extraterrestrial radiation “cosmic rays”, a term that was

introduced by Elster and Geitel as well as Wulf in the first decade of the century. Millikan found that cosmic rays interact with the atmosphere of the earth creating “secondary particles” [Lon92]. These secondary particles could be verified by Pierre Auger in 1938 [Aug39]. He used spatially separated detectors installed in the Alps, with which he measured signals coincident in time. These signals hinted at extensive air showers, consisting of many generations of secondary particles, passing the detectors. Auger calculated the energy of the primary particle initiating such a shower to be about 10^{15} eV, an energy that was a million times larger than ever observed before. The Pierre Auger Observatory, which the subject of this thesis is closely connected to, is named after him.

After the introduction of the Geiger-Müller counter in 1928 by Hans Geiger and Walther Müller [Gei28] and the coincidence selector by Walther Bothe in 1929, Bothe and Kolhörster proved that cosmic rays consist of charged particles [Bot29]. Two years earlier in 1927, Dimitry Skobelzyn by chance discovered high energetic particle tracks in a cloud chamber [Wal12b]. Jacob Clay demonstrated that the intensity of cosmic rays depends on the geographical latitude in 1927. He concluded that cosmic rays consist of charge particles. East-West studies in the late 1950s moreover showed that cosmic rays are dominated by positively charged particles since an excess from the west was detected, which is due to the bending of the tracks of charged particle in the earth’s magnetic field [Gru05].

Cosmic rays were the only source of high-energy charged particles up to the 1950s when particle accelerators became widely available. Thus, up to that time, new types of particles were only discovered in experiments based on cosmic ray physics. Examples to be mentioned are the positron (e^+), which was discovered in 1933 by Carl David Anderson, or the muon (μ^-), which was discovered in 1936 by Anderson and Seth Neddermeyer. In 1947, Clifford Rochester and George Butler found the “strange” kaons (K^+ , K^- , K^0) and hints of the lambda (Λ). Also in 1947, pions (π^+ , π^-) were found in measurements by Cecil Powell et al., using thick nuclear emulsion layers. The xi (Ξ^-) and the sigma (Σ), discovered in 1952 and 1953 respectively, were more or less the last particles to be detected in cosmic ray experiments before in 1953, accelerator physics arose [Lon92]. Cosmic ray physics shifted its interest to fields which are still subjects of research today: the origin of cosmic rays, their acceleration mechanisms, propagation of cosmic rays in space and in the earth’s atmosphere, the energy spectrum of the primary particles and their composition.

2.2 Cosmic Rays

2.2.1 The Energy Spectrum of Cosmic Rays

All sorts of nuclei of the periodic table constitute the charged part of cosmic rays. The spectrum covers more than 18 orders of magnitude in flux, and 11 orders of magnitude in energy (see Figure 2.1). At several GeV, particles hit the earth with a differential flux of 1000 particles per square metre and second. This flux is reduced to one particle per square metre and year for energies in the PeV region and further to one particle per square kilometre and century for energies above 100 EeV.

Particles in the low energy region, $E < 1 \text{ TeV}$, can still be detected directly and identified in satellite-based or balloon-borne experiments. The low flux at higher energies, $E > \mathcal{O}(100 \text{ TeV})$, on the contrary, requires long measurement periods and large detection areas. This excludes a direct measurement of the cosmic rays above the atmosphere. Instead, they are measured indirectly by the registration of secondary particles produced in extensive air shower (EAS). Those experiments are installed at ground level. While groups of elements can still be resolved in the PeV energy region, a classification of the cosmic rays into light and heavy composition becomes a major challenge at the highest energies [Blu09].

The flux ϕ of particles as a function of energy E can be described by a broken power law

$$\frac{d\phi}{dE} \sim E^{-\gamma} \quad (2.1)$$

with the spectral index γ . The different kinks or features in the spectrum are described with a change in the spectral index. At several 10^{15} eV it changes from $\gamma = 2.7$ to $\gamma = 3.1$, forming the knee in the energy spectrum, and to $\gamma = 3.3$ at around $4 \times 10^{17} \text{ eV}$, forming the second knee. A flattening of the spectrum back to $\gamma = 2.7$ can be observed at the ankle at $4 \times 10^{18} \text{ eV}$. Finally, the spectrum is expected to end at $E_{\text{GZK}} \approx 6 \times 10^{19} \text{ eV}$ [Blu09]. The differential flux of cosmic rays against energy is given in Figure 2.1. All features of the spectrum mentioned above will briefly be discussed in the following sections.

2.2.2 The Knees in the Spectrum

There are different classes of theories that try to explain the knee features in the cosmic ray energy spectrum as it is recorded by different air shower experiments. The first one holds New Physics to account for the feature, whereas the others suppose the knee to be characteristic for the energy spectrum itself, introduced at the source, during acceleration or propagation processes.

In the first instance, it is assumed that a single broken power law, as shown in Equation 2.1, lies behind the observed structure of the energy spectrum. Above a certain threshold energy, the knee energy, a for now unknown interaction process is to take place when the extensive air shower starts to evolve in the atmosphere. This mechanism is meant to transfer parts of the primary energy into channels whose results can not be detected by current detectors on earth. Hence, the experiment would underestimate the primary energy. This would lead to a steepening of the observed spectrum starting at the threshold energy. Possible candidates for this kind of undetected interactions and particles might be provided by supersymmetric extensions of the Standard Model (SM) of particle physics [Ber12] and are therefore related to New Physics [Kaz01]. Those processes depend on interaction cross sections, which itself depend on the energy per nucleon E/A . A possible dependence of the position of the knee on E/A would thus verify the theory.

If the underlying acceleration mechanism in space is a diffuse shock acceleration [Gru05], and if the origin of particles lies within the Galaxy, the maximal attainable

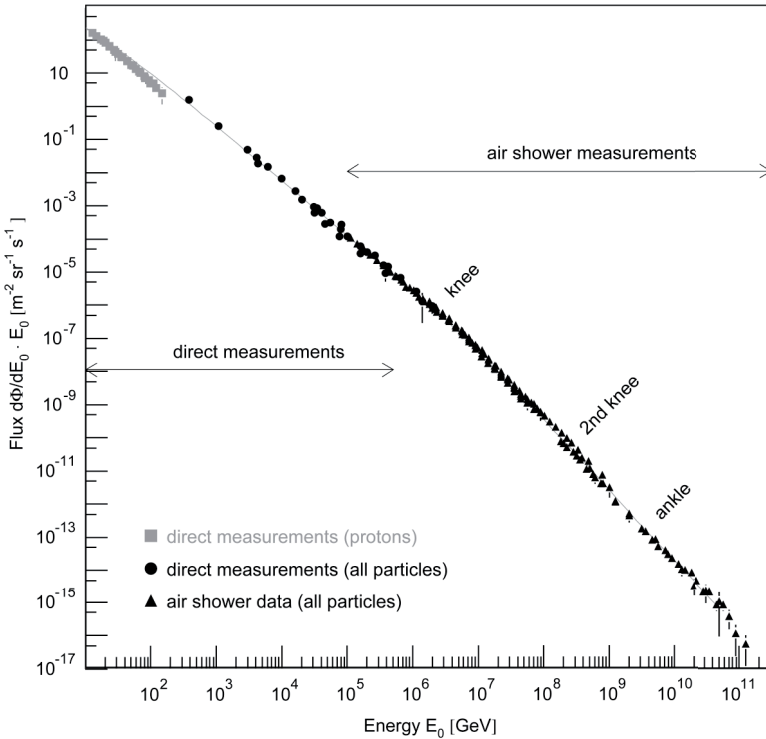


Figure 2.1: All-particle energy spectrum of cosmic rays as measured directly with detectors above the atmosphere (satellite and balloon-borne) and with ground based air shower detectors; direct measurements of primary protons are shown for low energies [Blu09].

energy is limited to a few PeV and is dependent on the charge Z of the particles. Thus, the position of the knee is specific for an element with charge Z [Kob08].

Another theory tries to explain the knee as a propagation effect. The presence of magnetic fields within our Galaxy is undoubted. Although the structure of the fields is not well known, their strength is assumed to be about $\approx 3 \mu\text{G}$. The existence of the fields leads to deflections of charged particles on their way through space. Dependent on their atomic number, the bending radii of ions differ. In a simple assumption, the Larmor radius r_L of a particle with charge number Z in a constant magnetic field B can be estimated as

$$r_L \approx 1.08 \text{ pc} \frac{E/\text{PeV}}{Z \cdot B/\mu\text{G}}, \quad (2.2)$$

which might approach and finally exceed the thickness of the galactic disk, which is in the order of 1 kpc, at those energies where the knee is observed. With increasing energy, protons are no more confined to the Galaxy and some of them will escape. The same happens to heavier elements, where the escape energies scale with the

charge numbers of the elements. The sum of those individually reduced fluxes models the all-particle flux and the knee feature at 10^{15} eV. If all particles have reached their escape energies, most of the galactic component of the charged component of primary cosmic rays will no more interact with the earth. This energy can be calculated to range around 10^{17} eV and could thus be associated with the second knee [Blu09].

Another explanation superimposes a featureless energy spectrum with the signature of a single, near, and relatively young supernova remnant. The local acceleration affects primaries up to the mass of oxygen, which is the reason why the knee structure would be formed mainly by the CNO group, i.e. of carbon, nitrogen and oxygen nuclei [Erl97].

However, results from the current air shower experiment KASCADE-Grande support the theory that the reduced abundance of certain light nuclei in the primordial spectrum causes the knee feature. It is observed that the knee position changes with the type of the primary particle and that it starts with a hydrogen component [Ant05, Kam04]. More statistics is needed to obtain higher precision results.

2.2.3 The Ankle in the Spectrum

In order to explain the ankle feature, basically two models exist. Common for both models is the assumption that high-energy cosmic rays can only originate in extragalactic regions of our universe since no strong source is known within our Galaxy and the confinement conditions can no more be fulfilled.

The first model is referred to as the galactic/extragalactic transition model. It proposes that an extragalactic, proton dominated spectrum overtakes a galactic, iron dominated spectrum at the ankle region. Thus, the overall spectrum would flatten due to the transition. The prediction of this model is almost independent of the composition of the extragalactic cosmic rays [All07, You07].

The second model is the pair production dip model. It describes the attenuation of protons while travelling through the intergalactic space caused by interactions with the cosmic microwave background (CMB):

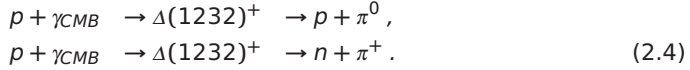


The pair production dip causes the flattening of the overall spectrum in a range up to 40 EeV, given that the assumption is true, that the transition from extragalactic and galactic cosmic rays ranges around the second knee [Ber07a]. A pure proton composition for the extragalactic cosmic rays and a maximum energy of the galactic component of about 10^{18} eV is needed by this model to explain the data [All07].

The second model predicts a dramatic change to protons in the composition of cosmic rays. The first model requires a mixed composition at the extragalactic sources to lie behind the ankle and is in better agreement with most of the current experimental data [All07].

2.2.4 The GZK Suppression

In 1966, the suppression of the cosmic flux at energies of about 10^{20} eV was predicted by Kenneth Greisen, Georgiy T. Zatsepin and Vadim A. Kuzmin [Gre66, Zat66]. Protons in the primordial cosmic radiation interact with photons of the cosmic microwave background to produce photo-pions in processes like



These processes can take place if the centre of mass energy of the system $p + \gamma_{CMB}$ is sufficient to create the delta resonance $\Delta(1232)^+$. The decay of the neutral pion into two photons, $\pi^0 \rightarrow \gamma\gamma$ can result in high-energy photon showers on Earth, Greisen-Zatsepin-Kuzmin (GZK) photons.

Several experiments, namely the Fly’s Eye Telescope [Bir94] at low statistics, the High Resolution Fly’s Eye Experiment (HiRes) [Abb08, Sok10] in a reconfirmation of earlier measurements, and the Pierre Auger Observatory [Abr08a, Abr10a] have already confirmed these predictions.

2.2.5 Composition of Primary Cosmic Rays

The abundance of elements in cosmic rays is in good agreement with the abundance of elements in the solar system (see Figure 2.2). This leads to the conclusion that particles in cosmic radiation originate from processes of nucleosynthesis as it betides in the sun.

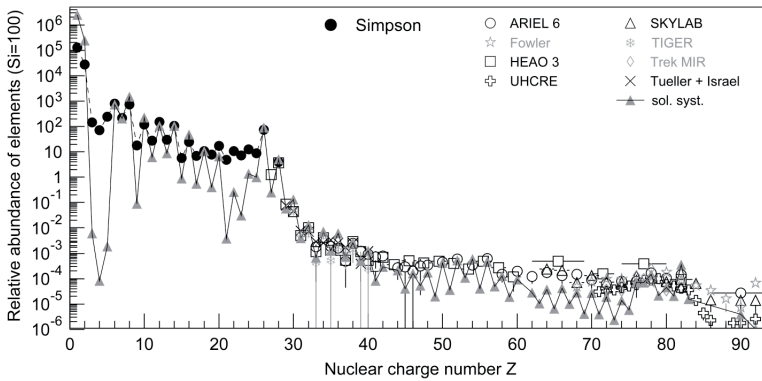


Figure 2.2: Abundance of elements in primary cosmic rays as a function of their nuclear charge number Z at energies around 1 GeV/n, normalised to silicon [Blu09].

Hydrogen and helium ($Z = 1, 2$) need comparably large energies for ionisation, which for this reason will happen less frequently. Since most of the acceleration mechanisms act on charged particles only, the uncharged fractions of hydrogen and helium can not reach the earth and can therefore not appear in the cosmic ray composition.

Overall, an excess of light elements is visible. It can be deduced, that this is due to spallation processes of heavier elements from the carbon/nitrogen/oxygen group, with $Z = 6/7/8$, up to iron or lead, with $Z = 26, 82$, during their journey through space [Blu09].

However, the composition of primary cosmic rays is well-known only up to some 100 TeV, since only for that energy range, direct measurements can be performed. Higher primary energies require indirect measurements through air shower experiments, which offer size and running time in reply to the low particle flux (compare Section 2.2.1). Composition analysis of the primary particles then becomes a result of reconstruction procedures which itself depend on hadronic interaction models. These interaction models were established and verified in collider experiments and then extrapolated to the needs and energies of astroparticle physics. Predictions about composition tend to become unreliable since they depend on the assumptions made for the extrapolations. Figure 2.3 shows the energy spectrum of primary cosmic rays as measured by different experiments and the centre of mass energies of collider experiments. The astrophysical spectrum exceeds these energies by orders of magnitude. However, the extrapolated hadronic interaction models appear to describe the data well.

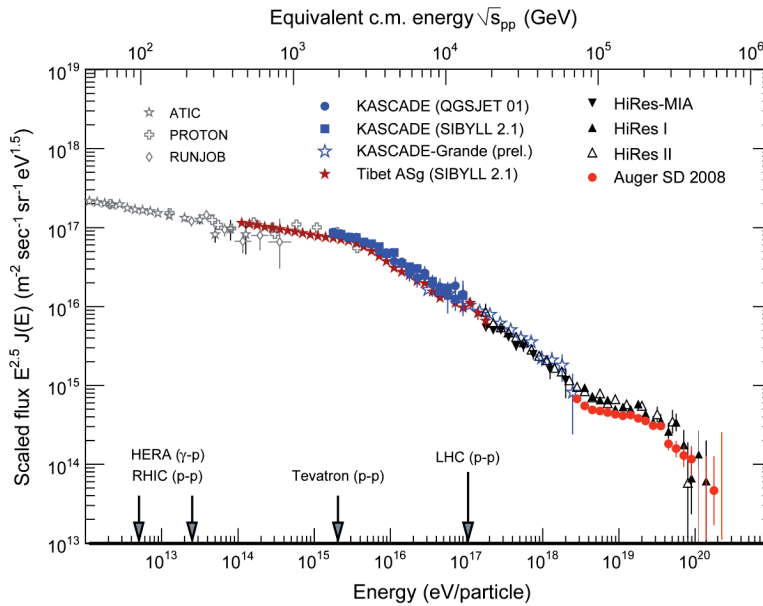


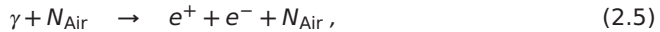
Figure 2.3: All-particle cosmic ray energy spectrum as obtained by direct measurements above the atmosphere (ATIC, PROTON, and RUNJOB) as well as results from air shower experiments (KASCADE - interpreted with two different hadronic interaction models QGSJET 01 and SIBYLL 2.1, KASCADE-Grande, Tibet, HiRes-MIA, HiRes and Auger). Centre of mass energies of selected collider experiments are given for comparison [Blu09].

2.3 Extensive Air Showers

2.3.1 A simple Model for Electromagnetic Cascades

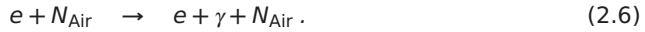
Looking at the flux of cosmic particles, it becomes clear that every experiment, which is to study primaries at more than $\approx 10^{14}$ eV, would suffer from low statistics if it was located above the atmosphere. Due to the low flux, an investigation on particles in these energy regions is only possible with large detection areas. A cosmic ray particle will interact with the atmospheric molecules and initiate a particle shower of which parts will reach the earth. These secondary particles can then be measured and conclusions can be drawn about the primary particle. It is therefore essential to have precise knowledge of the processes that happen inside a particle cascade. Applying a simple model, going back to a publication by Jehangir H. Bhabha and Walter Heitler [Bha37], the observables of an EAS shall qualitatively be derived in the following (compare [Gru93] or [Lon92]). Assuming that the primary cosmic ray is either a photon or an electron, hadronic interactions are of minor importance and for simplicity reasons will be neglected completely for now. Thus, this section concentrates on a pure electromagnetic cascade.

In the field of an atmospheric nitrogen atom, which is needed for momentum conservation, the cosmic photon γ may perform electron-positron pair production in



where the assumption holds that the energy E_γ is distributed in equal parts E_e to the two leptons in Equation 2.5. Since particles are created, the reaction is said to describe the first generation of particles in the air shower.

The two leptons now travel through the air and are finally deflected in the Coulomb field of another nitrogen atom and emit bremsstrahlung:



Again, it is assumed that the initial energy, now E_e , is distributed in equal parts to the products e and γ in Equation 2.6.

The radiation length X is introduced as a density independent quantity for the average distance that an electromagnetically interacting particle can travel in matter. It is defined as the distance of travel through the material in which the energy of a high-energy electron is reduced by a factor of e by bremsstrahlung. The radiation length of electrons in air is $X_{\text{brems}} = 36.62 \text{ g/cm}^2$ [Ber12]. For simplicity reasons, the interaction length of all photons in the cascade, meaning the distance of travel through the material before performing pair production, is set to $X_{\text{pair}} = X_{\text{brems}} \equiv X_0$. Thus, new particle generations will be produced at distinct distances of multiples of $X_0 \cdot \ln 2$. The cascade will grow until the single particle energy in a new generation is reduced to a critical energy E_c . For electrons, it means that ionization dominates over bremsstrahlung and Compton scattering overcomes pair production for photons. The number of particles has now reached its maximum N_{max} after k generations. Each particle has the energy E_c as N_{max} th part of the initial energy E :

$$E_c = E/N_{\text{max}} \Leftrightarrow N_{\text{max}} = E/E_c, \quad N_{\text{max}} = 2^k. \quad (2.7)$$

Equation 2.7 reveals the direct proportionality between N_{\max} and the primary particle energy E . Another observable can be derived from that model: the depth X_{\max} of the shower maximum, which is approximately k times the distance of travel $X_0 \cdot \ln 2$ following Equation 2.7:

$$X_{\max} = k \cdot X_0 \cdot \ln 2 = \ln \left(\frac{E}{E_c} \right) \cdot X_0 \sim \ln E. \quad (2.8)$$

This reveals the proportionality of this variable, which is an observable of dedicated telescopes, to $\ln E$. The 24 telescopes of the fluorescence detector of the Pierre Auger Observatory are built to detect air showers by nitrogen fluorescence from excited atoms in the atmosphere. The amount of light, that is produced per unit track length, is proportional to the amount of particles in that region and can therefore be used to determine both X_{\max} and N_{\max} .

These considerations hold not only for electromagnetic cascades but also for showers initiated by hadrons. It has to be emphasised that the model is not precise and does not account for changing cross sections with increasing energies, which are described by the Landau-Pomeranchuk-Migdal (LPM) effect [Lan53, Mig56], nor for any kind of fluctuations in the processes. Numerical simulations need to be applied in order to gain exactness (compare [Gri10]). However, the model is still well suited to reveal observables of EASs.

2.3.2 A simple Model for Hadronic Cascades

The interaction of a proton or heavier nuclei with atoms in the atmosphere is more complicated, since a variety of secondary hadrons is created while the shower develops. Usually, a large fraction of the initial energy E of a primary proton is given to a single hadron, the leading hadron, in a particle generation. The rest of the energy is distributed to the secondary hadrons, which can be of any kind. These secondary particles themselves will act alike and thus, a hadronic shower evolves. For unstable particles, the two processes, decay to lighter particles and further interaction with the atmosphere, compete. Since pions are the lightest mesons, they will take part in most of the decay chains of heavier hadrons and thus contribute the main content of the hadronic part of the air shower. A simplified model will be described here to derive those shower observables which are used in this thesis (compare [Mat01, Mat05]).

It is assumed, that there is no leading hadron and, further, that the product hadrons are exclusively pions (π^\pm, π^0). The ratio of charged pions to neutral pions is assumed to be to 2:1. The neutral pion π^0 will only decay via

$$\pi^0 \rightarrow \gamma\gamma. \quad (2.9)$$

The charged pions π^+ and π^- only decay through

$$\pi^- \rightarrow \mu^- + \bar{\nu}_\mu \quad \text{and} \quad \pi^+ \rightarrow \mu^+ + \nu_\mu. \quad (2.10)$$

Since charged pions have a long lifetime compared to neutral pions (2.6×10^{-8} s compared to 8.7×10^{-17} s [Ber12]), it is likely, that the π^\pm will interact before the decay. Every interaction results in additional charged pions as long as the energy of the first pion is larger than a threshold energy E_π , for which the interaction probability dominates the decay probability. In air the threshold energy is $E_\pi \approx 100$ GeV ([Gru05]). The

hadronic interaction length is X_h , resulting in a new generation of pions every $X_h \cdot \ln 2$. The pion multiplicity m defines the number of secondary pions per interaction. The muon from the pion decay has a lifetime of 2.2×10^{-6} s. It does not couple to the strong interaction and therefore can travel distances in the range of kilometres. Thus, hadron initiated air showers will result in muons at ground level. If it is assumed, that all muons reach ground level, the amount of muons N_μ at ground, equals the maximum number of charged pions N_π . It is reached, once the single particle energy equals the threshold energy E_π :

$$N_\pi(\text{j-th generation}) = \left(\frac{2}{3}m\right)^j, \quad (2.11)$$

where j is the number of pion generations. The initial energy E_p is distributed to all pions in equal parts, meaning that $E_\pi = E/m^j$. The number of pion generations j can thus be calculated by

$$j = \ln\left(\frac{E}{E_\pi}\right) / \ln m \quad (2.12)$$

and N_μ can be obtained as

$$\begin{aligned} \ln N_\pi = \ln N_\mu &= j \cdot \ln\left(\frac{2}{3}m\right) = \ln\left(\frac{E}{E_\pi}\right) / \ln m \cdot \ln\left(\frac{2}{3}m\right) \\ \Leftrightarrow N_\mu &= \left(\frac{E}{E_\pi}\right)^\beta, \quad \text{with } \beta = \ln\left(\frac{2}{3}m\right) / \ln m \end{aligned} \quad (2.13)$$

The higher the energy of the incoming proton, the larger the amount of muons at ground level. Assuming e.g. $E = 10^{19}$ eV, $m = 50$ and $\beta = 0.9$, this results in around 10^8 muons.

Heavier nuclei with A nucleons can be considered as a superposition of A proton showers each given the energy E/A . That leads to the muon number at ground level

$$N_\mu = A \left(\frac{E/A}{E_\pi}\right)^\beta = A^{1-\beta} \left(\frac{E}{E_\pi}\right)^\beta. \quad (2.14)$$

From the principle of superposition, it can be concluded directly that the first interaction of a heavier primary particle is located higher up in the atmosphere than that of a proton, assuming the same energy per nucleon. Thus, also the location of the shower maximum X_{\max} , being the position at which the number of particles in the shower starts to decrease, is located higher up. Hence, X_{\max} serves as an observable to composition analysis.

Giving up the assumption that all muons reach ground, the decay channels in Equation 2.15,

$$\mu^- \rightarrow e^- + \bar{\nu}_e + \nu_\mu \quad \text{and} \quad \mu^+ \rightarrow e^+ + \nu_e + \bar{\nu}_\mu, \quad (2.15)$$

have to be taken into account. Thus, the hadronic part of an air shower feeds the electromagnetic part with low energy electrons.

From Equation 2.14, it becomes clear that determining the muon number N_μ at ground level experimentally is a very good handle for a composition analysis of the primary cosmic rays, given that the energy is derived by another measurement. Therefore, the Auger Muon and Infill for the Ground Array (AMIGA) enhancement of the Pierre Auger Observatory is aiming at determining the muon number with high precision.

2.4 Detection Techniques in Astroparticle Physics

The low flux of high-energy primary particles limits a direct measurement to low statistics. Having several particles per square metre and second still at 10^{10} eV, the flux reduces to one particle per square kilometre and year for 10^{15} eV and further to less than one particle per square metre and century at primary energies above 10^{19} eV. Therefore, large detection areas for secondary particles are needed. There are basically four types of detection techniques that are applied in astrophysical experiments: scintillator or Cherenkov detector arrays, Cherenkov detectors, fluorescence detectors and, as a comparably new branch, radio detectors.

2.4.1 Array Detectors

High-energy primary particles initiate secondary particle cascades, which spread widely at ground level. Thus, a coarse-meshed array of detectors suffices to measure charged secondary particles, which are mostly originating from the electromagnetic component of an air shower. The coverage of the detection area may be below 1 % for primary radiation from the PeV-regime and onwards [Blu09]. Plastic scintillators (sc.) and water Cherenkov tanks (Ch.) have proven adequate in various experiments such as the Akeno Giant Air Shower Array (AGASA) (sc.), the Karlsruhe Shower Core and Array Detector (KASCADE) (sc.), the Michigan Muon Array (MIA) (sc.), the Sydney University Giant Air Shower Recorder (SUGAR) (sc.), the Volcano Ranch (VR) (sc.), the Yakutsk array (sc.), Haverah Park (Ch.) and in the Pierre Auger Observatory (Ch.). A brief description of these experiments can be found in [Ber07b].

2.4.2 Cherenkov Detectors

The creation of Cherenkov light in EASs is only possible because charged particles travel almost at the speed of light. Around 30 % of them emit Cherenkov light in forward direction with an aperture angle of about 1.3° , related to the refraction index of air. Most of the charged particles in an air shower are electrons. These have a relatively low Cherenkov threshold, which consequently means that most Cherenkov light originates from them. The drawback of the light exploiting technique is the need for a dark background in moonless nights and a clear sky. Therefore, the duty cycle is around 10 %. Light detection through the atmosphere also requires very good knowledge of the atmospheric conditions. This is the reason why e.g. the Auger Collaboration operates several weather stations.

Basically two types of Cherenkov detectors are being used: integrating and imaging detectors. While the former consist of an array of photomultipliers coupled to light connecting cones and looking upward in the sky, the latter are using mirrors and a camera with segmented read-out [Blu09]. The observables for integrating detectors are the energy of the primary particle, which can be calculated from the total amount of collected light, and the mass of the primary particle, which is derived from the distribution of Cherenkov photons along the shower axis. Light integrating detectors were e.g. applied in the Airshower Observation By angle Integrating Cherenkov Counters (AIROBICC), the Broad Lateral Non-imaging Cherenkov Array (BLANCA) in coincidence with the Chicago Air Shower Array (CASA) or in the Cherenkov detector

array close to lake Baikal in Siberia.

Imaging atmospheric Cherenkov detectors, however, produce a focal plane image of an EAS. Geometric properties of the footprint of the air shower and the total intensity of Cherenkov light are measured. The arrival direction of the primary particle and the longitudinal profile can be drawn from these observables. Composition information are connected to the total intensity of the collected light. Since most of the shower parameter reconstruction is based on geometric analysis, the results are almost independent from numerical simulations. The High Energy Stereoscopic System (H.E.S.S.), the Major Atmospheric Gamma-ray Imaging Cherenkov Telescopes (MAGIC) and the Very Energetic Radiation Imaging Telescope Array System (VERITAS) are present representatives of this technique [Blu09].

2.4.3 Fluorescence Detectors

At energies above approximately 10^{17} eV, particles in EASs can excite nitrogen molecules in the atmosphere, whose de-excitation leads to the emission of fluorescence light in the violet and ultra-violet wavelength range from 300 to 400 nm. The de-excitation of the excited states takes place after approximately 10 ns, so almost instantaneously. Light is emitted isotropically. Knowing the fluorescence yield, which is the amount of photons produced per unit of deposited energy, is essential for a precise determination of the primary particle energy. There are hints that the fluorescence yield is independent on the energy of the exciting particle. Therefore, the technique provides a calorimetric measure for the energy, with the atmosphere as detection medium. On the other hand, the fluorescence yield is dependent on atmospheric conditions. For the same reasons, that were mentioned for the Cherenkov telescopes, the duty cycle of fluorescence detectors is as well limited to about 10 %. For a complete reconstruction of a shower profile, this technique requires the determination of the geometry of the shower axis, of the Cherenkov light fraction, and the knowledge about the atmospheric absorption of light. The shower detector plane can be calculated directly from the recorded image, the angle of the shower axis with respect to the detector is derived from the arrival time distribution of the incoming light. The angular uncertainty in the determination of the arrival direction of the primary particle can be improved by about one order of magnitude to less than 1° when moving from monocular to stereo observation with two distinct telescopes. Alternatively, the telescope can be combined with an independent detector in a hybrid experiment. The Fly's Eye experiment, its successor, the High Resolution Fly's Eye (HiRes), the Pierre Auger Observatory and the Telescope Array (TA) have decided to exploit the fluorescence detector technique [Blu09].

2.4.4 Radio Detectors

A relatively new technique exploits electromagnetic waves emitted by EASs in the radio band from approximately 30 to 80 MHz. The emission is mainly caused by the geosynchrotron mechanism: charged particles travel through the magnetic field of the earth and undergo an acceleration by Lorentz force, thus, they radiate. Another reason is the Askaryan effect, which describes the behaviour of EASs in dense media and explains a coherent superposition of radio waves or microwaves from the charge

excess of charged secondary particles [Ask65]. Starting at several hundred PeV, the radio technology might complement the established methods starting at energies of 10^{17} eV. The Cosmic ray Detection Array with Logarithmic Electro-Magnetic Antennas (CODALEMA), the Low Frequency Array (LOFAR), the LOFAR Prototype Station (LOPES) within the KASCADE-Grande experiment or various enhancements at the Pierre Auger Observatory, see Section 3.6, investigate the detection of air showers by radio emission [Blu09].

Chapter 3

The Pierre Auger Observatory

Originally, the Pierre Auger Observatory was designed to consist of two sites, one on the northern and one on the southern hemisphere. At the time this thesis was written, the southern part was finished and is taking data. Due to the lack of funding, the future of a northern site was not yet clear. Unless otherwise stated, the term Pierre Auger Observatory will always refer to the southern site in the following.

3.1 Introduction

The Pierre Auger Observatory is located near the city of Malargüe in the west of Argentina in the Province of Mendoza. It is placed in the Pampa Amarilla, a flat semi-desert area, at an altitude ranging from 1340 m to 1610 m. The absence of local elevations allows for a good wireless communications to the different autonomous detector stations. An altitude between 1000 m and 1500 m is required to optimally observe an air shower development in the atmosphere. Minimal light pollution and, at most times, dry and stable weather conditions, ensured by the closeness to the Andes mountains, are the basis for a good performance of the fluorescence telescopes [All08]. The Pierre Auger Observatory was planned and constructed as a hybrid detector to study the arrival direction distribution, energy spectrum and mass composition of cosmic rays at primary particle energies larger than 10^{19} eV [All08, Abr10c]. Initially, the observatory consisted of two types of detectors: the fluorescence detector (FD), exploiting the technique of measuring light from de-exciting nitrogen molecules in the atmosphere due to a passing extensive air shower (EAS) at ground level (see Section 2.4.3), and the surface detector (SD), consisting of more than 1600 water Cherenkov detector stations, which measure secondary particles of such an air shower (see Section 2.4.2).

Meanwhile, additional types of detectors were added, either for refining the given measurement programme (see Auger Muon and Infill for the Ground Array (AMIGA) and High Elevation Auger Telescopes (HEAT) in Section 3.6) or to explore new detection techniques such as measuring in the radio or microwave band (see Auger Engineering Radio Array (AERA) and further enhancements in Section 3.6). In combination with the initial detectors, these additions result in a more and more powerful tool for astrophysical particle research.

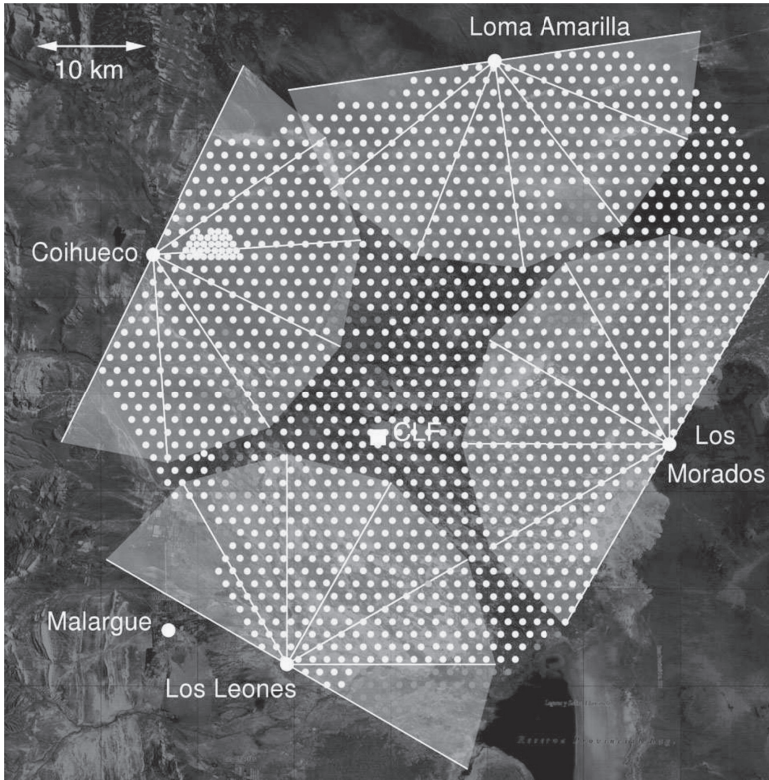


Figure 3.1: Status of the Pierre Auger Observatory near the city of Malargüe as of March 2009. Gray dots show the positions of SD stations: light gray shades indicate deployed detectors, while dark gray defines empty positions. Light gray segments indicate the fields of view of the 24 fluorescence telescopes, which are located in four buildings at the perimeter of the surface array. Also shown is a partially completed infill array near the *Coihueco* building and the position of the CLF, indicated by a white square [Abr10b].

3.2 Physics Aims

The first cosmic ray particle with an energy about 10^{20} eV has already been detected in 1962 by John Linsley with the Volcano Ranch (VR) station [Lin63]. Almost 50 years after this discovery, many questions on the highest energy cosmic rays remain still unanswered. The Pierre Auger Observatory is addressing these open question. The physics programme of the experiment contains

- the measurement of the energy spectrum of ultra-high-energy cosmic rays (UHECRs) with energies above 10^{20} eV,
- the determination of the chemical composition of the primary cosmic rays as they reach the atmosphere of the Earth,
- the identification of sources of UHECRs in the sky,
- and the clarification on the acceleration and propagation mechanisms.

The nature of UHECRs with energies above 10^{20} eV can not yet be explained sufficiently. The Greisen-Zatsepin-Kuzmin (GZK) suppression, which results from the interaction of primary protons with photons of the cosmic microwave background (CMB) (see Section 2.2.4), requires sources comparably near to our Galaxy. Otherwise, the GZK effect would have affected particles at those high energies already farther out in space. The Pierre Auger Observatory is to give a high statistics measurement on cosmic rays in this part of the energy spectrum with an energy resolution better than 20 % and also determine the distribution of the arrival direction with an angular accuracy better than 1° . Given that the full Auger detector would have been built (including the foreseen northern site with 3000 km^2 detection area), up to 1000 events with $E > 10^{20}$ eV could have been detected within 10 years. This calculation is made under the assumption that the broken power law as found at 10^{19} eV persists for another decade in energy.

The composition of primary cosmic rays is not yet fully understood at the highest energies. This includes the flux of cosmic neutrinos and photons. Measuring the depth of the shower maximum, the ratio between the muonic and the electromagnetic component in a shower and the spread of the particle arrival time will help answering this open question. Building the Pierre Auger Observatory as a hybrid detector allows for measuring many parameters of a particle shower independently and thus renders possible cross checks and cross calibrations of the detectors, which increases the accuracy.

The determination of the arrival distribution of cosmic rays allows for answering the question whether UHECRs are distributed isotropically over the sky or not. Again, both sites are necessary for that survey, since e.g. radio galaxies, which might be candidates for UHECRs, are anisotropically distributed around the supergalactic plane, which is only partly in the field of view of a single site. It might become possible to identify regions in the sky from which a majority of UHECRs originates. These regions could be associated to regions that host objects which are remarkable in another sense already, like active galactic nuclei (AGNs). Anisotropy can only be determined at energy regions above 10^{19} eV, since the structure of the interstellar magnetic fields

is not well known. Thus, high energy particles still point to their sources as their path is not bended much by the fields. It will also be possible to learn about the structure of the magnetic fields farther from our Galaxy. Ongoing isotropy at increasing energies on the other hand favours those theoretical models that associate e.g. topological defects or gamma ray bursts with the cosmic rays at the highest energies. The verification or falsification of acceleration and propagation mechanisms comes within reach [Cro97].

3.3 The Surface Detector Array

More than 1600 water Cherenkov detectors constitute the SD array of the Pierre Auger Observatory. These stations measure the secondary particles of the air shower at ground and thus sample its lateral density distribution. They are set up in a triangular grid with a spacing of 1500 m covering more than 3000 km². The spacing results in an energy threshold of 3×10^{18} eV for a primary cosmic ray particle above which the trigger efficiency is at 100 % [All08, Abr10c].

Additionally, station pairs and station triplets have been installed. Under the assumption, that in a close distance of only a few metres the physical content of an air shower at ground level is the same, differences in the measured signals can be ascribed to station-to-station signal fluctuations and can therefore be studied. Station pairs are set up in a distance of only 11 m, triplets build up a triangle of that spacing.

Nearby the *Coihueco* FD building, additional 61+24 SD stations were deployed, filling a finer grid of 750 m and 433 m, respectively. These stations constitute the infill array belonging to the AMIGA enhancement and will be further described in Section 3.6 [Etc10].

Exemplarily, the SD station *Voldemort* is shown in Figure 3.2. Twelve tons of ultra-pure water are filled in a cylindrical plastic tank of 3.6 m in diameter and 1.6 m in height. Ultra-pure water is used in order to achieve the lowest possible attenuation for the ultra-violet Cherenkov light and to ensure a low-maintenance operation for about 20 years. The filling level is approximately 1.2 m, which is sufficient to absorb about 85 % of the incident electromagnetic shower energy at core distances larger than 100 m. The water is sealed in an outer liner made of polyvinyl chloride (PVC) with a diffusively reflecting inner surface. Three photo multiplier tubes (PMTs), orientated downwards into the water, are mounted on the upper side of the tank. They are arranged in a triangular manner, 1.2 m from the center of the tank, and collect parts of the Cherenkov light that is sent out by highly energetic particles from an EAS which penetrate the water volume. Each PMT measures about 23 cm in diameter [All08]. A solar panel is installed on top of each SD station to charge two batteries inside the battery box, which is located at the southern side of the tank to lie in its shadow. Thus, the operation of the station is assured during day and night. The batteries distribute the power to the SD electronics, which consists of front end board (FEB) and the unified board (UB). The electronics is hosted in the electronics dome to achieve protection from harmful influences like weather or animals. The electronics controls the PMTs, performs a first analysis of the PMT pulse shapes (by digitising them using a ring buffer of 1024 positions [Con10] and a 10-bit flash analogue-to-digital converter (FADC) at a sampling rate of 40 MHz for each pulse), and generates

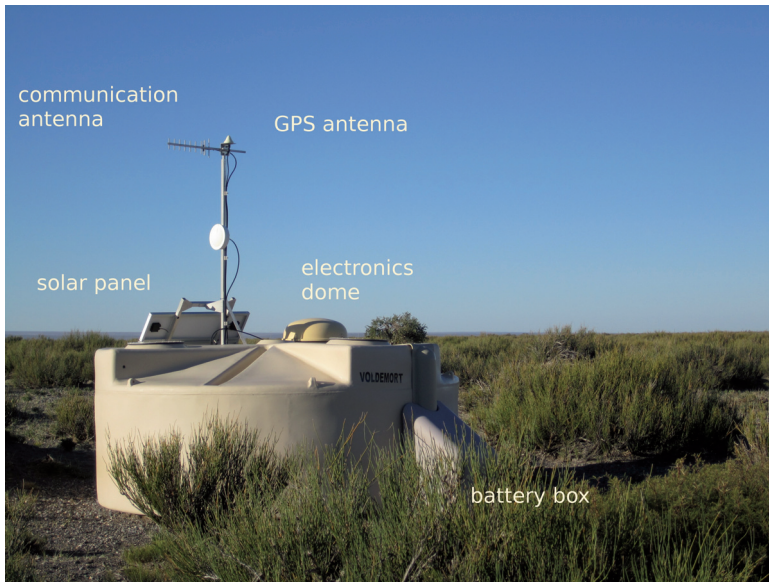


Figure 3.2: Image of the SD station *Voldemort* with explanatory labels applied: the electronics dome, the battery box, the GPS antenna and the communication antenna are clearly visible, image: April 2011.

the first level triggers T1 and T2 (see also Section 3.5) [Abr04]. Communication with the Central Data Acquisition System (CDAS) of the office building of the Pierre Auger Observatory, located in Malargüe, is achieved via a radio link. Hence, all SD stations operate stand-alone [All08].

With the signals measured in the stations of the SD array, information about the causative EAS are reconstructed. For a detailed discussion of the reconstruction see [Veb09, All06].

The signal-weighted barycenter of the individual stations is used to calculate a first estimate for the impact point of the shower core on ground. Similarly, the weighted bary-time is set as initial estimate for the time of impact. The signal times or times of trigger of the individual stations, which participated in the recording of the event, are used to determine an estimate of the direction of the shower axis. Hence, the azimuthal angle φ of the arrival direction is computed. The shower front is assumed to be a plane front moving at the speed of light over the array in these assumptions. The reconstruction is later refined by assuming a curved shower front as part of an expanding sphere.

The determination of the energy of the primary particle of an EAS requires a model for the lateral dependence of the signals $S_{LDF}(r)$ in the stations. Equation 3.1 expresses the model for the signal for the regular SD grid in the 1500 m spacing:

$$S_{LDF}(r) = S_{1000} \times f_{LDF}(r), \quad (3.1)$$

where S_{1000} is the signal strength at a distance of $r_{opt} = 1000$ m from the shower

axis and $f_{LDF}(r)$ is the normalised parametrisation of the lateral density function (LDF) with $f_{LDF}(1000\text{ m}) = 1$. The signal strength S_{1000} is basically separated from the angular dependence in the model. For the normalised LDF, a modified NKG function (Nishimura, Kamata and Greisen) [Kam58, Gre56] as given in Equation 3.2 is used:

$$f_{LDF}(r, \beta, \gamma) = \left(\frac{r}{r_{opt}} \right)^\beta \times \left(\frac{r + 700\text{ m}}{r_{opt} + 700\text{ m}} \right)^{\beta+\gamma}, \quad (3.2)$$

with $r_{opt} = 1000\text{ m}$.

A minimum likelihood minimisation is used to find the best values for the fit parameters S_{1000} , β and γ and thus to completely determine $S_{LDF}(r)$ for the measured shower.

Due to geometrical effects and the attenuation of shower particles at larger zenith angles Θ , the average value for S_{1000} decreases with increasing Θ . Assuming an isotropic flux over the full range of values for the zenith angle, a correction is applied to the quantity S_{1000} using a constant intensity cut method and the zenith angle independent quantity S_{38° is obtained. S_{38° may be regarded as the signal S_{1000} , that the shower would have, if it had arrived with a zenith angle of $\Theta = 38^\circ$. This is the average zenith angle under which events are recorded. It is therefore chosen as a reference angle.

The FD exploits a calorimetric method to measure the energy E_{FD} of a shower. Hybrid measurements, i.e. recording events synchronously with both the SD and the FD are used to find the relation between S_{38° and E_{FD} . The data are well described with the relation given in Equation 3.3.

$$\lg(E_{FD}/\text{eV}) = A + B \times \lg S_{38^\circ}, \quad (3.3)$$

with A and B derived from data [Rot08]. Equation 3.3 is now used to determine the energy of a showers measured solely with the SD array. The quantities S_{1000} and S_{38° , as observables of the SD, are therefore said to be energy estimators for the primary particles of EAS.

For data of the infill array, the reference signal is chosen as S_{450} , being the signal strength at a distance of $r_{opt} = 450\text{ m}$ from the shower axis, the normalisation is $f_{LDF}(450\text{ m}) = 1$ to account for the reduced grid size and the fit parameter γ is set to zero. The zenith angle independent energy estimator becomes S_{35° [Mar11].

3.4 The Fluorescence Detectors

Four telescope stations are installed on small hills at the edge regions of the SD (compare Figure 3.1), overlooking the full SD array. Each telescope station consists of six Schmidt telescopes [Sch32] with a field of view of $30^\circ \times 30^\circ$ in azimuth and elevation [Abr10b]. The telescopes measure the nitrogen fluorescence emission in the atmosphere, induced by an EAS. The amount of fluorescence photons, with wavelengths ranging between 300 nm and 400 nm, is proportional to the energy deposited in the atmosphere due to electromagnetic energy losses of charged particles. Thus, through measuring the emission as function of the atmospheric depth X , the longitudinal development profile $dE/dX(X)$ is determined. By integration, the total electromagnetically dissipated energy can be obtained. It constitutes about 90 % of the

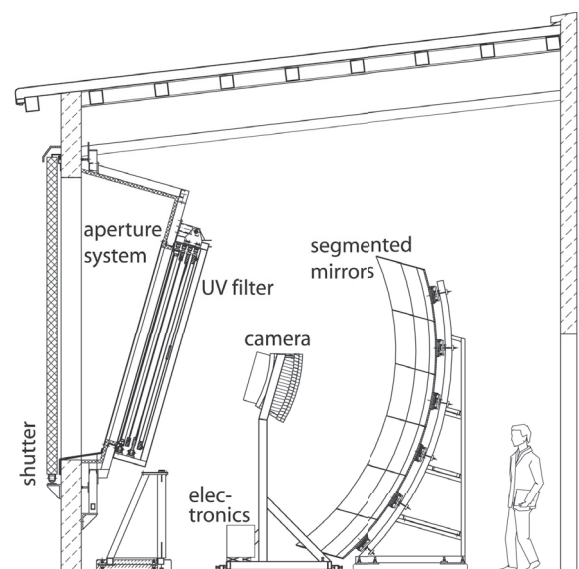


Figure 3.3: Schematic view of the optical system of the FD telescopes [Abr10b].

primary particle's energy. However, the fluorescence yield, which is the number of photons emitted in a certain wavelength band per unit energy loss, varies with the atmospheric variables temperature, pressure and humidity. Atmospheric monitoring is therefore essential to the telescope measurements (see e.g. [Ben09]).

Figure 3.3 illustrates the setup of the optical system. Light enters the diaphragm and a corrector lens and is then reflected by the mirror, with a total area of 13 m^2 and a radius of curvature of 3.4 m , and focused to the camera $\approx 1.7\text{ m}$ apart. In order to improve the signal-to-noise ratio in the fluorescence band of nitrogen, an ultra-violet transmitting filter is installed at the aperture system allowing only photons from 290 nm to 410 nm to pass. Corrector lenses are applied around the diaphragm to account for optical aberrations and to increase the collection area of the telescope.

The camera hosts 440 hexagonal photomultiplier tubes [19] in a $22\text{ rows} \times 20\text{ columns}$ matrix. The spectral band is in the ultra-violet range from 350 nm to 450 nm . Light collectors increase the effective detection areas of the PMTs. Further electronics is dedicated to the trigger mechanisms and are therefore described in Section 3.5.2.

3.5 The Trigger System

3.5.1 SD Trigger

The trigger system of the SD array is a hierarchical system. The first two levels, T1 and T2, are generated at the SD station itself. Combinations of T2 triggers from different stations constitute the third level trigger T3, which is formed at the CDAS. T3 triggers

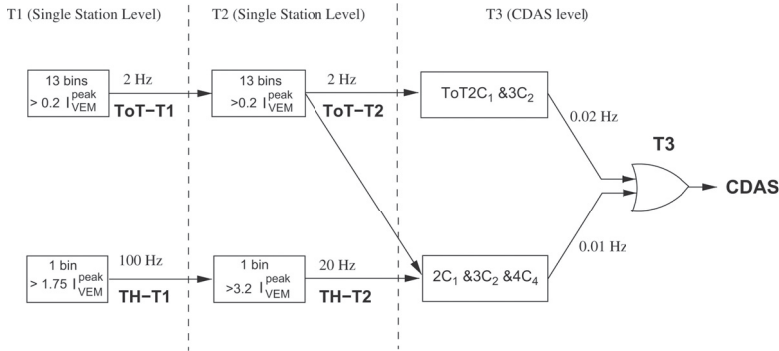


Figure 3.4: Trigger system hierarchy of the SD of the Pierre Auger Observatory [Abr10c].

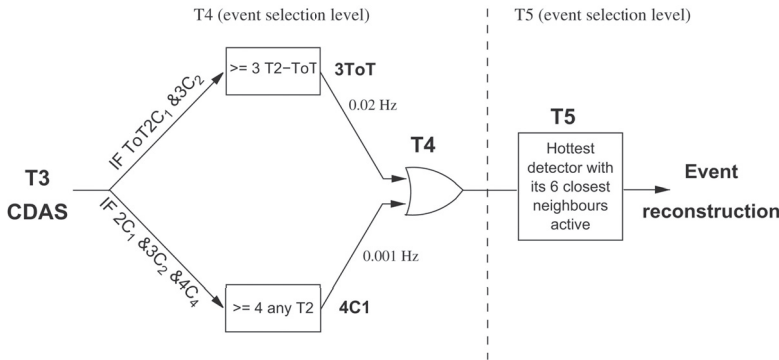


Figure 3.5: Event selection hierarchy of the SD of the Pierre Auger Observatory [Abr10c].

then initiate data acquisition and storage. The structure of the SD trigger system is shown in Figures 3.4 and 3.5 and will be described in more detail in the following sections (see also [Abr10c]).

SD Triggers at Detector Stage

A T1 trigger can be generated in two modes (compare Figure 3.4): the threshold mode T1-TH and the time-over-threshold mode T1-ToT. The peak current I^{peak} of the PMTs is measured in units of vertical equivalent muons (VEMs). A VEM is defined by the signal of a vertical impinging muon to the tank and results in a current of $I = 1 I_{\text{VEM}}^{\text{peak}}$. The T1-TH requires a coincident signal of all three PMTs of the SD station with peaks above $1.75 I_{\text{VEM}}^{\text{peak}}$ each. The rate of T1-TH triggers is approximately 100 Hz, which is a factor 30 below the rate of impinging atmospheric muons. Very inclined air showers can be detected efficiently with this trigger since they are dominated by muons, which create large but comparably short signals when measured with the PMTs.

The T1-ToT requires signals longer than 325 ns and with an amplitude above $0.2 I_{VEM}^{peak}$ in a sliding window of $3 \mu s$ width and with a coincidence in two of the three PMTs. Single muons can be efficiently suppressed by this condition since on average they create signals with widths around 15 ns. Thus, nearby air showers, which are dominated by the electromagnetic component, or distant, high-energy showers can be detected. The rate of T1-ToT triggers per detector is lower than 2 Hz.

Further reduction of the trigger rate is necessary to filter physics events from noise and to allow for storing the data at all. The T2 trigger refines the previous T1 selection. All T1-ToT triggers are promoted to the T2 level. T1-TH triggers need to fulfill the stronger condition of a peak above $3.2 I_{VEM}^{peak}$ for each PMT signal and with a coincidence in the three PMTs. The rate of T2 triggers is around 20 Hz.

SD Triggers at Array Stage

The next trigger levels (compare Figure 3.5) can only be formed at a superior stage, since their generation requires information of more than one SD station. T2 trigger lists are therefore sent to the CDAS by all stations for evaluation. At this third trigger level of the SD, data acquisition is initiated by T3 triggers. All data, i.e. FADC traces, from SD stations with fulfilled T2 conditions are then requested by the CDAS. In addition, data from detectors that had no T2 but a T1 trigger are also requested as long as their T1 signal arrive within $30 \mu s$ of the T3 signal. Spatial and timing conditions are required to form a T3 trigger. At least three detectors with a T2-ToT trigger need to be in a compact configuration for the first T3 trigger mode. This means that among the triggered stations, one must be in the first crown of stations (C_1) around another one and in the second crown (C_2) of yet another one. Then, the timing criteria are applied: depending on the order of crown (C_n) with respect to the earliest station, all stations must have the T2 within $6+5 \times C_n \mu s$. The sequence of these conditions selects events from which 90 % are real showers. It is therefore a physics trigger. Since it is based on T1-ToT, it is most efficient for air showers at zenith angles θ below 60° . About 1600 events per day from the full SD array are recorded in this way. With four stations of any T2, TH-T2 or ToT-T2, in a less compact configuration, the second trigger mode requires a softer spatial condition. The timing criteria thereafter do not change. Horizontal showers with mostly muonic contents, therefore with narrow time spreads in the PMT signals but with a wide footprint on the ground, can thus be detected. This second T3 trigger mode delivers around 1200 events per day from the full SD array, from which 10 % are real showers [Abr10c].

SD Physics Triggers before Event Reconstruction

The full event reconstruction is only started after two more trigger levels are fulfilled. These additional trigger levels select real shower data from the set of stored T3 data.

Again, spatial and timing conditions are applied. The first T4 mode (3ToT) requires three nearby stations with T2-ToT in a triangular pattern. The times of the signals from these stations need to fit a plane shower front moving at the speed of light. More than 98 % of all events, that have an arrival direction with zenith angle $\theta < 60^\circ$, are selected such. Less than one event per day is chosen by a chance coincidence.

The second T4 mode, 4C1, requires four nearby stations with any T2 trigger. The

timing needs to match a plane shower front at the speed of light. In addition to almost vertical and vertical showers, the more inclined ones are described by this second T4 mode.

In order to remove accidentals from the set of stations before the reconstruction procedure, an initial triangle of non-aligned stations is chosen. The shower arrival direction is calculated from the time information of these stations. Then, it is checked whether all other detectors match the assumption of a plane shower front moving at the speed of light along the arrival direction within ${}_{-2}^{+1} \mu\text{s}$. Besides, all stations with no active neighbours in two crowns are rejected in the further analysis.

Applying event selection and removing accidental stations leads to a set of data for which the reconstruction of arrival direction, core position and the energy estimator does succeed in 99.9 % of all cases.

Corrections of border effects of the SD array is mandatory, since otherwise showers, in this region might be reconstructed with wrong results. The detector with the highest signal needs to be surrounded by six working neighbour stations. Thus, only events that are well-contained inside the array are passed to the reconstruction algorithms.

3.5.2 FD Trigger

Since the muon detector (MD) modules of the AMIGA enhancement are physically connected to parts of the SD stations and do not require information from the FD, the trigger system of the FD shall only be mentioned very briefly in this thesis. It is described in [Abr10b].

Signal driver circuits and high voltage (HV) dividers for the individual PMT of an FD camera are located in one unit, the head electronics (HE). In the HE, the anode signals of the PMT are passed on to the front-end analog board (FAB) of the readout electronics.

A hierarchical trigger system controls the data output. The first level trigger (FLT) board digitises signals from the FAB at 10 MHz and stores data for a later readout. It readjusts the pixel trigger thresholds permanently so that a pixel trigger rate of 100 Hz is secured to account for varying background light situations. In addition, the FLT calculates the pixel multiplicity per PMT column of the camera. The second level trigger (SLT) checks whether the pattern of at least five triggered pixels follows a more or less straight track, by comparison with pattern classes. The SLT then generates internal triggers and attaches Global Positioning System (GPS) timestamps to the pixel events. Further trigger stages are implemented through software in dedicated computers inside the telescope buildings. These computers receive external triggers from the CDAS and then read out and analyse data tagged by FLT and SLT.

The Third Level Trigger (TLT) is an algorithm that is optimised to reject triggers due to lightning or muon impacts on the camera or due to randomly triggered pixels. Lightning events are efficiently rejected by refusing events with more than 25 triggered pixels. Random events with less than 25 triggered pixels are filtered using the correlation between spatial arrangement of the triggered pixels and peak signal times. Up to this stage, about 94 % of all background events are identified by the TLT.

Camera based events associated with the remaining triggers, and thus likely physics events, are merged and combined images of adjacent telescopes are created. A T3 trigger is formed and passed to CDAS. Subsequently, CDAS requests events from the

FD and from the SD. Only those SD stations that are located near the triggering FD are taken into account. These comprise about one quarter of the full SD array. In addition, the SD stations have to have an SD trigger at T2 level around the impact time of the shower as calculated from FD data. This T3 trigger is consequently named hybrid trigger. The energy threshold of the hybrid trigger of approximately 10^{18} eV [Abr11] lies below the trigger threshold of the pure SD.

3.6 Enhancements of the Pierre Auger Observatory

The decision to extend the Pierre Auger Observatory with different enhancements was driven by two arguments: the improvement of the quality of data for energy and mass composition analyses for low energies and the capability to get a handle for an unbiased measurement of $\langle X_{\max} \rangle$. Measurements in the energy region below 10^{18} eV allow for a direct comparison of results with other experiments, e.g. KASCADE-Grande. Detection of coherent radio signals from air showers and the research and development activities in microwave detection complement the enhancements.

AERA

Studies of the mechanisms for radio emission in the frequency band between 10 and 100 MHz, demonstration of the physics capabilities of the radio technique and a measurement of the composition in the ankle region were the physics motivations to build the Auger Engineering Radio Array (AERA). At its present stage, 21 radio detection stations (RDS) have been installed, co-located with the infill detector array and within the field of view of HEAT, and are taking data since March 2011. The detectors are set up in a triangular grid with 150 m spacing. At later stages, up to 160 RDSs will be installed in grids with 250 m and 375 m spacings. Figure 3.6 shows the different stages of the AERA enhancement.

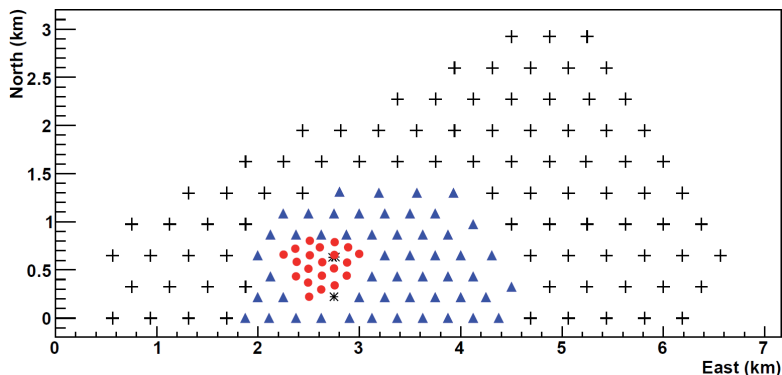


Figure 3.6: Layout of the AERA enhancement at its different installation stages. Stage 1 core stations (red solid circles) were deployed in 2010, expansions (blue triangles and black crosses) will increase the instrumented area to approximately 20 km^2 [Kel11].

A single RDS consists of two log-periodic dipole antennas, one orientated in north-south, the other in east-west direction. The antennas operate between 27 and 84 MHz, which is the quiet region between the shortwave and the frequency modulated (FM) bands. Signals from the antennas enter a low noise amplifier (LNA), which includes a bandpass filter from 23 and 79 MHz to eliminate any intermodulation from the FM band. Further amplification circuits and bandpass filters from 30 to 78 MHz feed 12 bit digitisers with a sampling frequency of 200 MHz. Inside a field-programmable gate array (FPGA), the digitised signals are processed by filter and trigger logics using the time-domain radio signal. Upon the generation of a trigger, data corresponding to $10.2 \mu\text{s}$ is stored for a later transfer to a data acquisition system located in the central radio station (CRS). RDS events are given timestamps, that are generated by on-board GPS receivers. Timestamp information from all RDS is sent to the CRS, which is to check for multi-station events and generate a trigger in case. Once the RDS information fit an expected signal moving over the array at the speed of light, all data from all RDS are requested and written to permanent memory for later analyses. The trigger rate of an individual station ranges at 100 Hz, the multi-station trigger rate is one decade below.

The RDS are powered through a photovoltaic system and rechargeable batteries. Communication with the CRS is achieved via an optical fiber network. This will be changed to a wireless communication system at later stages.

Most of the multi-station events acquired are due to man-made radio signals and need to be neglected for physics data analysis. The rate of coincident events with the SD ranges between 0.3 and 0.9 events per day [Kel11].

AMIGA

The transition region, in which the flux of cosmic rays changes from galactic to extra-galactic origin, is assumed to range between 10^{17} and 4×10^{18} eV. Investigating these energies should enable the discrimination between different theoretical models and is aimed at with the Auger Muon and Infill for the Ground Array (AMIGA) enhancement at the Pierre Auger Observatory. AMIGA consists of two parts, the infill and the MD. It was started together with the High Elevation Auger Telescopes (HEAT) after the completion of the original detector system of the Pierre Auger Observatory in 2008.

The infill is an array of regular water Cherenkov detectors as used in the SD but placed in a triangular grid with a reduced spacing of 750 m and 433 m covering 23.5 km^2 and 5.9 km^2 , respectively. The 433 m infill detector array is planned within the 750 m infill array but has not yet been installed. As of September 2011, all 61 infill stations of the 750 m grid have been deployed. Figure 3.7 shows the efficiency calculations from simulated air showers. The reduced grid sizes will lower the energy threshold for full trigger efficiency for events with at least three stations, that fulfill the time-over-threshold (ToT) requirement to 3×10^{17} eV and 10^{17} eV and thus to one decade below the original thresholds for the 750 m and the 433 m infill array [Mat11]. There are 55 ± 6 events reconstructed with the coarser infill array. Out of these events, 28 ± 3 events pass the fiducial quality cut T5, which requires an event to have one working hexagon around the station with the highest signal.

The angular resolution of the 750 m infill array was calculated to be better than 1° for events with more than six stations corresponding to an energy of 3×10^{17} eV. The

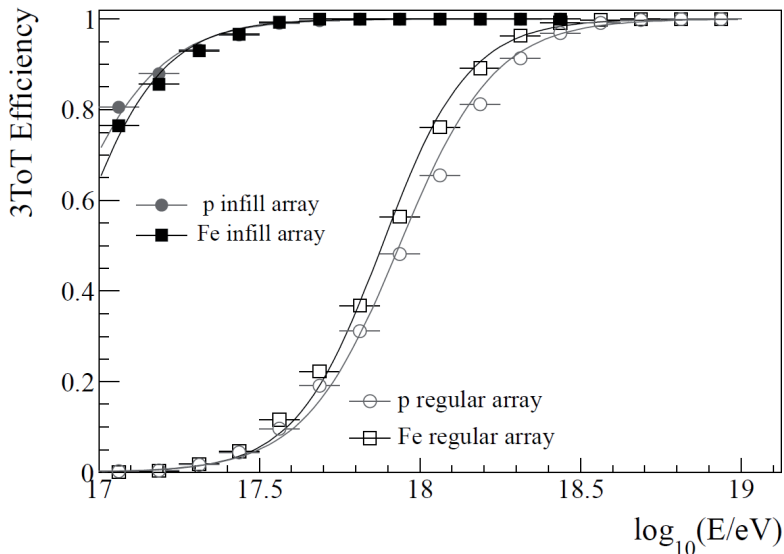


Figure 3.7: The trigger efficiency for the 3ToT trigger for the 750 m infill array and for the regular 1500 m array obtained from simulations of iron and proton primaries. Graphical adaption of [Mar11].

energy estimator for the 750 m infill array was chosen to be S_{450} instead of S_{1000} for the regular array. The S_{450} value is the interpolated strength of the SD stations' signals at a distance of 450 m away from the core of the measured air shower [Mat11].

The subject of this thesis is the MD of the AMIGA enhancement. Therefore, a more detailed description of these detectors is presented in Chapter 4.

HEAT

Low energetic cosmic rays interact earlier in the atmosphere so that part of the event might be missed by the standard FD telescopes. In this case, X_{\max} can be estimated with lower accuracy, since it results from fits rather than from the direct observation of the shower profile. Three telescopes, the High Elevation Auger Telescopes (HEAT), were added to the FD in 2009. They are located near the *Coihueco* FD building, overlooking the extra SD stations of the infill array.

The additional telescopes are constructed similar to the original FD system except for the ability to tilt them upwards by 29° within two minutes. The field of view in tilted mode is approximately $30^\circ \times 40^\circ$. Differences in the mechanical construction are mostly due to the tilt mechanism. The HEAT telescopes are located in individual shelters, each constructed from lightweight walls coupled to a steel structure. They rest on long steel frames with concrete filling. Optical components are connected to this ground plate to avoid vibrations and keep a fix geometry. Mechanical stability is monitored by inclination sensors and by measuring distances between elements within the shelter.

The data acquisition (DAQ) system is an improved version of the standard FD system. The sampling frequency for the PMT pulses was doubled to 20 MHz. The analysis software can combine HEAT data with data from the *Coihueco* FD telescopes to one virtual site. A combined low energy event, as recorded by *Coihueco* and HEAT, is shown in Figure 3.8 [Mat11].

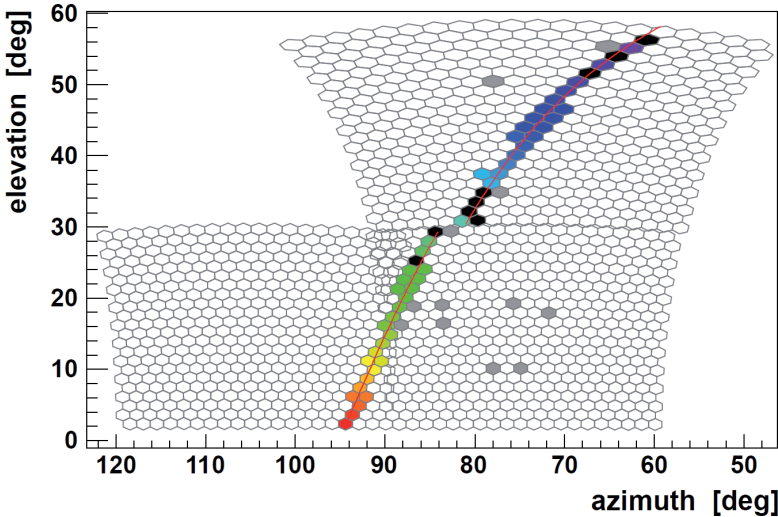


Figure 3.8: Example image of a low-energy event recorded in coincidence with HEAT and two *Coihueco* telescopes. The arrival time of the light is color-coded (blue early, late red). The position of the shower axis is determined independently for *Coihueco* and HEAT. The observable offset between the tracks needs to be corrected for in further analysis. This nearly vertical event with a zenith angle of 19° has a reconstructed energy of about 1.7×10^{17} eV [Mat11].

Microwave Detection

Microwaves emitted by particles in the electromagnetic parts of EASs may be used for a novel detection technique. The low attenuation of microwaves in the atmosphere might enable a duty-cycle of 100 % for the observation of the longitudinal profile of the air shower with microwave detectors. Four experiments at the Pierre Auger Observatory are aiming at proving its viability. The Air-shower Microwave Bremsstrahlung Experimental Radiometer (AMBER), the Extensive Air Shower Identification using Electron Radiometer (EASIER), the Fluorescence Detector Wave system (FDWave) and the Microwave Detection of Air Showers (MIDAS) form the microwave research and development activities within the collaboration.

AMBER is to observe showers in coincidence with the SD array. It is located near HEAT, and shares its field of view, overlooking the infill array. Data taking was underway at the time this thesis was written.

EASIER antennas are installed at two hexagons of the usual SD array. For a prototype phase, stations of one hexagon are equipped with a MHz antenna each, stations in another hexagon carry GHz antennas. The signals of the antennas are adapted to fit the SD electronics FADC input range. Thus, existing structures for the signal processing and event building are used. Data recording has started for the prototype array [All11] and an evidence for a signal in the band of 3.4 to 4.2 GHz from an EAS as recorded in coincidence by the SD was found [Aub11].

The FDWave system uses 264 empty pixels in a camera of an FD telescope at *Los Leones* for the installation of GHz antennas. The FD telescope mirror in *Los Leones* is made of aluminium and is thus reflecting the microwave radiation. Theoretical calculations predict the energy threshold for shower observations to be above 3 EeV. Coincidence measurements with the remaining PMT pixels and FD event reconstruction shall simplify the commissioning of FDWave.

The MIDAS detector is a parabolic reflector with a 53-pixel camera. Standard commercial satellite television low-noise block downconverters with feedhorns are used for the pixels. MIDAS was designed to detect EASs with energies in the EeV region. Candidate events are selected by pixel topology and time coincidence requirements in the MIDAS trigger. Calibration was performed using a calibrated source at the centre of the reflector as well as astronomical sources. A prototype has been working for six months and will be relocated next to the FD telescope *Los Leones* soon [All11].

3.7 Results of the Pierre Auger Observatory

This section summarises which results were already published by the Pierre Auger Collaboration with respect to their physics programme as described in Section 3.2.

Energy Spectrum

In 2008, the Pierre Auger Collaboration published the measured energy spectrum of cosmic rays above 2.5×10^{18} eV. The spectrum was derived from 20,000 events, which were recorded between January 1, 2004 and August 31, 2007. A single power law from $E = 4 \times 10^{18}$ eV to $E = 4 \times 10^{19}$ eV could be rejected with a significance of more than six standard deviations [Abr08a]. An update of this result was given in [Abr10a], which used data until December 2008 and confirmed the previous results at higher statistics. Figure 3.9 shows the measured spectrum with two fit functions adapted: three power laws $E^{-\gamma}$ with different coefficients and power laws combined with a smooth fit function. The ankle is found at $10^{18.61 \pm 0.01}$ eV. The spectral index changes from $\gamma = 3.26 \pm 0.04$ to $\gamma = 2.59 \pm 0.02$. A cut-off is observed at $10^{19.46 \pm 0.03}$ eV. A continuation of the former spectral shape can be rejected with more than 20σ . More details are given in [Abr10a].

This observation is consistent with the GZK cut-off (see Section 2.2.4), which predicts an increase of the spectral index and therefore a steepening of the spectrum in the vicinity of 10^{20} eV [Gre66, Zat66]. However, it may also be caused by the exhausting of the acceleration mechanisms at the sources, which remain unclarified. The measurements of High Resolution Fly's Eye (HiRes) [Sok10] and the Pierre Auger Observatory are in agreement within the systematic energy uncertainties of 22 % [Abr10a].

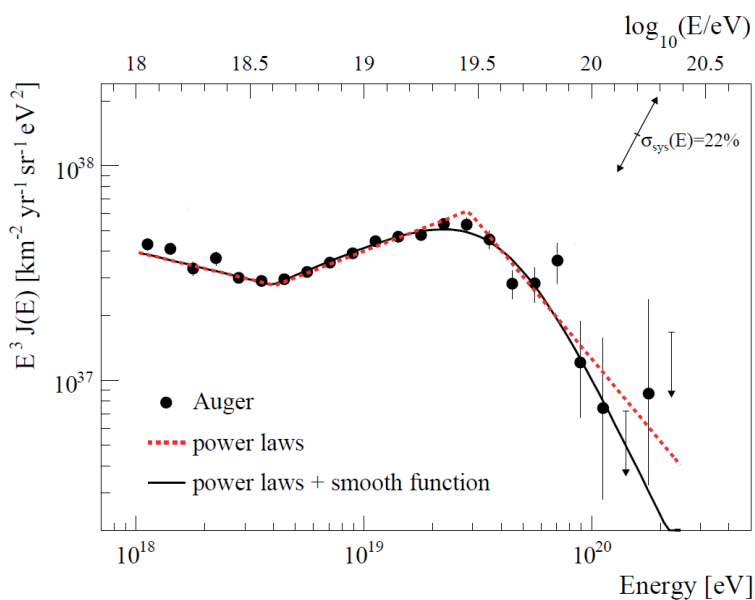


Figure 3.9: Combined energy spectrum as measured by the Pierre Auger Observatory between 2004 and 2008. The spectrum is fitted with two functions (see text and reference). The systematic uncertainty, determined by the uncertainty of 22 % in the energy, is indicated by arrows. The flux is scaled by E^3 to emphasize the structure in the spectrum [Abr10a].

Mass Composition

The depth of the shower maximum X_{\max} is an indicator of the type of primary particle of an EAS (compare Section 2.3). Due to their lower cross section, the first interaction point of a proton will be deeper in the atmosphere than that of a heavier particle. Energy is spent at a slower rate by protons, which means that X_{\max} will increase. Hence, the fluctuations and thus the root mean square deviation (RMS) of X_{\max} , $RMS(X_{\max})$, from shower to shower are larger for protons compared to heavier primaries [Con11].

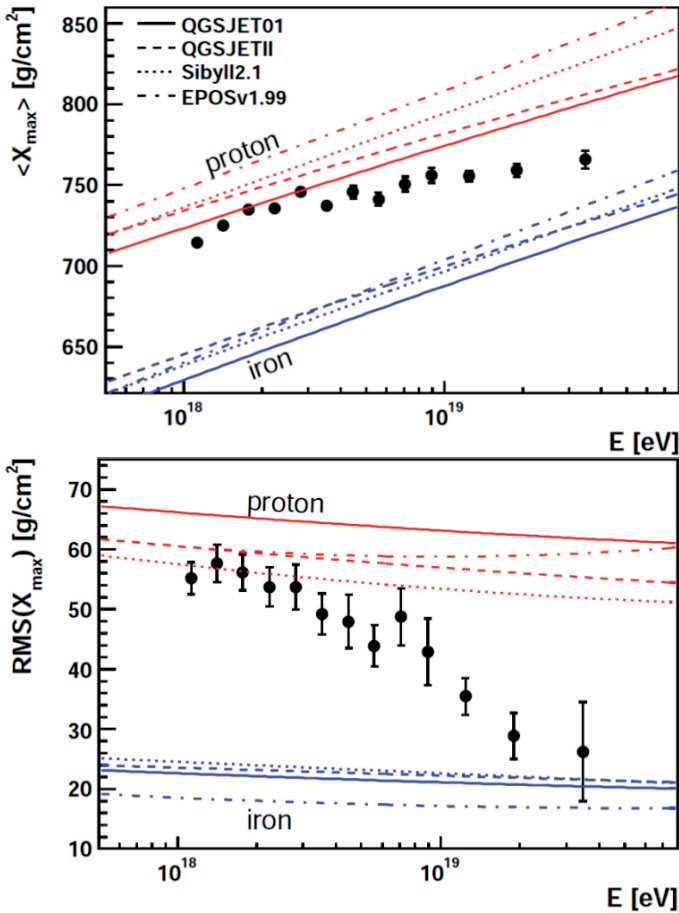


Figure 3.10: Measurement of $\langle X_{\max} \rangle$ (top) and its RMS (bottom) as a function of energy and representations of the predictions of air shower simulations based on different hadronic interaction models [Con11].

Figure 3.10 represents the obtained results for the mean X_{\max} and for $RMS(X_{\max})$ as a function of the energy and the predictions from simulations using different hadronic interaction models. Looking at the measurement of $\langle X_{\max} \rangle$ and of $RMS(X_{\max})$, the

data seem to hint at a transition of primary particles from lighter to heavier elements with increasing energy. However, interpretations like this rely on the hadronic interaction models, which show the same tendencies, but which differ in details. Thus, neither precise interpretations on the composition of the primary particles nor statements on the particular kind of a single primary appear possible.

Up to now, there is no established theory that can fully describe the interaction processes in the high energy regions. Interaction models, therefore, extrapolate accelerator data by several orders of magnitude to the energy range of UHECRs. The number of muons from a shower serves as a test tool for these phenomenological models. However, comparisons with Auger data resulted in an underestimation of the muon number for all interaction models applied [Con11]. The direct measurement of the muon number, which the AMIGA enhancement aims at, will help to clarify that situation.

Anisotropy

In 2007, the Pierre Auger Collaboration published a correlation of $p_{data} = 69_{-13}^{+11}$ % between the incoming direction of observed events above 55 EeV and the positions of AGNs within 75 Mpc distance to Earth from the Véron-Cetty and Véron 12th (VCV) catalogue [Vé12] (Figure 3.11). Eight of 14 events in the Auger data lay less than 3.1° off from an active galactic nucleus (AGN) in the VCV catalogue. For an isotropic distribution of AGNs, 2.9 conformities, corresponding to $p_{iso} = 21$ %, are expected.

The analysis was updated in 2010 using all available Auger data through 31 December 2009 and keeping all parameters. The degree of correlation of $p_{data} = 38_{-6}^{+7}$ % was derived. Conformities with the VCV catalogue in 21 of 55 new events were found, where 11.6 (21 %) are expected for an isotropic distribution [Abr10d]. Another update for data up to June 2011, yields 24 of 84 events in correlation with the entries of the VCV catalogue. The correlation probability reduced further to $p_{data} = (33 \pm 5)$ %. The development of p_{data} with the number of events is represented in Figure 3.12 [Kam11].

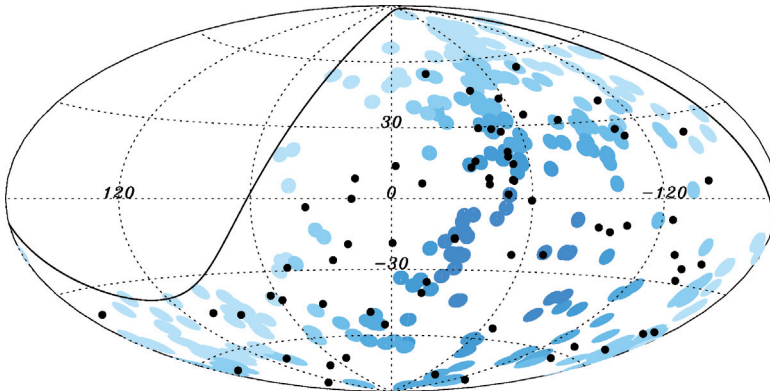


Figure 3.11: The 69 arrival directions of cosmic rays with energy above 55 EeV detected by the Pierre Auger Observatory up to 31 December 2009 are plotted as black dots in an Aitoff-Hammer projection of the sky in galactic coordinates. The solid line represents the field of view of the Pierre Auger Observatory for zenith angles smaller than 60° . Blue circles of radius 3.1° are centred at the positions of the 318 AGNs in the VCV catalogue that lie within 75 Mpc and that are within the field of view of the Observatory. Darker blue indicates larger relative exposure. The exposure-weighted fraction of the sky covered by the blue circles is 21 % [Abr10d].

The arrival directions of high-energy events has also been compared with other catalogues, but common for all analyses is the need for more data in order to increase the significance of the results.

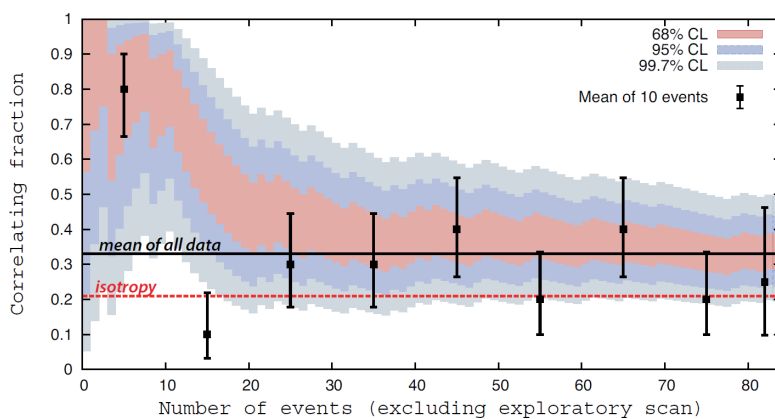


Figure 3.12: The degree of correlation p_{data} is plotted as a function of the total number of time-ordered events for the latest updated dataset up to June 2011. The 68 %, 95 % and 99.7 % confidence level intervals around the most likely value are shaded. The horizontal dashed line shows the isotropic value $p_{iso} = 21$ % and the full line the estimate of the signal $p_{data} = (33 \pm 5)$ %. The black symbols show the correlation fractions bins of independent ten consecutive events [Kam11].

Photon and Neutrino Limits

Photon induced showers are expected to develop deeper in the atmosphere than hadron induced ones. Since photons do not participate in the strong interaction, less secondary muons will be generated, which mostly originate from hadron decays. Therefore, the muon footprint on ground level of such a shower will be more compact [Set11]. Combining the SD observable S_b , as introduced in [Ros11], and the X_{\max} , determined by the FD, in a Fisher analysis, the separation power between proton and photon induced showers is increased. Figure 3.13 shows the scatter plot of X_{\max} vs. $\log_{10}(S_b)$ for simulated showers of primary protons and photons with energies between 10^{18} and $10^{18.5}$ eV. These simulated distributions are used to optimise the analysis to identify photon candidate showers in the Auger hybrid dataset from 2005 to September 2010. For each photon candidate shower, hadron showers with the same energy and arrival direction are simulated. It can be seen that these hadron showers partly result in similar combinations of X_{\max} and S_b .

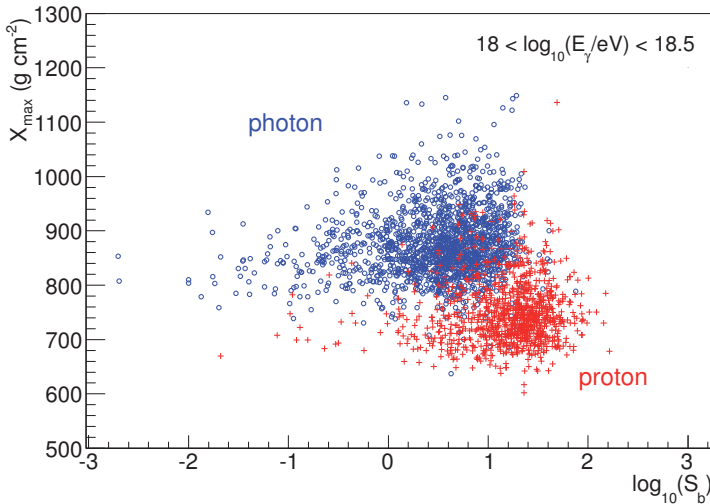


Figure 3.13: Scatter plot of X_{\max} vs. $\log_{10}(S_b)$ for simulated showers of primary protons (red crosses) and photons (blue circles) with energies between 10^{18} and $10^{18.5}$ eV [Set11]. Basically, the curve, onto which the projection of the data points results in the highest separation of the two quantities, is determined in the analysis. Heavier primaries would end up in the lower right corner in this plot. Comparing proton and photon showers is therefore sufficient.

Photon candidates are thus compatible with the proton background. It cannot be stated that single events stem from a primary photon, but however, the upper limit on the photon flux in the cosmic ray flux can be calculated. If ultra-high energy photons exist and reach the Earth, they should contribute less than 0.4 %, 0.5 %, 1.0 %, 2.6 % and 8.9 % (95 % C.L.) to the all-particle flux above 1, 2, 3, 5 and 10 EeV

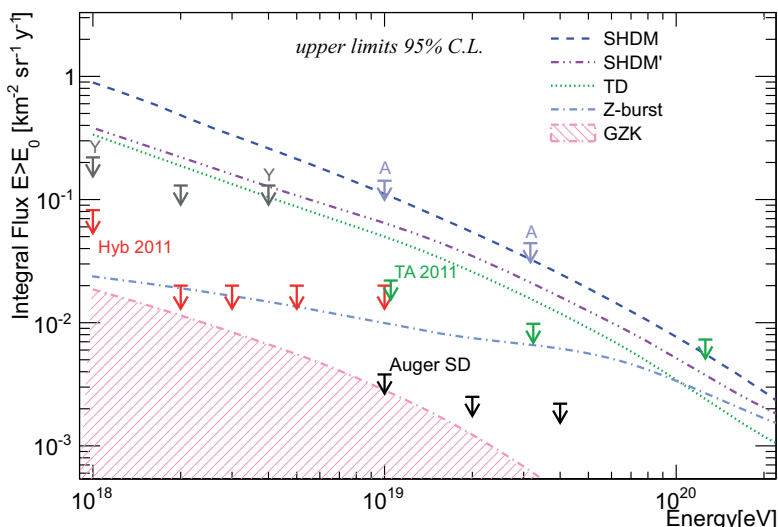


Figure 3.14: Upper limits on the photon flux above 1, 2, 3, 5 and 10 EeV (red arrows) compared to limits from Auger for SD, from AGASA (A) and Yakutsk (Y). The shaded region and the lines give the predictions for the GZK photon flux (compare Section 2.2.4) and for top-down models (TD, Z-Burst, SHDM and SHDM'), respectively [Set11].

[Set11, Set12]. The analysis of higher energy events with hybrid data is impossible yet due to limited statistics. However, the SD array, being fully efficient above 3×10^{18} eV, is used by a similar analysis. This analysis results in photon limits on the flux fraction of 2.0 %, 5.1 % and 31 % (95 % C.L.) for energies above 10, 20 and 40 EeV, respectively [Abr08b]. The photon limits on the flux are shown in Figure 3.14 compared to the expected fraction of GZK photons, results from other experiments and different theoretical models.

Despite the low cross section of weakly interacting neutrinos with matter, they can be detected with the Pierre Auger Observatory for energies above 0.1 EeV. The different mechanisms that can be detected with the observatory are shown in Figure 3.15. Down-going neutrinos enter the atmosphere, they may interact close to ground and create an air shower. Due to this deep interaction, the electromagnetic component has not yet died out when reaching the SD, and will arrive with the muonic component. Thus, these signals in the detectors differ from the ones created by hadron showers. Furthermore, the heaviest of the neutrinos, the τ -neutrino ν_τ , can skim the Earth and interact in the surface. As a result, a τ -lepton might be created, which will then induce a shower. τ -leptons can also be created through interactions in the massif of the Andes for inclined down-going neutrinos coming from the West.

Within exposure-corrected two years of observation with the full SD array, no down-going neutrino event could be found. In data, corresponding to 3.5 years of the full SD in operation, no event could be identified to originate from an Earth-skimming

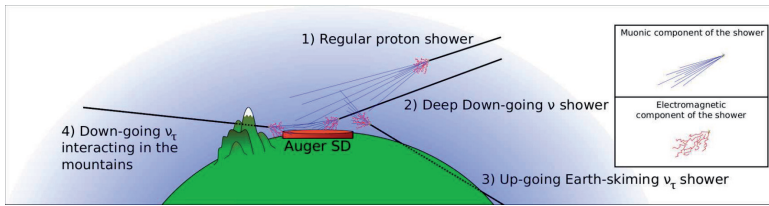


Figure 3.15: Sketch of different inclined showers which can be detected by the Pierre Auger Observatory. (1) An inclined shower induced by a proton interacting high in the atmosphere whose electromagnetic component is absorbed and only the muons reach the detector. Inclined showers presenting significant electromagnetic component at the detector level: (2) a deep down-going neutrino shower; (3) an Earth-skimming tau-neutrino ν_τ shower; (4) and a tau-neutrino ν_τ interacting in the mountains [Gua11].

neutrino. Upper limits on the neutrino flux can be placed and are displayed in Figure 3.16. More data is required to verify or falsify theoretical models [Gua11].

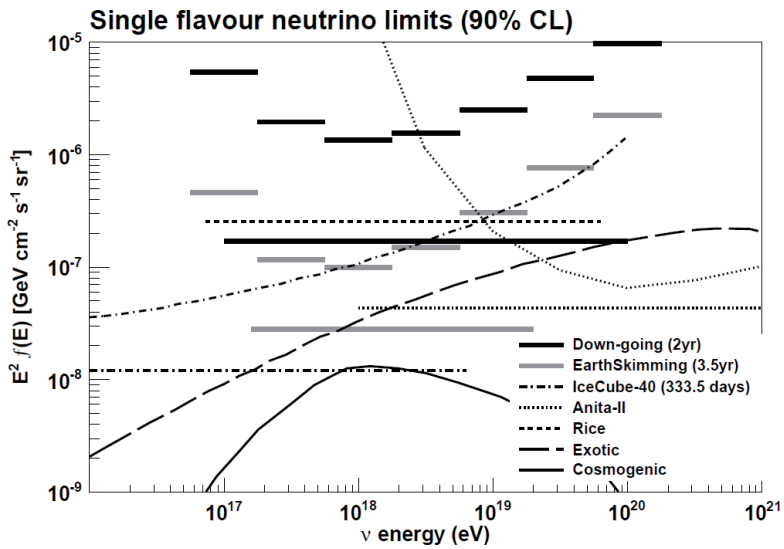


Figure 3.16: Differential and integrated upper limits (90 % C.L.) from the Pierre Auger Observatory for a diffuse flux of down-going neutrinos (two years of full Auger) and Earth-skimming tau-neutrinos (3.5 years of full Auger). Limits from other experiments are also plotted as well as expected fluxes for cosmogenic neutrinos and for a theoretical exotic model [Abr10c].

Chapter 4

The Muon Detector of the AMIGA Enhancement

4.1 Physics Aims of the AMIGA Enhancement

The current lower energy threshold of the Pierre Auger Observatory for measuring cosmic ray events with a 100 % trigger efficiency is 3×10^{18} eV. With the two infill arrays, with 750 m and 433 m grid size, this threshold will be lowered by approximately one decade. The Pierre Auger Observatory will not only become more sensitive to the ankle region in the cosmic spectrum, but it will also see the second knee region and connect to the energy range of the Large Hadron Collider (LHC) at 10^{17} eV. The latter is of great importance since hadronic interaction models are very reliable in these energy regions as they are very well tested by the experiments at the LHC. Furthermore, a comparison, based on high statistics, of the KASCADE-Grande measurements and the energy spectra as measured by the Pierre Auger Observatory will become possible in the overlap region between 10^{17} and $10^{17.5}$ eV [Aug06], compare Figure 4.1. The transition of cosmic rays from galactic to extragalactic sources will be better understood, if the composition in the region between 10^{17} and 4×10^{18} eV can be determined more precisely. Acceleration mechanisms and anisotropy can be studied in more detail [Aug06].

The relevant observables for these studies are the longitudinal profile and the muon number of an extensive air shower. The first observable can be observed directly by the additional fluorescence telescopes, HEAT, the second one is going to be measured exclusively with a new detector array, the muon detector (MD) array of the AMIGA enhancement.

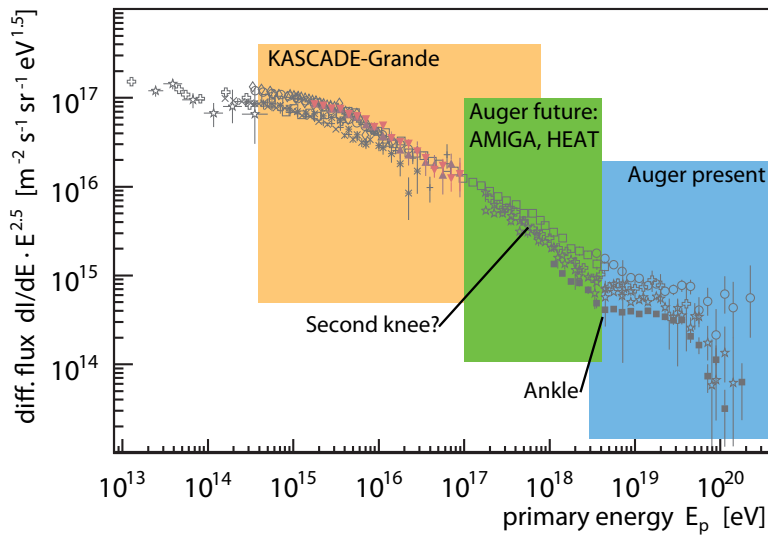


Figure 4.1: Comparison of the energy ranges in the spectrum of primary cosmic rays covered by KASCADE-Grande, the present Auger detector systems and the future Auger enhancements AMIGA and HEAT, graphical adaption from [Kic08] in [Nie11].

4.2 The Muon Detector Array

Each surface detector (SD) station in the infill array shall be accompanied by an associated MD module. Each MD module is located approximately 2.25 m below ground and slightly apart from the SD station in order to avoid a placement in the muon shadow of the station. This shadow is the region in which parts of the muons can be absorbed by the water volume in the tank. A distance of approximately 5 m was found to be sufficient. Simulations have proven, that the different locations of MD module and SD station still represent the same physical position inside the shower front for sharing Global Positioning System (GPS) signals.

A study was presented in [Aug06], in which vertical particle showers with a primary energy of $E = 10^{18}$ eV were simulated to impinge on the Pierre Auger Observatory. At ground level, which corresponds to approximately 874 g/cm^2 of atmospheric depth, mainly γ , e^\pm and μ^\pm arrive. Muons, therein, have a mean energy of 10 GeV compared to 100 MeV for γ and e^\pm at 200 m distance from the shower core. Since scintillators are sensitive to charged particles in general, muons and electrons can not be distinguished and a shielding against the electromagnetic component of an air shower is needed. The MD modules are thus covered with soil, corresponding to 540 g/cm^2 of atmospheric depth. Particles that still pass a MD module at that depth are mostly muons with an energy larger than $\mathcal{O}(1 \text{ GeV})$ at ground level [Nie11]. Punch-through, being the creation of electromagnetic sub-showers in the soil, may lead to a particle cascade hitting the detector, which is contaminating the muon measurements. It was shown in [Aug06], that an installation depth between 1.5 and 2.5 m limits this contribution to below 13 and 5 %, respectively. That way, the muonic component of an extensive air shower (EAS) can be separately measured without contributions from the electromagnetic part and hence, the MD array is sensitive to the composition of the primary particles.

It was shown in [Aug06], that the reconstructed number of muons $N_\mu(600)$ at a distance of 600 m from the shower core constitutes the best parameter to discriminate proton from iron primaries for the given array arrangement. In this study, 50 showers for a primary iron particle and 50 showers for a primary proton particle were simulated. The primaries had an energy of 50 EeV and an incident angle of 45° each. A random change of the core position within the AMIGA array was applied to use one shower 20 times. The detection efficiency of the muon counters was assumed to be 100 %. Effects of pile-up, being the underestimation of the muon number due to the limited amount of channels in the detector, can be corrected with Equation 4.1 later on:

$$N_\mu^{\text{est}} = \frac{\ln\left(1 - \frac{N_\mu^C}{N_{\text{seg}}}\right)}{\ln\left(1 - \frac{1}{N_{\text{seg}}}\right)} \approx -N_{\text{seg}} \ln\left(1 - \frac{N_\mu^C}{N_{\text{seg}}}\right), \quad (4.1)$$

where N_μ^{est} is an estimation of the real number of muons, N_μ^C is the measured number of muons and $N_{\text{seg}} = 192$ describes the number of channels per 30 m^2 MD module. A muon lateral density function (MLDF), following Equation 4.2, is fitted to the sample of discrete muon numbers $N_\mu(r)$. $N_\mu(r)$ is obtained from the individual MDs that were hit by the shower front. The parameter $N_\mu(600)$ is calculated with this continuous

distribution:

$$N_{\mu}(r) = P_0 \left(\frac{r}{r_0} \right)^{-\alpha} \left(1 + \frac{r}{r_0} \right)^{-\beta} \left(1 + \left(\frac{r}{10 \cdot r_0} \right)^2 \right)^{-\gamma}, \quad (4.2)$$

with fixed parameters $r_0 = 320$ m, $\alpha = 0.75$ and $\gamma = 2.93$, leaving P_0 and β as free parameters for the fit. Figure 4.2 shows the distributions of $N_{\mu}(600)$ for the simulated showers. The sensitivity of the observable $N_{\mu}(600)$ to composition becomes visible.

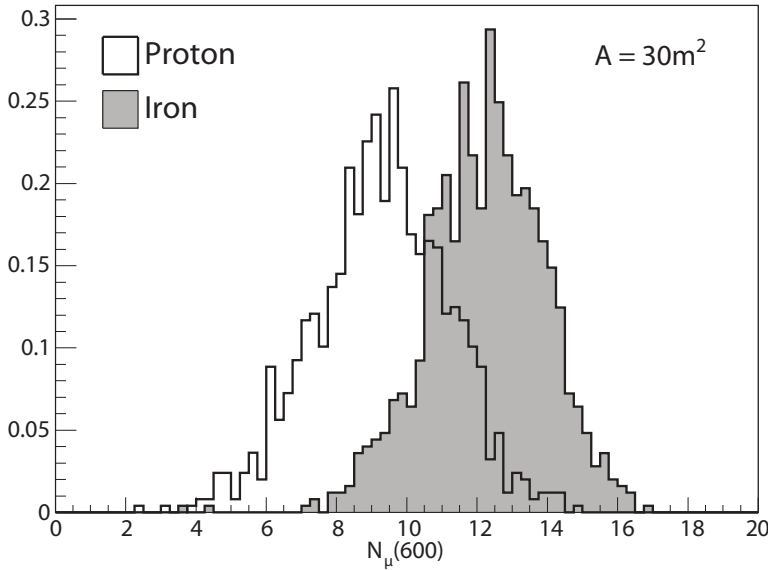


Figure 4.2: Distribution of the simulated and reconstructed number of muons $N_{\mu}(600)$ at a distance of 600m from the shower core for proton and iron primaries for 30 m² MD modules, graphical adaption from [Aug06]. The difference in the mean values in the distributions of this observable represents the sensitivity to composition.

4.2.1 Deployment of the Muon Detector Array

The installation of the MD array has been planned in different stages. The deployment of a single prototype detector with a 5 m² scintillator module at the SD station *Corrientes* was executed in November 2009. The aim was to test whether all logistics worked well and to gain experience with the installation of a MD module at the Auger site, both with respect to mechanical and to electrical aspects. A 10 m² scintillator module followed in August 2010 at the same station, which ended stage zero of the installation. Stage one was the deployment of a single 10 m² module at the SD stations *Heisenberg* and *Phil Collins* in April 2011. Finally, the deployment of the remaining four technically identical modules at the stations *Kathy Turner*, *Los Piojos*, *Toune* and *Yeka* followed as stage two in February 2012. With seven MD modules with a 10 m² scintillator each, a first filled hexagon is currently deployed and constitutes

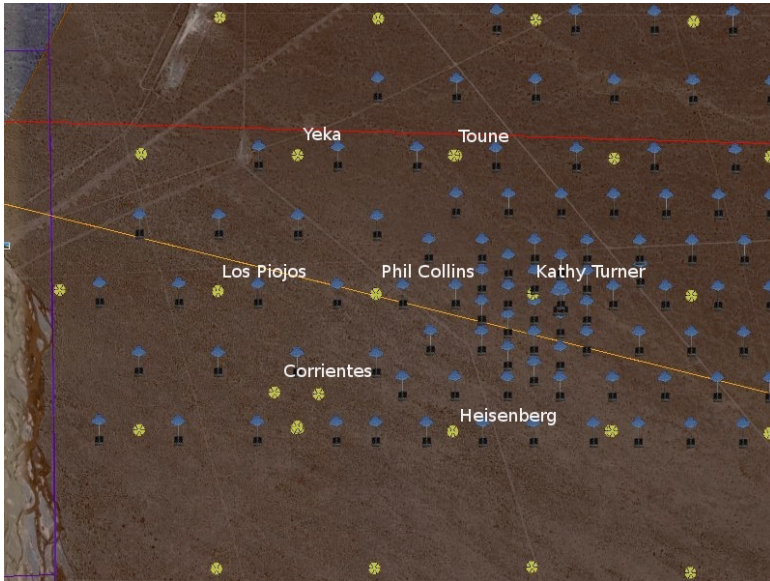


Figure 4.3: Part of the SD infill array. Those tanks that constitute the PUC of the MD array are labeled and the SD station names are illustrated. The distances of the tanks in the triplet at station *Corrientes* are not shown true to scale. The blue items represent detector stations of the AERA detector array. Modified overlay of a satellite picture [Goo11] and the SD station map [Cou11].

the pre-unitary cell (PUC). This thesis will focus on the MD as deployed at this stage. Stage three will be the extension of the MD modules of the PUC in order to have 30 m^2 of scintillators per SD station. It is planned to have two 10 m^2 and two 5 m^2 modules per station. The set of seven 30 m^2 MD modules will be referred to as unitary cell (UC). The last stage, four, will then be the equipment of all the SD stations of the 750 m infill array with 30 m^2 MD modules consisting of three 10 m^2 modules each. Figure 4.3 illustrates the arrangement of the SD stations in the PUC.

4.3 The Muon Detector Modules

4.3.1 Scintillator Unit

Each MD module is constructed from 64 extruded single scintillator strips. The basic design of the strips follows the design of the target tracker detector of the OPERA experiment (Oscillation Project with Emulsion-Tracking Apparatus) [Ada07]. The strips have a rectangular cross section of $41\text{ mm} \times 10\text{ mm}$, a length of 4 m and are made of polystyrene doped with fluorescent chemicals [14]. A reflective layer of titanium dioxide was co-extruded as a coating to improve the light collection. A WLS fibre [21] with 1.2 mm in diameter is glued [20] into a 2 mm deep groove along the scintillator

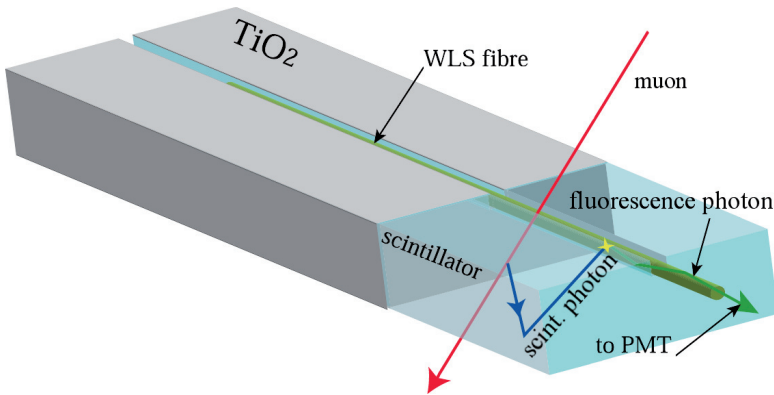


Figure 4.4: Principle of particle detection in a scintillating strip. The trajectories of the impinging cosmic muon (red) and the photons that are produced are drawn. The scintillation process generates a photon with an energy corresponding to a wavelength in the blue region (scintillation photon). Deexcitation of molecules inside the WLS fibres generates a photon with an energy corresponding to a wavelength in the green region (fluorescence photon). Graphical adaption from [Ada07].

strip. Reflective tape covers the fibres. The length was restricted by two factors: the need of mechanical handling of the complete detector and the light attenuation in the fibre. The attenuation length of the fibre was measured to be approximately 6 m [Aug06]. The fibres are blackened on the open end to prevent reflection of light, which could lead to double counting of the same signal. Those fibre ends, which are connected to the photo multiplier tubes (PMTs) are polished with a diamond-bit on a fly cutter [Aug06]. Figure 4.4 shows the detection principle of the scintillating strip. An impinging charged particle generates photons with a wavelength around 400 nm (blue region) in the scintillating material. An average total number of 6 photo electrons was measured for a distance of 4 m of the impinging particle from the fibre end. The energy deposition needed to produce a single photo-electron (SPE) has been measured to be at least 100 keV [Aug06]. The scintillation photon is eventually reflected by the outer titanium layer, enters the fibre and excites molecules in it. By deexcitation of the fibre material, a photon with a wavelength of 492 nm (green region) is generated and will enter the PMT [16], which is attached to the fibre. The PMT produces an electrical signal proportional to the amount of fluorescence photons seen. The maximum light absorption and emission of the fibre range at 410 nm and 485 nm, which matches the PMT. Details on the scintillator production and module assembly can be found e.g. in [Pla11] and [Buc09].

Two groups of 32 scintillating strips are placed at each side of a central dome, which houses the PMT and parts of the electronics. All module casing is constructed from panels of polyvinyl chloride (PVC), onto which the scintillating strips are glued. Stabilising u-profiles are added along the module. Figure 4.5 shows the first MD module during its installation at the SD station *Corrientes* on 25 November 2009. The exca-

vation hole for the 10 m² modules is 3 m wide and 11 m long, with a depth of 2.5 m [Sid12].



Figure 4.5: During the installation of the first 5 m² MD module at *Corrientes*. The yellow scaffold holds the detector in a horizontal position. It is also suited for the 10 m² modules. The dome, which encloses the readout electronics and the PMT, and the u-profiles, that give stabilisation to the module can be seen. Styrene is attached to the module to protect it from the topside. A sand bed of ≈ 20 cm height was prepared for the module to protect it from rocks in the soil below and to ensure a horizontal position. Except for the access tube, which enables maintenance of the PMT and the electronics, the pit was completely filled with soil as the last step of the mechanical deployment; image: November 2009.

4.3.2 The Photomultiplier Tube

In order to convert the optical signals from the scintillator to electrical ones, a 64 multianode PMT [16] was chosen. It is based on an existing type but re-designed specially for AMIGA. The pixels are arranged in an 8 × 8 matrix, each pixel covers an active area of 2 mm × 2 mm.

Some of the features of the PMT are: high speed response with signal rise times of 1 ns, low dark current of less than 2 nA / channel, sensitivity to wavelengths between 300 nm and 600 nm, a quantum efficiency of typically 43 % at the wavelength peak value of 400 nm and a minimum of 20 % at 490 nm, a typical gain of 3×10^5 per channel, a maximal gain uniformity of 1 : 3, and an operating ambient temperature of 0 to 50 °C [16].

Crosstalk is the reaction of a pixel which was not fired. It can originate from two sources. Firstly, light from a neighbouring fibre can enter the pixel, which would result in photo electron peaks. Secondly, the collection efficiency of the dynodes of a channel can be less than 100 % and electrons may enter a neighbouring dynode system. The latter would widen and shift the noise peak of the channel [Ada07, Bor04]. The PMT shows crosstalk at a level of 2 % [16].

A test facility was set up to characterise all PMTs, which will be used in the AMIGA MD array. The main goals of the tests are the determination of the pixel gain, the gain uniformity between pixels, the PMT dark rate and crosstalk, the quantum efficiency and the mean amplitude of the SPEs. Afterpulsing and dependencies on the high voltage (HV) are excluded from the tests. Information on the tests can be found in [Sua09]. Similar tests for this kind of PMTs, which serve as a basis for the current tests, have been done [Bor04] for the OPERA project [Ada07].

The PMT is optically coupled to the 64 fibres. A plastic optical connector was built to guide the fibres onto the PMT pixels [Pla11]. This connector was aligned to the PMT using the method described in [Ada07, Bor04]. By polishing the fibre ends and applying optical grease [22] between the fibre and the PMT window, the coupling quality is improved and reflections are minimised [Pla11].

The PMTs are operated at a HV of 1000 V at the experimental site. Therefore, all PMTs are characterised at that voltage in the tests. The system tests of the electronics, ensure that a HV of 1000 V can be supplied and monitored.

4.4 The Muon Detector Electronics

Data recorded with the MD array needs to be synchronised with the data of the SD array. Therefore, the electronics of each AMIGA MD module needs to be able to accept an external trigger signal from the associated SD station. The module create a muon event out of the PMT signals at the time of the trigger. This event is stored sufficiently long until a potential request by the Central Data Acquisition System (CDAS) of the Pierre Auger Observatory is received. The event is then transmitted to the CDAS.

The PMTs generate SPE pulses with an average pulse width of about 3 ns. The signature of a muon is an overlay of several SPE pulses. In order to determine the exact number of muons, their signals need to be distinguished from thermal noise pulses, which result in single SPE pulses. A sampling unit of 320 MHz, and thus a resolution of 3.125 ns, was used to fulfill this requirement.

Like the SD stations, the MD modules are supplied by two batteries each, which are charged by a separate solar panel. It is therefore essential that the total power consumption of the electronics is kept low to allow for the operation of three to four detectors with the batteries. All parts, which form the electronics of the AMIGA MD modules, are described in the following sections.

4.4.1 The Underground Electronics

The electronics readout system was described in detail in [Fro09] and will also be subject of [Fro13]. It will be discussed only very briefly in the following sections.

A power distributor board (PDB), a microcontroller board (MCUB), a digital board

(DB), eight analogue boards (ABs) and one mother board (MB) constitute the underground part of the readout electronics of each AMIGA MD module. The electronics was kept modular to allow for the development of the individual components in different places and for the possibility of reworking one part while the rest of the system remains unchanged.

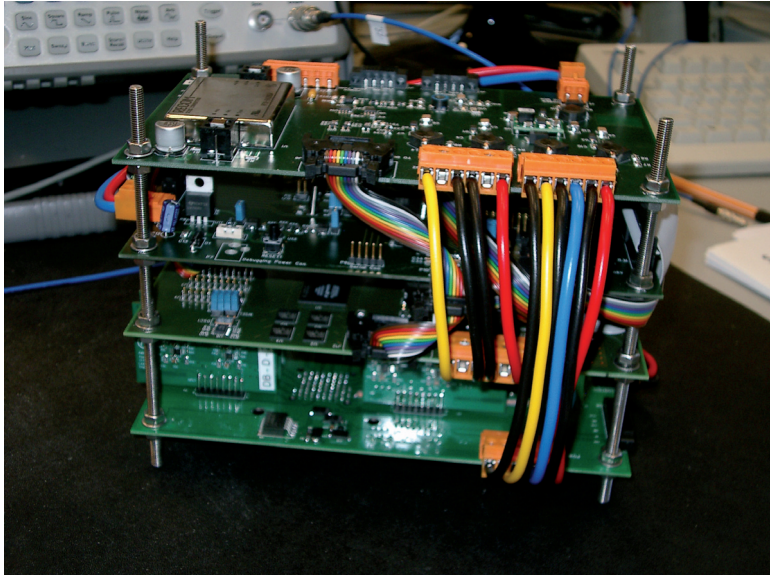


Figure 4.6: A completely assembled setup of the underground readout electronics. From top to bottom: the PDB, the MCUB, the DB, the vertically mounted eight ABs and the MB. Power is distributed through the thick power lines. The communication and trigger line, integrated into one internal flat cable, are distributed to the MCUB and to the DB respectively. Besides providing structural stability and a basis to connect to the PVC casing of the scintillator, the metal threaded rods provide part of the ground connection between the individual boards. The setup shown in the image is meanwhile operating in the MD module of the SD station *Heisenberg*; image: March 2011.

The Power Distributor Board (PDB)

The PDB is the hardware interface between the surface and the underground electronics. Two tasks are performed: the supply of all underground electronics with the required voltages and the galvanic isolation of the ground levels of surface and underground electronics. The latter is required to avoid ground loops and to minimise electronic noise. Voltages of +3.9V are separately generated for the DB, the MB and the MCUB. In addition, the DB is provided with +1.8V and the MB with -3.9V and 12V from the PDB. Low voltage differential signal (LVDS) lines are used for the trigger as well as for the communication link between surface and underground electronics. The

link is realised through a bidirection controller area network (CAN) bus.

The Mother Board (MB)

PMT and readout electronics are connected through the MB. It provides the HV for the PMT and distributes the signals from the 64 directly connected anode pins of the PMT to the eight ABs, which are soldered to the MB in a vertical position. A control circuit limits the maximum HV to -1 kV in order to protect the PMT. A precision HV divider [13] with a division factor of 1000 delivers a HV monitoring signal to the MCUB. From the input voltage of +3.9 V the operating voltages for the ABs of +3.3 V and -3.3 V are generated and provided to each AB.

The Analogue Boards (ABs)

The ABs are the only signal shaping instances of the readout electronics. Eight individual channels are located on each board. Incoming PMT pulses are processed to provide a valid digital input signal, fulfilling the transistor-transistor logic (TTL) standard, to the field-programmable gate array (FPGA) [9] on the DB. PMT pulses are amplified by a nominal factor of $G = 3.1$ [Fro09], inverted and then compared to a threshold voltage by a discriminator. Signal amplitudes above the threshold level result in a discriminator output of 0 V, a logic 1, or 3.3 V, a logic 0, otherwise. A digital-to-analogue converter (DAC) [27] with eight programmable outputs allows the adjustment of individual thresholds for each channel. Thus, variations in the amplifications of the PMT, between PMTs and of the electronic amplifiers can be overcome.

It was shown in [Fro09] that the minimal pulse width, that can be resolved by the electronics, ranges at 2.2 ns. Pulses of 3 ns are prolonged by approximately 25 %, since the amplification circuit operates at its limit. Furthermore, the overall gain decreases slightly below pulse widths of 5 ns. Typical SPE PMT pulses with widths of $t = (3.0 \pm 0.4)$ ns are thus prolonged to pulses with widths of $t' = (3.8 \pm 0.5)$ ns at a gain of $G' = 3.3 \pm 0.1$ [Fro09]. Above 6 ns, pulses remain with the same width at a constant gain. The linearity of the DAC is tested in the threshold scan and channel to channel variations are determined. These tests are described in Chapter 5.

The Digital Board (DB)

The DB is the main piece of the data acquisition (DAQ) system. Digitised PMT signals, as generated on the ABs, are directly fed to input pins of an FPGA [9]. Signal sampling at a frequency of 320 MHz for each of the 64 readout channels, the combination of the single signals to MD module events and the storage of these events are performed using the FPGA and four 2×16 Mbit static memory blocks. The last 2048 MD module events are available for readout and correspond to about 20 s of recording time at a nominal trigger rate of ≈ 100 Hz of the SD T1 trigger. An LVDS receiver provides the T1 trigger information, as distributed by the PDB, to the FPGA.

Upon receiving an SD T3 trigger signal, the FPGA is programmed to search for an associated event inside the memory and to return it for data analysis. A 16-bit wide data bus, an 8-bit wide address bus and additional 3 control lines constitute the interface to the microcontroller on the MCUB. Moreover, the FPGA can be programmed by the microcontroller via five lines applying a passive serial (PS) configuration scheme.

Besides signal sampling and data acquisition, the FPGA controls the threshold voltages of the 64 single input channels. Therefore, four lines for control signals need to be fed to each AB.

The FPGA can operate at frequencies of up to 400 MHz. However, the device is at its specification limit in that case. Thus, the usage of the highest frequencies was reduced to the sampling part of the firmware. Digitised inputs from the ABs are sampled at a rate of 320 MHz in the FPGA. A converter was written, which then prolongs short input pulses to multiples of 12.5 ns and enables a further processing at 80 MHz [s3].

Short SPE pulses are thus detected, but they result in a signal of 12.5 ns length in the data. They cannot be discriminated from longer pulses unless the pulse length exceeds the 12.5 ns. The impact of that situation on the accuracy of the muon number is not yet clarified but is under investigation [Mal12]. However, after an extended period for tests and development of the firmware modules for the peripheric tasks, the FPGA firmware was updated for a full 320 MHz acquisition in August 2012 [s4]. The FPGA firmwares are based on a firmware developed for the Auger SD hardware, which was then adapted to the requirements of the AMIGA MD [Sza09a] and continuously updated throughout the prototype stages. These updates include the addition of features like a trigger prescaler, a trigger rate counter or an internal trigger generator. Functional descriptions of the firmwares are given in [Fro13].

The DB is supplied with two voltages from the PDB. Since the FPGA requires very stable operating voltages of 1.3 V, 2.5 V and 3.3 V, these are generated directly on the DB.

The Microcontroller Board (MCUB)

The MCUB constitutes the programmable interface between the surface and the underground electronics of the MD modules. A CAN connection allows for the communication with a single board computer (SBC) [23] at the surface. Controlling commands to change the output voltages of the DACs on the ABs are sent via CAN bus to the microcontroller [25] on the MCUB, forwarded to the FPGA through the 16-bit data and the 8-bit address bus, and finally executed on the ABs. More commands, which control the operating mode of the FPGA, are transmitted to the FPGA via that bus. At present, the microcontroller is permanently programmed with its firmware [s6], whereas the FPGA on the DB needs to be reprogrammed after each power cut. The microcontroller takes care of that by applying a PS configuration to the FPGA. A 12-bit DAC [11] replaces the former 10-bit DAC [24] and is used to generate the input voltage for the HV power supply [15], which is located on the MB.

The microcontroller includes 12 analogue-to-digital converters (ADCs) [25] with a resolution of ten bits each. These are used to monitor operating voltages of the full system, the output of two temperature sensors, as well as the HV monitoring signal, that is generated on the MB. A humidity sensor could replace one temperature sensor, but it has not yet been applied.

The initial idea to merge the DB and the MCUB was postponed for the benefit of having a fully working detector in 2009. The microcontroller [25] is no more recommended for new designs by the vendor but a full equivalent successor in functionality and parametrics is available meanwhile [26] and could be used instead for future

productions.

4.4.2 The Surface Electronics

The Auxiliary Board LS (AuxLS) and the Auxiliary Board SBC (AuxSBC)

The synchronisation between a AMIGA MD module and the associated SD station requires additional pieces of hardware for the SD electronics. They are referred to as auxiliary board LS (AuxLS) and auxiliary board SBC (AuxSBC) [12], emphasising their placement in the system (Figure 5.9).

The AuxLS receives the modified T1 signal (Section 5.13.2) from the SD front end board (FEB) (e.g. [Sza09b]) as TTL level and converts it to an LVDS signal. Power for the LVDS driver is drawn from the SD FEB. The modified T1 trigger signal is sent to the AuxSBC, which distributes it to a maximum number of two underground MD readout electronics while isolating the ground levels. In order to supply up to four underground readout electronics, extensions to the auxiliary boards are necessary.

The AuxLS furthermore submits pairs of local and global timestamps, LTS and GTS, on a serial peripheral interface (SPI) bus as LVDS signals to the AuxSBC. Using a complex programmable logic device (CPLD) [8], configured with the AMIGA CPLD firmware for trigger synchronisation [s1], the AuxSBC retrieves the SPI signal and stores the timestamp pair in a 48-bit wide shift register. Then, it launches an interrupt to the SBC [23] to which it is connected on a socket for the PC/104 bus [Con12a].

The SBC will then read the timestamp pair bitwise from the CPLD, applying an 8-bit industry standard architecture (ISA) protocol. The interrupt signal is resetted by the CPLD as soon as the first byte of the timestamp pair was requested. The SBC stores the last 2048 pairs of timestamps in a ring buffer.

The AuxSBC also houses the voltage converter, which lowers the battery voltage of 24 V to 5 V to supply the SBC. Furthermore, it serves as the distributor of the CAN signals, coming from the SBC, to up to two underground readout electronics systems.

To simplify the installation, Ethernet cables with RJ45 connectors were used for the interconnection cables between the two auxiliary boards.

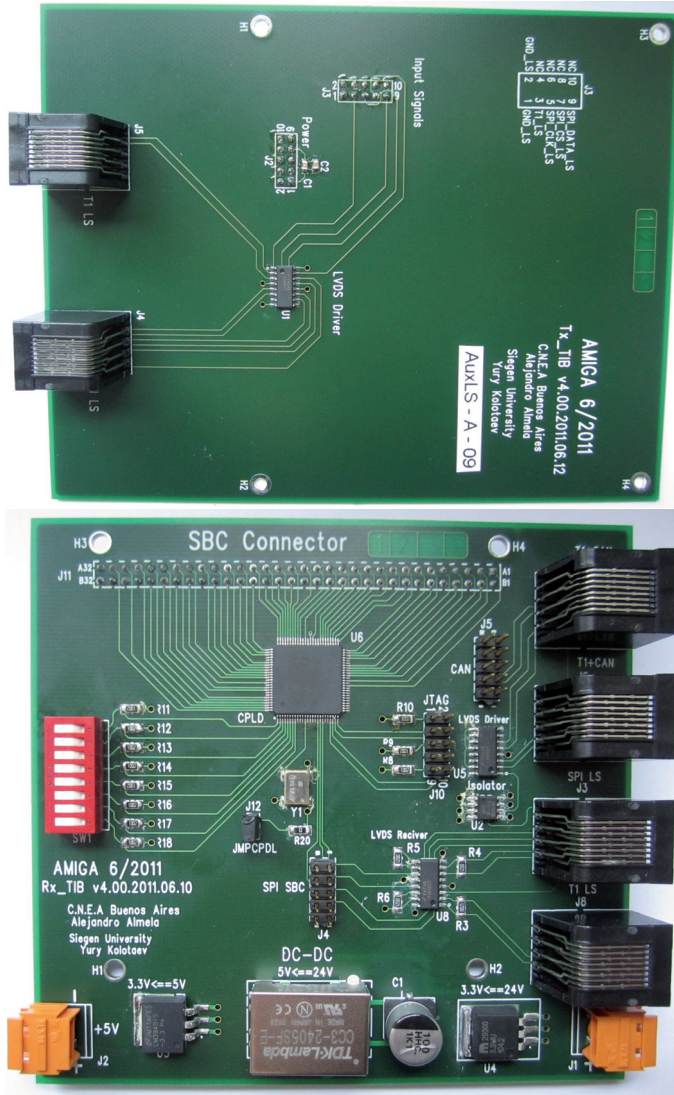


Figure 4.7: The two auxiliary boards AuxLS (top) and AuxSBC (bottom).

Chapter 5

System Tests

The analysis of detector data with the aim of revealing the physics behind it is only worth the effort if the detector itself is well understood. Precise investigations of the detector response to given signals have to be performed before deployment and data taking. In case of the AMIGA MD modules, the information, which a detector-traversing particle leaves, is modulated manifold. The response function is determined by the scintillator and the fibres, by the PMT and finally by the signal processing electronics.

Geometric reasons, like the distance of the hit position to the PMT or the inclination angle of the incoming particle, as well as material related reasons, like fluctuations in the local density of the scintillating and WLS materials, lead to non-constant attenuations of the light intensity for different strips under the same hit conditions. To accomplish and to characterise this scintillator related part of the response function, a module scanner was developed [Pla11].

Light, that is guided through the WLS fibres, enters the PMT. Apart from the positioning of the single fibres on the associated PMT pixel, the intrinsic properties (Section 4.3.2) of the PMT and the individual channels play a major role in the shaping of the electrical signal. Each PMT channel is characterised individually [Sua09] and its properties are documented.

The last piece of the response function is formed by the readout electronics and, more precisely, by the analogue part of it. The following sections of this thesis are dedicated to the description of the full system tests of the underground electronics of the MD modules. The tests characterise each single setup and guarantee full functionality. The systems are tested in an environment that is close to the later conditions, e.g. using the SBC already in the tests instead of developing purely stand-alone solutions. The procedures to perform the full system tests are documented in detail in a manual [Pon11].

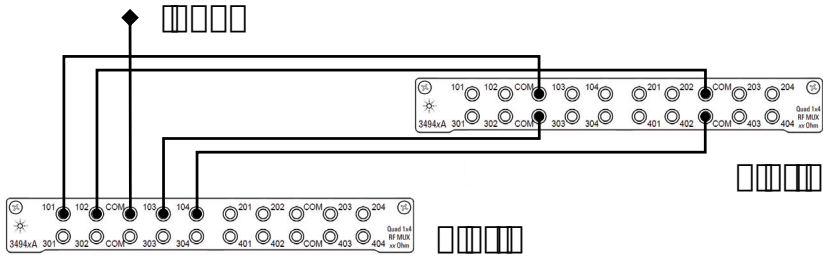
In the following, a short explanation of the test is given at each section beginning. Then, a code listing is given for the experts for completion.

5.1 Test Stand Setup

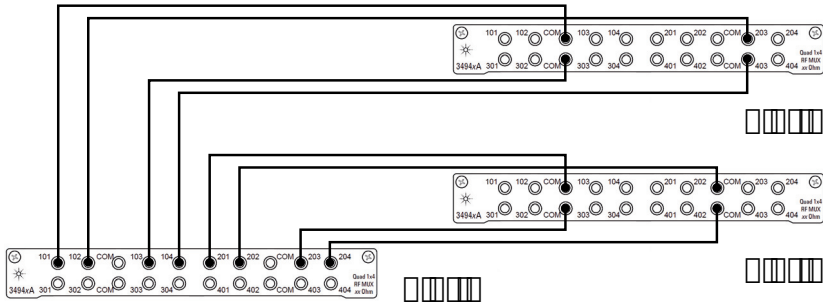
The test stand was kept identical for all electronics setups to obtain comparable results. In those tests, in which signals were sent to individual channels, namely the channeltest, the crosstalk test and the threshold scan, a multiplexing analogue switching unit [5, 6] was used to distribute the signals coming from a single arbitrary waveform generator [4] to the channel of choice. A quad module [5] multiplexes four independent input channels to four output channels each. Six such modules were used in the mainframe [6]. Multiplexing one input channel to 64 equivalent output channels was achieved by cascading modules. A signal, which is multiplexed to any of the output channels, passes three electromechanical switches. The cascading scheme and the location of the quad modules in the slots of the mainframe are given in Figures 5.1(a), 5.1(b) and 5.1(c).

The final interface to the AMIGA readout electronics system is the test stand interface board (TIB). Coaxial cables with gold-plated SubMiniature version A (SMA) connectors were used for the cascades and the connection of the multiplexer outputs to the TIB inputs. A coaxial cable, one-side ended with a mini push-pull-connector [LEM12] and the other side ended with an gold-plated SMA connector, was used to connect waveform generator and multiplexer.

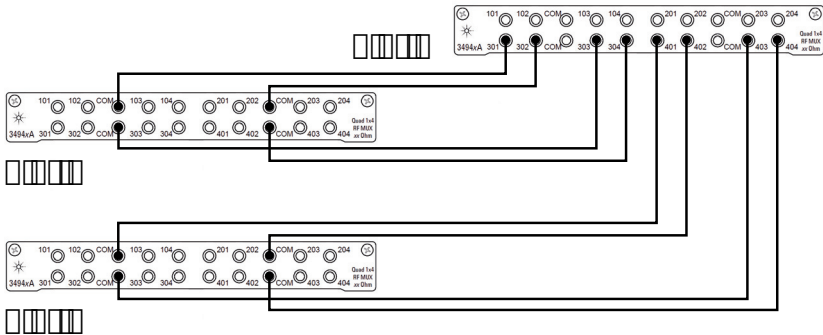
The multiplexer mainframe as well as the waveform generator allow control via GPIB (general purpose interface bus) applying SCPI commands (standard commands for programmable instruments) [IVI12]. A computer was connected via an USB-to-GPIB converter [3]. The devices were addressed using libraries [Bro12] for the Python programming language [Pyt12]. Access to the command prompt of the SBC was realised using a telnet/ssh client [Tat12]. An automation and scripting language [Aut12] was applied to control and interface the different applications running on the computer. Several applications, scripts and libraries were written to perform the system tests. An overview on the test stand and the interconnection of the devices in use is given in Figure 5.2.



(a) First step of multiplexing.



(b) Second step of multiplexing for the channels 0 to 31.



(c) Second step of multiplexing for the channels 32 to 63.

Figure 5.1: Multiplexing scheme: (a) The two distributor modules, (b) distribution of the signals from the distributor module in slot 2 to serve channels 0 to 31, and (c) distribution of the signals from the distributor module in slot 2 to serve channels 32 to 63.

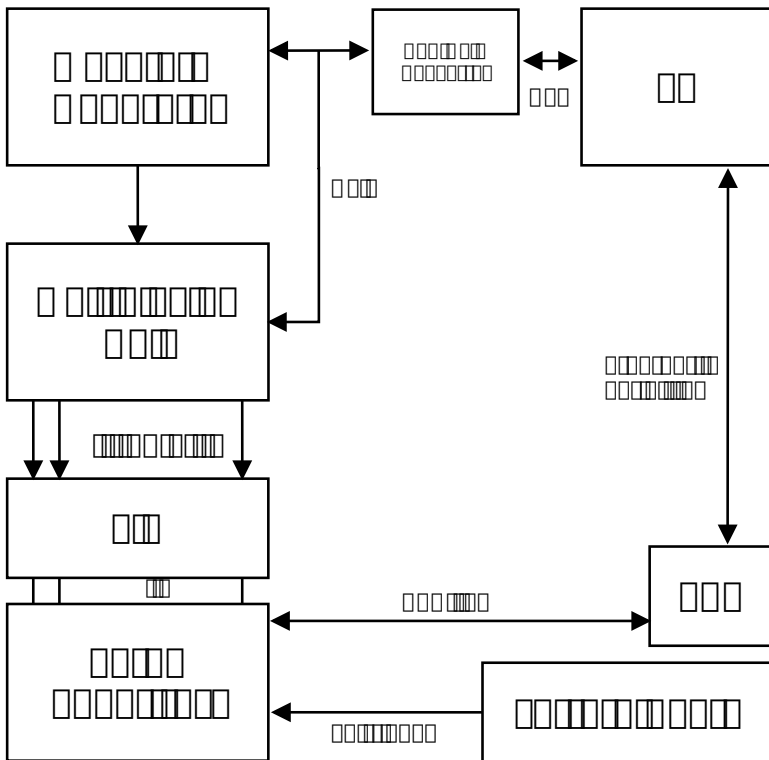


Figure 5.2: Interconnection of the devices used in the test stand.

5.2 Configuration of the Microcontroller

This test is a single board test rather than a test of the full system. It is performed before the assembly of the full setup. Since it was developed following the need to have a test of the MCUB before the integration into the full system, it is the subject of this section.

A good electrical connectivity between the pins of the microcontroller and all connected output pin rows needs to be assured. A dedicated test firmware was written [s2]. When configured with this firmware, the microcontroller generates rectangular waveform pulses on all output pins, that have connections to peripheric pin rows. Adjacent pins are fed with signals of different frequencies, so that electrical shorts can easily be detected. By connecting LEDs (light emitting diodes) or an oscilloscope to the peripheric pin rows, the correct connectivity is verified. After that, the microcontroller is configured with the AMIGA data acquisition firmware [s6]. The board is repowered to make sure that the configuration was performed permanently and will not be erased by a power cut. The built-in LEDs of the MCUB are programmed to flash in the dedicated testing code, so that it can be clearly distinguished from the data acquisition firmware for which flashing should no more appear. Since the MCUB serves as an interface board, no more single board tests are performed for this board, but the functionality e.g. of all monitoring circuits or the HV controlling is checked in full system tests using the AMIGA data acquisition firmware.

Up to now, the microcontroller can only be configured using the JTAG protocol (joint test action group). A remote configuration via the communication CAN bus line was not yet developed but is under investigation.

5.3 Communication via CAN

The basic communication between SBC and MCUB is checked in both directions through a simple test. A successful readout of the microcontroller firmware version ensures that commands can be sent to, and data can be received from the MCUB. It is also ensured, that the correct firmware is permanently programmed into the flash memory of the microcontroller.

```

1 # export MCU_ADDR=300
2 # sh read_mcu_ver.sh
3 Opening /dev/can0
4 Sending message 300 [f4 00]
5 Received message #1: id:300 data:[00 06 00 10 00 00 00 00]
```

Listing 5.1: Readout of the MCU firmware version. The address of the microcontroller in the CAN network needs to be set (l. 1) and a script needs to be executed (l. 2). The firmware version can be derived as 6.16 from line 5.

In Listing 5.1, firmware version 6.16 was programmed, which can be concluded from the bytes six 0x06 and four 0x10 in the output line, printed as hexadecimal numbers. Except for one setup, all readout setups were configured with this version before the delivery. This one setup was installed in a three-node network with another setup and an SBC at *Corrientes* and therefore needed another address.

5.4 Configuration of the FPGA

This test ensures, that the FPGA on the DB can be configured with any firmware. For the tests and for data taking, the DAQ firmware [s3] needs to be present.

The configuration process is invoked by an application which was developed for the SBC [23]. FPGA firmware needs to be present in raw binary format (rbf).

First, the configuration mode is set inside the microcontroller on the MCUB and second, the FPGA firmware is sent to the microcontroller in blocks of eight bytes. After one block was received, the microcontroller directly transfers this data to the FPGA following the PS configuration scheme as described in [9].

In order to speed up the process, it is recommended to change the firmware of the microcontroller such that first the full firmware data is present inside the buffers of the microcontroller and only then the configuration of the FPGA starts. Typical file sizes of the firmware files of less than 300 kB do not exceed the internal storage capabilities of 1 MB inside the microcontroller.

Since the method applied abstains from a feedback from the microcontroller to the SBC, that the write process of the last data block was completed, delays between the sending of the blocks need to be sufficiently long. A delay of 80,000 empty loop cycles between two blocks was found to be sufficient. The delay value is parsed as parameter to the configuring application besides the start position and the filesize (compare Listing 5.2, l. 12). The FPGA is configured with the DAQ firmware [s3] for all system tests in which the FPGA is involved. The sequence of commands and the corresponding output of the SBC is shown in Listing 5.2.

```

1 # sh read_version.sh
2 Open CAN interface /dev/can0 ...
3 Inside t3daq mode          r
4 Inside t3daq reg           0x40
5 Inside t3daq filebase     /dev/tty
6 Message sent now waiting for CAN /dev/can0 :
7 1 00 00 FF FF 00 00 00 00
8 #
9 # stat -c %s \ac{AMIGA}.v0.1a_bc_2048.rbf
10 279790
11 #
12 # program_fpga \ac{AMIGA}.v0.1a_bc_2048.rbf x 0 279790 80000
13 Arguments passed to the program:
14 binfile : \ac{AMIGA}.v0.1a_bc_2048.rbf
15 mode    : x
16 filesize : 279790 bytes (0444ee bytes)
17 start   : 0
18 end     : 279790
19 delay   : 80000
20 nbytes  : 279790 = 0444ee (hex) bytes to be sent.
21 MCU_ADDR : 0x300
22 The complete file content is now in memory.
23 Start of programming.
24
25 End of programming.
26 #
27 # sh read_version.sh
28 Open CAN interface /dev/can0 ...

```



```

29 Inside t3daq mode           r
30 Inside t3daq reg           0x40
31 Inside t3daq filebase      /dev/tty
32 Message sent now waiting for CAN /dev/can0 :
33 1 00 00 00 1A 00 00 00 00

```

Listing 5.2: Configuration of the FPGA with the DAQ firmware [s3] via the microcontroller. Response for an incorrectly configured FPGA (ll. 1-7), determination of the filesize of the firmware file (ll. 9/10), configuration of the FPGA (ll. 12-25) and response for a correctly configured FPGA (ll. 27-33).

5.5 Read and Write Access to Registers of the FPGA

The communication between FPGA and SBC uses the registers inside the FPGA. This ensure, that the parallel data and address buses are operational on every line.

Therefore, bit patterns `0xAAAA` and `0x5555` are written to different registers inside the FPGA and then read out again. Thus, it is tested, whether all lines of the 16-bit data bus between microcontroller and FPGA are correctly connected. An example of the output of a successful test is given in Listing 5.3.

```

1 # sh write_reg.sh 4A 55 55
2 Sending message 300 [fc 4a 55 55]
3 # sh read_reg_fast.sh 4A
4 1 00 00 55 55 00 00 00 00
5 # sh write_reg.sh 4A AA AA
6 Sending message 300 [fc 4a aa aa]
7 # sh read_reg_fast.sh 4A
8 1 00 00 AA AA 00 00 00 00

```

Listing 5.3: Writing of 16-bit patterns to the register with the address `0x4A` inside the FPGA and readout of the stored values.

5.6 Channeltest

For every assembled setup, first of all, the basic functionality of the 64 channels is checked in the channeltest. That means, that the channels show a reaction if there are signals fed to their inputs.

Although all boards, that are assembled to a full system, were checked in single board tests (see [Fro09, Fro13]), it may happen that during the soldering and assembling process some electrical circuits are damaged. Severe malfunctions caused by such damages are already detected at that early stage. In that case, further testing is postponed until the electronics was repaired.

```

1 ;Variables for the scan
2
3 $initial_high_code = 100 # corresponding to approx. -50 mV
4 $hvoltage = 0 ; in V
5 $lvoltage = -.210 ; in V
6 $pwidth = 1e-6 ; in s

```

```

7
8 $occ = 1
9 $mask = "ff ff ff ff ff ff ff ff"
10
11 $ncycles = 1

```

Listing 5.4: Typical settings for the channeltest.

For this test, variables need to be set in the settings file according to Listing 5.4. To make sure that incoming pulses will definitely be seen by a well operating channel, the thresholds are set to a corresponding level of ≈ -50 mV (`$initial_high_code`), which is much lower than the pulse amplitude of -210 mV (`$lvoltage` w.r.t. `$hvoltage`). Thus, after amplification on the AB, the comparator has to evaluate a ≈ 630 mV signal against a 50 mV threshold. With a width of 10^{-6} s (`$pwidth`) the rectangular input pulses are chosen to be well within the technical specifications of the analogue devices and can safely be detected at a sampling rate of 320 MHz. The FPGA is configured to trigger on an incoming analogue pulse on any of the 64 channels (occupancy trigger on `$occ` channels). The `$mask` variable can be used to deactivate channels which are noisy or otherwise known to be malfunctioning.

One pulse (`$ncycles`) is now sent to the first channel. Then, the multiplexer unit is requested to switch to the next channel until all 64 channels were covered. After that, the first 64 recorded events are read out and stored.

If all channels are operate as expected, event N will show a signal only for channel N . Plotting the active channel number against the event number reveals errors or shows full functionality. In Figure 5.3, the resulting plot for a well operating system, is shown. Figure 5.4 instead represents the resulting plots for a failed channeltest. Here, the test revealed noisy channels on AB 1, which is represented by the channels 0 to 7 . Throughout all events, channel 6 is active. Disabling that particular AB leads to the correlation shown in Figure 5.4(b). Another error becomes visible: channel 53 did not show any response. The channel could not be recovered and further tests were performed while disabling this channel. The setup was held back for laboratory tests.

Driven by the need for a quick check of the channeltest data, an SBC based script was written. In contrast to the offline analysis program, this script accesses very few data per event and displays them in text mode. An example of the output is given in Listing 5.5. Thus, it can directly be evaluated whether a continuation with the next time-consuming test is appropriate or whether the setup needs repair work.

```

1 # sh channeltest_binz.sh /external/11-06-08_channeltest_SETUP11/
   channeltest_evt /external/11-06-08_channeltest_SETUP11.log
2
3 Channeltest quickscan on
4 /external/11-06-08_channeltest_SETUP11/channeltest_evt
5
6 00: pos. 03fb sig. ...1 subpos. 3: ch. .... .1
7 01: pos. 03fb sig. ...2 subpos. 3: ch. .... .2
8 02: pos. 03fb sig. ...4 subpos. 3: ch. .... .4
9 03: pos. 03fb sig. ...8 subpos. 3: ch. .... .8
10 04: pos. 03fb sig. ..1. subpos. 3: ch. .... .1.
11 05: pos. 03fb sig. ..2. subpos. 3: ch. .... .2.
12 06: pos. 03fb sig. ..4. subpos. 3: ch. .... .4.
13 07: pos. 03fb sig. ..8. subpos. 3: ch. .... .8.

```

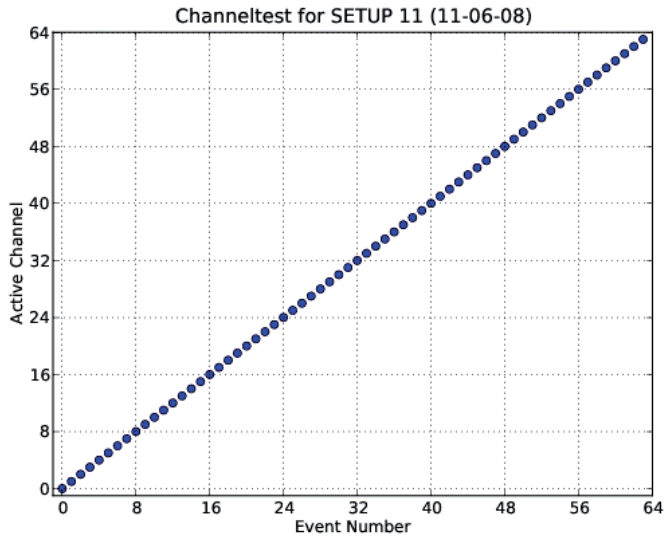


Figure 5.3: Channeltest evaluation for a fully operational setup. All channels behave as expected.

```

14 ...
15 60: pos. 03f8 sig. 1... subpos. 0: ch. 1... ..
16 61: pos. 03f8 sig. 2... subpos. 0: ch. 2... ..
17 62: pos. 03f8 sig. 4... subpos. 0: ch. 4... ..
18 63: pos. 03f8 sig. 8... subpos. 0: ch. 8... ..

```

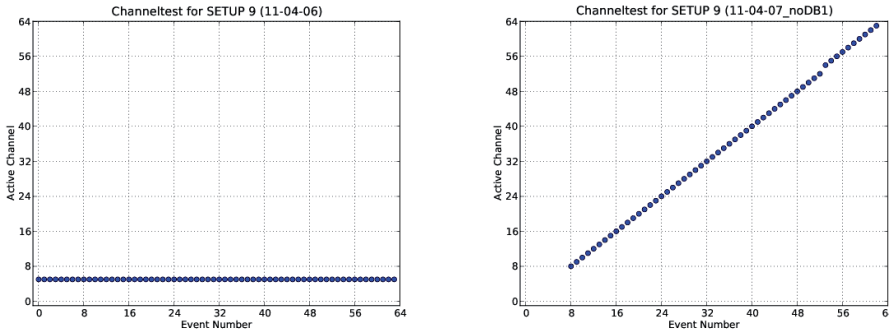
Listing 5.5: Output of the channeltest quick check. The first entry in each row shows the channel, which should respond. The last entry shows the position of the measured response in hexadecimal encoding.

5.7 Crosstalk Test

After the basic functionality was tested, a scan of electrical crosstalk between channels is performed. Electrical crosstalk may occur if one channel is coupled, capacitively, inductively or conductively, to another one and thus reacts without incoming signals. The crosstalk test makes sure that a channel reacts only if it had a signal on its input.

It is more likely that this error is seen on high input currents rather than on low ones. In order to find crosstalk, a pulse with high amplitude is sent into one channel and the response of all channels is recorded. The same test routine as for the channeltest is applied, albeit with modified settings (Listing 5.7).

Comparable to the channeltest, a negative rectangular pulse with an amplitude of -800 mV (`$lvoltage`), a pulse width of 28 ns (`$pwidth`) and a period of 1 μ s (`$period`) is chosen. The pulses are repeated five times (`$ncycles`) per channel. Such signals



- (a) Channel 6 of the system under test permanently triggers the system. (b) Repetition of the channeltest excluding AB 1. Another error is seen on channel 53, this channel could not be recovered.

Figure 5.4: Channeltest evaluation for a failing setup, with and without analogue board (AB) 1 enabled. Typical results for a noisy (a) and a dead channel (b).

are significantly larger in amplitude and width than any pulse which the PMT can generate from the light of a muon when passing the scintillator. The test is repeated until a minimum threshold (variated through `$initial_high_code`) is found at which crosstalk appears. If no electrical crosstalk is seen in this test, it can be concluded, that there won't be any using the PMT as input device above the minimum threshold.

```

1 $initial_high_code = 15
2
3 $hvoltage = 0 ; in V
4 $lvoltage = -.800 ; in V
5 $pwidth = 28e-9 ; in s
6 $period = 1e-6 ; in s
7
8 $occ = 1
9 $mask = "ff ff ff ff ff ff ff ff"
10
11 $ncycles = 5

```

Listing 5.6: Typical settings for the crosstalk test. The channeltest test routine is executed. The settings are modified.

5.8 External Trigger Acceptance

One of the most important function of the AMIGA MD module is the synchronisation with the assigned SD station as it is described in detail in Section 5.13. For each underground electronics it needs to be tested that T1 trigger signals sent by the station are decoded correctly in the underground FPGA.

The MD readout electronics is set into the mode for external trigger acceptance. The pattern board needs to be configured with a dedicated firmware. A sequence of T1 trigger signals, each followed by a well-known 24-bit timestamp, is then sent to the readout electronics. After each sending procedure, the last timestamp, that was received, is requested from the FPGA by the SBC (Listing 5.7) and compared with the pattern sent.

Trigger signals are sent, until it is clear, that all 24 bits are transferred correctly. It can be concluded that the decoding algorithm samples all bits at the correct position and the lines carry no noise.

Advanced tests of the external trigger decoding part of the FPGA firmware were performed representatively for one setup. They are described in Section 6.3.2.

```
1 # export MCU_ADDR=300
2 # sh activate_t1.sh
3 Sending message 300 [fc 48 00 02]
4 # read_last_ts
5 2736e7
6 # read_last_ts
7 c5d655
8 # read_last_ts
9 b29ec3
10 # read_last_ts
11 e51c14
12 # read_last_ts
13 61604e
14 # read_last_ts
15 0effe1
16 # read_last_ts
17 8ebe40
18 # read_last_ts
19 a9466b
20 # read_last_ts
21 1e6141
22 ...
```

Listing 5.7: Output of the T1 trigger test for Setup 9. Activation of the external trigger acceptance mode (ll. 2/3), manual trigger to the electronics (not shown), readout of the last timestamp received by the FPGA (l. 4) and repetition of the procedure.

5.9 Threshold Scan

Of all full system tests, the threshold scan characterises an electronic setup most, but it is at the same time the most time consuming one. The gain of a PMT pixel, the attenuation of a WLS fibre, the coupling of the fibre to the pixel, the amplification circuits of the ABs and the integrated circuits themselves are subject to fluctuations due to production tolerances. In order to provide the same sensitivity to all 64 channels, it is necessary to be able to adjust each discriminator threshold for each single channel individually. The response of the electronics to a well known input signal can be determined in the threshold scan and therefore, fluctuations can be overcome.

As all other tests, the threshold scan is fully automated. A settings file allows for modifications of parameters without running the danger of changing the structure of the test routine. A typical initial setting for a threshold scan of a full system is given in Listing 5.9.

A list of programming codes for the DACs (`$codes_measure`) on the ABs as well as a list of channels that will be scanned (`$channels_measure`) have to be defined in the settings file. Following the entries in the list of codes, the output voltages of the DACs on the ABs are programmed for all channels. The threshold voltages are thus set to a level that is calculated from Equation 5.1 [27]:

$$V_{OUT} = \frac{2 \times V_{REF} \times \text{code}}{4096} = \frac{\text{code}}{2} \text{ mV with } V_{REF} = 1.024 \text{ mV.} \quad (5.1)$$

Given the theoretical value of the AB amplification $A_{AB}^{theo} \approx 3.1$ [Fro09], an estimate for the negative amplitude of the input pulse is determined as $v_{code} = \frac{-\text{code}}{2 \times 3.1} \text{ mV}$, which corresponds to the theoretical 50 % value for the detection efficiency.

Now, the efficiency curves of all channels for the current threshold are measured consecutively. Therefore, pulses from the waveform generator are distributed via the multiplexing unit to the first channel given in the list of channels. 1000 pulses (`$ncycles`), with a pulse width of $1 \mu\text{s}$ (`$pwidth`) and a period of $500 \mu\text{s}$ (`$period`), are sent from the waveform generator to the channel currently under test. Around the estimate v_{code} , a scan region, ranging from $v_{code} + v_{range+}$ to $v_{code} - v_{range-}$, is calculated. The pulse amplitude is then varied in that region by increments of 0.6 mV (`$stepsize`) each.

The firmware of the FPGA is configured such, that it is sensitive only to that single channel by disabling all others for the trigger generation. Every pulse above the current threshold should result in a recorded event. The amount of all events is recorded for each increment. The detection efficiency η at the current threshold can thus be determined, since it is known how many pulses constitute the input sequence. The data pair of the pulse amplitude from the waveform generator and the number of pulses seen by the AMIGA electronics is written into a logfile on the SBC. Results from an example measurement are shown in Figure 5.5. The actual values for the gain of a single channel A_{AB}^i , as determined in the single board tests of the ABs, are taken into account to compare the pulses sent by the waveform generator with the theoretical expectation.

An s-curve following Equation 5.2 was fitted to the data:

$$y = 50 + 50 \cdot \operatorname{erf}\left(\frac{x - p_0}{p_1}\right), \quad \text{with} \quad \operatorname{erf}(u) = \frac{2}{\sqrt{\pi}} \int_0^u e^{-t^2} dt. \quad (5.2)$$

From this, the 50 % efficiency value can be deduced. The asymmetric uncertainties of a single efficiency measurement were determined following [UII07]. The difference between the theoretical threshold voltage, v_{code} , and the 50 % efficiency is visible in Figure 5.5 and originates from the fluctuations mentioned above.

```

1 $hvoltage = 0.0 ; in V
2 $stepsize = 0.6e-3 ; in V
3 $ncycles = 1000
4 $pwidth = 1000e-9 ; in s
5 $period = 500e-6 ; in s
6 $occ = 1
7 $vrang_pos = 0.010 ; in V
8 $vrang_neg = 0.015 ; in V
9
10 ; list of programming codes
11 Dim $codes_measure[21] = [110,210,310,410,510,610,
12                          710,810,910,1010,60,160,
13                          260,360,460,560,660,760,
14                          860,960,10]
15
16 ; list of channels
17 Dim $channels_measure[64] = [ 0, 1, 2, 3, 4, 5, 6, 7,
18                              8, 9,10,11,12,13,14,15,
19                              16,17,18,19,20,21,22,23,
20                              24,25,26,27,28,29,30,31,
21                              32,33,34,35,36,37,38,39,
22                              40,41,42,43,44,45,46,47,
23                              48,49,50,51,52,53,54,55,
24                              56,57,58,59,60,61,62,63]

```

Listing 5.8: Typical settings to configure the test stand for a threshold scan.

Through the determination of the 50 % efficiency values for all programming codes given in the list of codes in Listing 5.9, the functional dependence between programming code and measured output voltage of the DAC on the AB is calculated for each channel. A line, following Equation 5.3, is fitted to the recorded data pairs:

$$\text{code} = \frac{\text{slope}}{100 \text{ mV}} \cdot U_{thr} + \text{offset}. \quad (5.3)$$

The fit parameters, which are the slope and the offset value, as well as their uncertainties are saved in a configuration file for the electronics setup under test. With this configuration file, the precise adjustment of a threshold voltage U_{thr} is achieved by recalculating the required programming code from the line parameterisation in an SBC script using Equation 5.3.

Part of the production roadmap was the evaluation of the results determined in the tests of a first series of electronics setups, which include those dedicated to the pre-unitary cell (PUC), to detect irregularities. It was thus found, that repeated measurements on some channels each did show a linear dependence between threshold

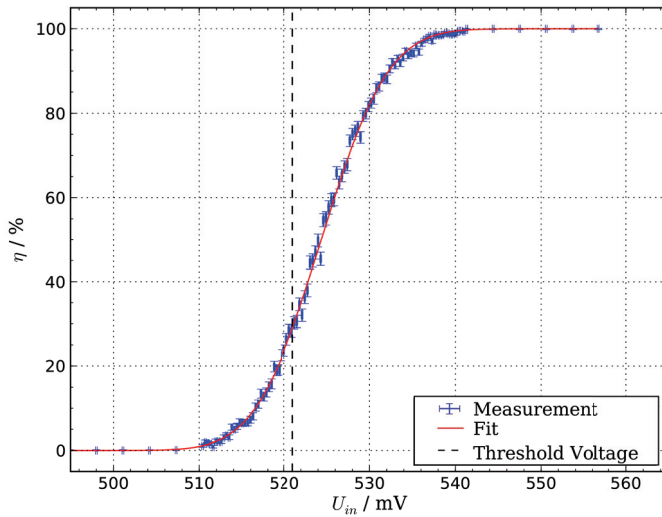


Figure 5.5: Threshold scan for a single channel and one threshold voltage. The dashed vertical line represents the theoretical value v_{code} of the threshold as calculated via the datasheet formulae. Each blue cross represents a single measurement of the detection efficiency η for input pulses with amplitude U_{in} multiplied by the amplification A_{AB}^i of that channel as determined in single board tests. An s-curve was fitted to the data (compare also [Fro09]).

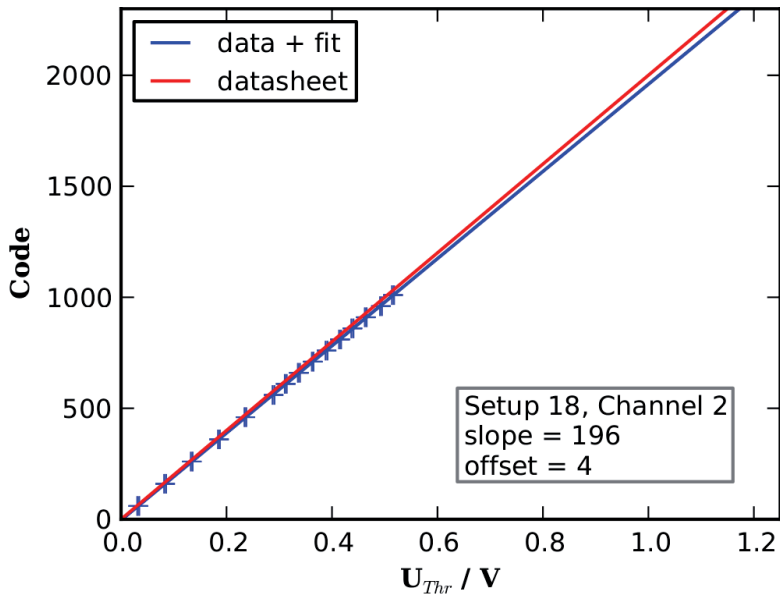


Figure 5.6: Linearity measurement for channel 2 of Setup 18. A linear fit was applied to the 50 % efficiency values, that were measured for different thresholds, which were programmed with a given code value to the DAC. The theoretical values should be 200 and 0 for slope and offset respectively, corresponding to a relation of 2:1 between code and U_{thr} (compare [27]).

code and determined 50 % efficiency values but the different line fits had incompatible slopes and offsets. The origin of this behaviour was found in the test stand itself. It is described in more detail in Section 5.1. A modification of the test setup, e.g. by replacing the analogue multiplexer unit by a digital one or a regular monitoring of the performance of the multiplexer unit and an improved contact between TIB and the setup under test is recommended for future measurements of this kind. However, the threshold scan can still be used to discriminate between operating and non-operating channels. Every measurement was found to result in a linear dependence between programming code and determined threshold voltage as expected from the datasheets of the analogue components in use. If a channel was found to be non-linear or non-operating at all, a repair attempt was started.

5.10 High Voltage Characterisation

The level of the HV for the PMT is programmable using a 12-bit DAC [11] on the MCUB. The results of this test are used to find the programming value to precisely adjust the HV taking into account the characteristics of individual setups.

The DAC feeds its output voltage $U_{control}$ to a compact HV power supply [15] on the MB. The HV power supply can generate output levels of up to $U_{HV} = -1.25$ kV. A protection circuit limits $U_{control}$ to 4.0 V which corresponds to a HV output of $U_{HV} = -1$ kV. Executing an SBC script invokes a process in the microcontroller, which reconfigures the DAC over an SPI protocol. The programming value $code_{HV} = 0 \dots 4095$ is converted to

$$U_{control} = \frac{2 \cdot U_{REF}}{4096} \cdot code_{HV} = \frac{5V}{4096} \cdot code_{HV}, \quad (5.4)$$

with the reference voltages $U_{REF} = 2.5V$ generated directly on the MCUB. For the characterisation of the HV, several levels are programmed and the sets of programming values $code_{HV}$, HV values U_{HV} and monitored HV $U_{HV,mon}$, as measured with a digital multimeter [28], are recorded. The functional dependence between $code_{HV}$ and U_{HV} can be determined by applying a linear regression fit, following Equation 5.5, to the data:

$$code_{HV} = U_{HV} \cdot Slope_{HV} - Offset_{HV}. \quad (5.5)$$

Exemplarily, one fit is shown in Figure 5.7.

The resulting parameters $Slope_{HV}$ and $Offset_{HV}$ of the fit can now be used to adjust the HV precisely to the required value U_{HV} . They are added to a configuration file. In the test, it is then checked, that the protection circuit prevents the adjustment of HVs larger than $U_{HV} = -1$ kV. For this purpose, higher values are programmed and it is checked whether the HV runs into the limit.

To set the HV U_{HV} to the desired voltage, the programming value $code_{HV}$ is calculated in an SBC script following Equation 5.5. The programming value is then written into the DAC by invoking a routine inside the microcontroller and thus, the HV is adjusted. By measuring the HV monitoring voltage $U_{HV,mon}$ with a digital multimeter [28] for different HVs, it is made sure that the HV divider [13] is operating and provides $U_{HV,mon} = U_{HV}/1000$.

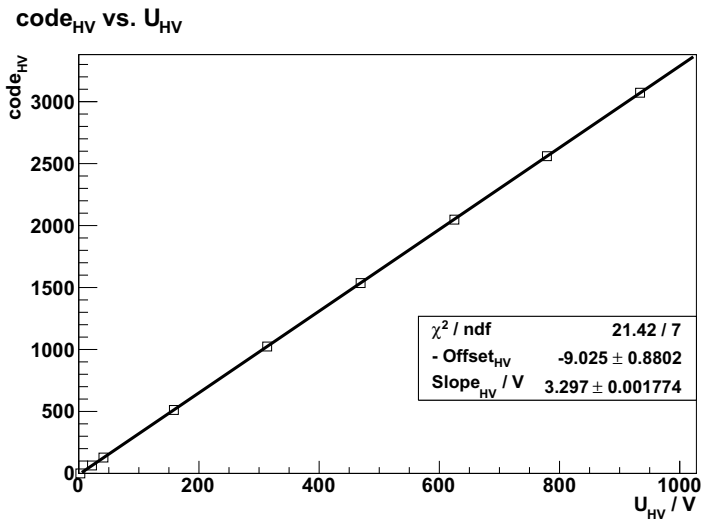


Figure 5.7: Functional dependence between the programming value $code_{HV}$ for the DAC and the HV U_{HV} as directly measured. Exemplarily shown for one setup. The programming value is assumed to be exact and an uncertainty of 0.5 V is assumed for the HV measurement. A linear fit was applied. The fit parameters deliver the characteristic values for the HV circuits $Slope_{HV}$ and $Offset_{HV}$.

5.11 Monitoring Voltages and Temperatures

The microcontroller on the MCUB holds a 12-channel multi buffered analogue-to-digital converter (MibADC) with a resolution of ten bits per channel [25, Tex05]. This test, ensures that all monitoring channels work and values are recorded and cross checked with multimeter measurements.

Inside the MibADC, the twelve input channels are multiplexed to one ADC. Seven monitoring signals for supply voltages, the HV monitoring signal on the MB and the output of the two temperature sensors on the MCUB are fed to the input channels of this MibADC.

As voltages from different parts of the system are measured with the MCUB, the connectivity and functionality of the monitoring circuits are ensured in a full system test and not in a single board test. The test provides values that can later be compared with those values that will be measured with the MibADC once the system is deployed at the experimental site.

Those voltages, which need to provide constant levels, are measured with a digital multimeter [28] first. This applies for the first seven entries in Table 5.1.

Before entering the monitoring circuit, the HV is divided to $U_{HV,mon} = U_{HV}/1000$ using a high precision resistor chain [13]. This reduced voltage $U_{HV,mon}$, is then fed into the monitoring circuit (compare also the previous section).

There are two identical temperature sensors [10] connected to the MCUB. One is mounted directly on the board, the other one can operate as external temperature sensor. The sensors produce an output voltage ranging from $U_{Tmon}(0^\circ\text{C}) = +0.25\text{ V}$ to $U_{Tmon}(100^\circ\text{C}) = +3.05\text{ V}$ using a supply voltage of $V_s = 3.3\text{ V}$ [10]. The output voltage U_{Tmon} of the sensor as a function of the surrounding temperature T is given by Equation 5.6 [10]:

$$U_{Tmon}(T) = \frac{V_s}{3.3\text{V}} \cdot (0.25\text{ V} + T \cdot 0.028\text{ V}/^\circ\text{C}) = 0.25\text{ V} + T \cdot 0.028\text{ V}/^\circ\text{C}. \quad (5.6)$$

Thus, at the constant laboratory temperature $T_{Lab} = 21^\circ\text{C}$, the sensors theoretically provide $U_{Tmon}(T_{Lab}) = 0.838\text{ V}$.

The MibADC provides digitised values A_{DIG} to the input voltages U_{IN} following Equation 5.7 [Tex05]:

$$A_{DIG} = \frac{1024 \cdot (U_{IN} - U_{REFLO})}{U_{REFHI} - U_{REFLO}} = \frac{1024}{2.5\text{ V}} \cdot U_{IN}, \quad (5.7)$$

where the reference voltages are $U_{REFLO} = 0\text{ V}$ and $U_{REFHI} = 2.5\text{ V}$. The MibADC can thus digitise amplitudes between 0 and 2.5 V in 1024 steps. A resistor chain, working as a voltage divider, and an operational amplifier, working as an impedance converter, are connected to each of the monitored voltages. They convert the monitored voltages U_{mon} to levels below $U_{REFHI} = 2.5\text{ V}$. Fluctuations in positive and negative directions can be covered best over comparable ranges if the voltage is converted to about 50 % of U_{REFHI} . Exemplarily, such a circuit is shown in Figure 5.8 with the monitoring scheme for $U_{mon} = 2.5\text{ V}$ from the DB.

The formulae, that explain how to reconvert the obtained digital values A_{DIG} to the monitored voltages U_{mon} , are provided in Table 5.1. The nominal values for the digital values are given based on the nominal values of the resistors that are installed in the

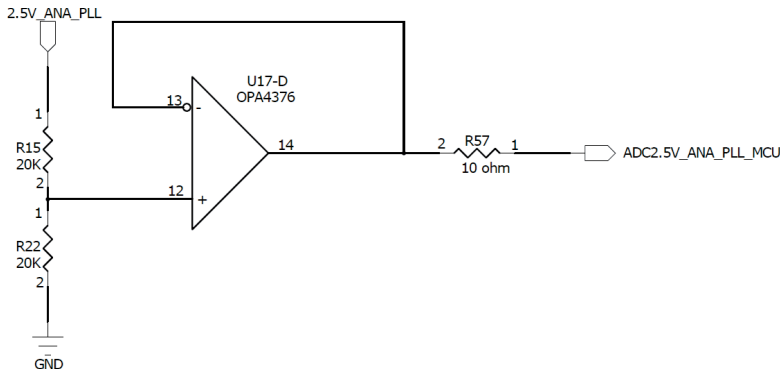


Figure 5.8: Monitoring circuit for the 2.5V voltage generated on the DB. A voltage converter serves as an input for an operational amplifier which works as an impedance converter. The output of the full circuit ranges at 1.25V and thus matches the MibADC input requirements. Graphical adaption from the electronics design file [Kol12].

voltage converter circuits. Tolerances in the actual values, however, may change the nominal values slightly. Therefore, they are determined with a digital multimeter [28] for every MCUB.

All available monitoring values are read out by processing an SBC script. Once the HV characterisation is done, and the configuration characteristics exist in a configuration file on the SBC, the HV can be set exactly. It is varied over several values and the monitoring test script is executed each time. The monitoring HV value should react on these changes, whereas all other values should remain constant.

monitored value	$U_{mon}(A_{DIG}) = A_{DIG} \cdot \frac{2.5V}{1024} \cdot \dots$	nom. A_{DIG}
VCC_ANA_2.5V	$\dots \cdot \frac{R15+R22}{R22}$, with $R15 = R22 = 20 \text{ k}\Omega$	512
VCC_1.2V	$\dots \cdot 1$	492
VCC_3.3V	$\dots \cdot \frac{R13+R19}{R19}$, with $R13 = 16.5 \text{ k}\Omega$, $R19 = 10 \text{ k}\Omega$	510
VCC_PLL_1.2V	$\dots \cdot 1$	492
-3.3V_ANALOG	$\dots \cdot \frac{R44+R45}{-R45}$, with $R44 = R45 = 10 \text{ k}\Omega$	676
+3.3V_ANALOG	$\dots \cdot \frac{R42+R43}{R42}$, with $R42 = R43 = 10 \text{ k}\Omega$	676
12V_ANALOG	$\dots \cdot \frac{R40+R41}{R40}$, with $R40 = 3.9 \text{ k}\Omega$, $R41 = 22 \text{ k}\Omega$	740
$U_{HV,mon}$	$\dots \cdot \frac{100 \text{ k}\Omega}{100 \text{ k}\Omega + R59}$, with $R59 = 100 \text{ k}\Omega$	819
U_{Tmon}^{int}	$\dots \cdot \frac{R16+R24}{R24}$, with $R16 = 6.04 \text{ k}\Omega$, $R24 = 20 \text{ k}\Omega$	264
U_{Tmon}^{ext}	$\dots \cdot \frac{R4+R6}{R6}$, with $R4 = 6.04 \text{ k}\Omega$, $R6 = 20 \text{ k}\Omega$	264

Table 5.1: Monitored voltages, the formulae to convert the digitised values A_{DIG} of the ADC to the corresponding voltages U_{mon} and the nominal values for A_{DIG} . The notation for the resistors is chosen following the schematics of the MCUB [Kol12]. The nomenclature for the voltages is chosen according to the schematics of the DB and the MB [Kol12]. The nominal values for the HV and the temperatures are given at $U_{HV} = 1000 \text{ V}$ and $T = 21 \text{ }^\circ\text{C}$, respectively.

```
1 # sh monitoring_check_system_test_v3.sh 11-11-03
   _monitoring_SETUP23_1000HV.log
2 FPGA monitoring
3 2.5V PLL
4 01FD # 509 (512)
5 1.2V Core
6 01E6 # 486 (493)
7 3.3V IO
8 01F7 # 503 (512)
9 1.2V PLL
10 01E7 # 487 (492)
11 Motherboard monitoring
12 -3.3V analog
13 0242 # 578 (676)
14 3.3V analog
15 029D # 669 (676)
16 12V analog
17 02D2 # 722 (740)
18 HV
19 0331 # 817 (819)
20 Temperature
21 mcu temp
22 0115 # 277 (264)
23 ext temp
24 010E # 270 (264)
```

Listing 5.9: Output of the initial monitoring test for Setup 23. The hexadecimal values were manually converted to decimal numbers in this example and are shown next to the hash symbols. The nominal values are given in brackets. The measured values obtained for HV and temperature refer to 1000 V and a laboratory temperature of 21 °C respectively.

5.12 Temperature Dependence

Many electronic features depend on the surrounding temperature. Therefore, the functional dependence of the parameters obtained in the different full system tests on the temperature needs to be determined. At the time of this thesis, this has not yet fully been done and is recommended for future measurements.

The most critical part is the stability of the HV for the PMT at changing temperatures. This was investigated with a deployed MD module in 2012 and is described in Section 6.5.

5.13 Triggers to the AMIGA MD Modules

5.13.1 Internal Trigger

During DAQ, the AMIGA MD modules are triggered by an external signal from the associated SD station. In addition, an independent internal trigger was implemented in the FPGA firmware [s3]. This trigger can be used to verify the basic functionality of the detector directly after deployment and, later on, for calibration purposes in dedicated calibration runs. The internal trigger is also used to investigate detector

properties and it was used for data taking runs in periods in which the external trigger was not yet available.

The internal trigger is generated, if a signal is detected on n or more input channels on the same sampling edge. The minimum occupancy of signals n is adjustable. The trigger will be referred to as n -fold occupancy trigger or occupancy n trigger in the following.

An initial detector check based on the internal trigger was developed and is described in [Pon11]. This test can be executed during module deployment at the experimental site. The test ensures that the dome, which covers the electronics and the PMT, is closed, so that no light enters, and that the detector shows a qualitatively correct behaviour.

In the test, the DACs of the ABs are programmed such that they provide a threshold of approximately 50 mV to the comparators. The prescaler is disabled and the FPGA is configured to accept data from all channels. The occupancy level is set to a value different from 1 initially, e.g. $n = 8$. If now the trigger rate is monitored, it should be 0 Hz as long as there is no HV set to supply the PMT. Once the high voltage is set, the rate should increase to a stable value. This rate is to decrease again if the thresholds or the occupancy level n are increased. Both dependencies are checked for. The initial detector check also includes a check of the external trigger, which will be described in the following section.

If the detector passed this first test, it is verified that the communication with the underground electronics is possible, that the HV can be set for the PMT, that the thresholds can be set on the ABs, and that the external trigger line is connected correctly.

5.13.2 External Trigger

In order to provide additional information to that obtained by the existing SD array of the Pierre Auger Observatory, the AMIGA MDs need to be synchronised with this array. The technical implementations, both in software and in hardware, will be described in this section. Some modifications have to be made to the SD hardware and to the SD firmwares for the FPGA and the microcontroller on the FEB and on the unified board (UB).

A schematic view of the trigger generation and a CDAS-based event request to an AMIGA MD is given in Figure 5.9. The readout electronics of an MD module is permanently recording data in a ring buffer. After recording a surface event, the SD electronics generates a fast trigger pulse, the T1 pulse, followed by a 24-bit local timestamp (LTS) (step 1 in Figure 5.9). Furtheron, the full sequential signal will be referred to as modified T1 trigger signal. It is sent to the MD underground electronics on a dedicated trigger line. An example of a modified T1 trigger signal is shown in Figure 5.10. The LTS is generated inside the FPGA on the UB of the Local Station (LS). It is a 24-bit free-running counter driven by a 1.25 MHz clock [Wai11]. Thus, the timestamp value is unique for 13.4 s, which suffices to uniquely label at least 1024 muon events with it.

Inside the LS, an interrupt request is given to the microcontroller on the UB. Subsequently, the microcontroller will generate another 24-bit timestamp, based on the GPS signal from the GPS module. This GPS timestamp (GTS) is sent to the FPGA

on the FEB of the SD station again. The FPGA combines LTS and GTS to one 48-bit word, which stores the LTS on the first 24 bits and the GTS on the last 24 ones. The combined signal is then sent to the AuxSBC and stored there (step 2 in Figure 5.9). An interrupt signal is given to the SBC, which subsequently reads the timestamp pair. It is then stored in a look-up table, that holds the last 2048 consecutive timestamps pairs (step 2 in Figure 5.9).

Once there is a T3 event request sent via a radio network by the CDAS to the SD station (step 3 in Figure 5.9), a software module inside the AMIGA SBC filters the GPS information of the request out of it. Therefore, the incoming radio signals are permanently scanned inside the SBC. Using the timestamps look-up table, the received GTS can be translated to an LTS and an event request based on this LTS is proceeded to the underground electronics of the MD module via the usual CAN bus. AMIGA MD events can now be assigned to Auger SD events. A search routine inside the AMIGA DAQ FPGA firmware [s3] is invoked. It finds the event that carries the requested LTS and returns it to the SBC (step 4 in Figure 5.9). The SBC finally sends the event to the CDAS (step 5 in Figure 5.9).

It is essential that the LTS information in the two signals T1+LTS and LTS GTS are identical. Otherwise, the event cannot be found by the AMIGA FPGA and the data is irrecoverably lost. To avoid this, the identity was verified in field and in laboratory measurements, which are described in Section 6.3.2.

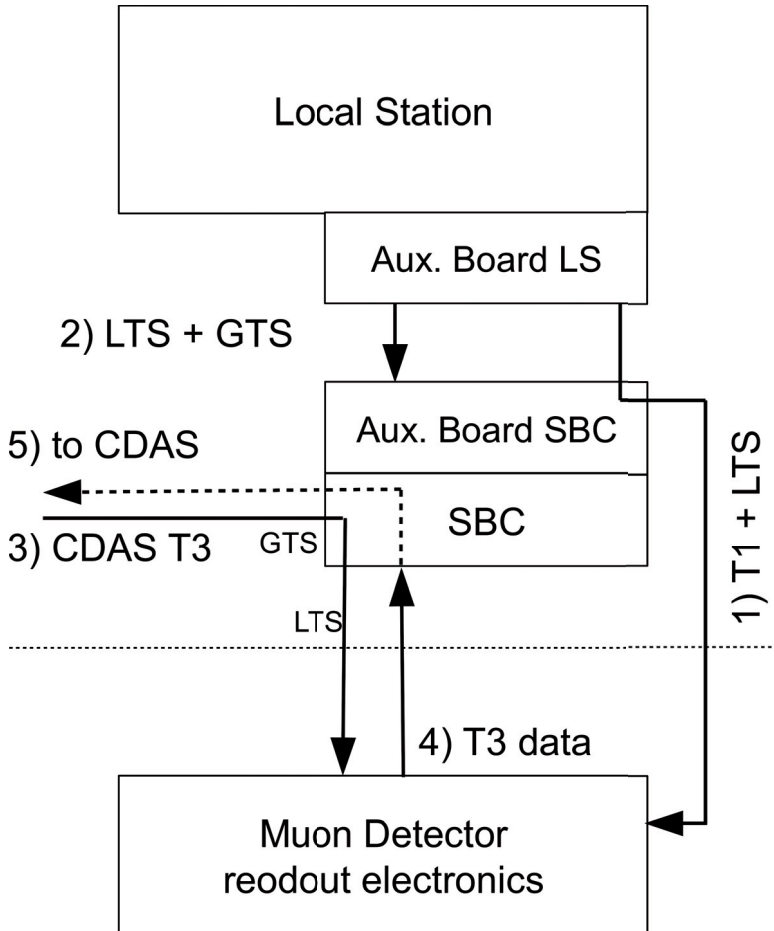


Figure 5.9: Schematics of the handling of an external trigger and the processing of an CDAS event request in a AMIGA MD module.

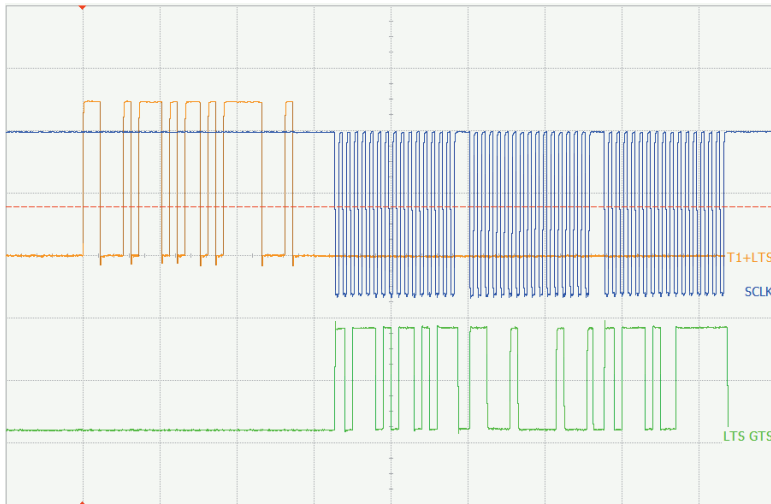


Figure 5.10: Trigger signals for the AMIGA electronics. The modified T1 trigger signal T1+LTS, consisting of T1 pulse and a 24-bit local timestamp, is shown in the left-hand orange curve (1 V / div., 1 μ s / div.). Signals on the data line of the SPI bus on the AuxSBC are shown as LTS GTS in light green on the right-hand side. In 48 bits, the local timestamp LTS and the GTS are transmitted here (2 V / div., 1 μ s / div.). The signal is evaluated on the rising edges of the SCLK signal, which is shown in dark blue on the right-hand side (1 V / div., 1 μ s / div.). The signals LTS GTS and SCLK are skewed by 140 μ s with respect to the first rising edge of the LTS+GTS signal.

5.14 Detector Calibration

The amount of background muons, that pass the detector, is a physics quantity, independent of the detector. It is thus constant for each scintillator strip of all AMIGA MD modules. Assuming a background muon flux at sea level of $I_{s.l.} \approx 1 \text{ cm}^{-2}\text{min}^{-1}$ [Ber12, Gru93] for a horizontal detector and a minimum muon momentum of $E_{\mu} > 1 \text{ GeV}/c$, the expected muon rate per scintillator strip of the area $A_{strip} = 4.1 \text{ cm} \times 400 \text{ cm} = 1640 \text{ cm}^2$ amounts to

$$r_{strip} = I_{s.l.} \cdot A_{strip} \approx 27 \text{ s}^{-1}. \quad (5.8)$$

This expected background rate adds to the noise level, that is generated by the MD detector. The resulting signal rate distribution is a property of the detector and is used for calibration.

The laboratory based characterising tests of each component of the complete detector, consisting of scintillator, PMT and electronics, ensure the functionality of each part of the detector. Combining these characteristics results in a description of the full detector. The calibration procedure presented here aims at determining the properties of the detector in one step.

A repetition of the calibration at regular intervals is recommended to study possible fluctuations and deviations from the initially determined parameters. The calibration results with respect to seasonal and environmental conditions still need to be studied.

The recalibration measurements are a basis to ensure a well-operating system over long terms. Finally, if fluctuations or ageing processes are detected, the recalibration measurements are a basis to account for those.

The signal rate r_i per channel i as a function of the adjusted threshold on the DAC of the AB was found to be a characteristic measure of the fully assembled muon detector. By executing an SBC script, the HV for the PMT is set to $U_{HV} = 1000 \text{ V}$, the first threshold from a parsed list is programmed to the DACs and the FPGA is configured to generate internal triggers upon signals on channel 0 only. Thus, the occupancy trigger is activated with $n = 1$ for a given time and the amount of triggered events during that time is recorded. The next channel is activated and the procedure is repeated until the rate for all channels is determined for the first threshold. The next threshold is programmed into the DAC and the rates are determined again for this threshold. The procedure ends after all channels have been measured for each threshold from the list.

Exemplarily, Figure 5.11 shows the measurement results for PMT channel 41 of the MD module with electronics Setup 7, which is deployed at the SD station *Phil Collins*.

With rising threshold, the signal rate $r_i(x)$ decreases. An exponential fit, following Equation 5.9, is performed. The resulting fit parameters, which are the slope p_0^i and the constant p_1^i , represent the individual channel characteristics:

$$r_i(x) = \exp [p_0^i \cdot x + p_1^i], \quad (5.9)$$

with x describing the threshold in units of programming code (compare Section 4.4.1), the fit parameters p_0^i and p_1^i and the index $i = 0..63$ for the PMT channel. Only those data points enter the fit, for which the trigger rate counter has not yet exceeded

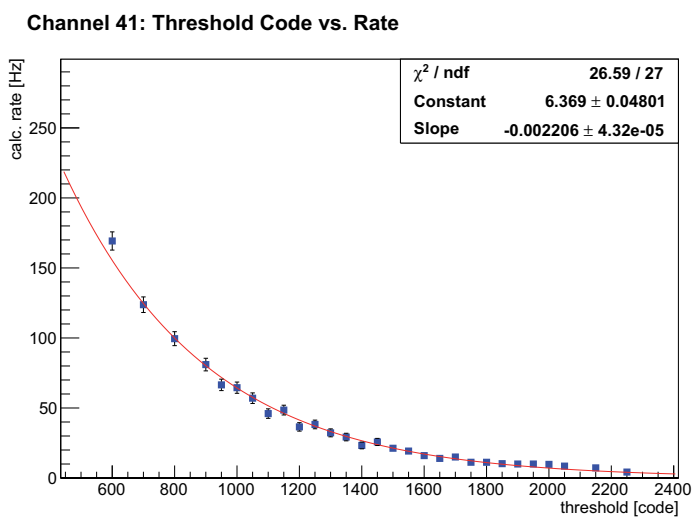


Figure 5.11: Signal rate $r_{41}(x)$ of channel 41 of the MD module with Setup 7 installed as a function of threshold at the comparator level on the board board. An exponential curve following Equation 5.9 is fitted to the data. Looking at the measurements for all channels, it was found, that the dependence steepens for the threshold codes and higher rates. The exponential function thus does not properly describe the data in this region and could be improved e.g. by a double exponential function. However, in total, the exponential seems to be a good starting point.

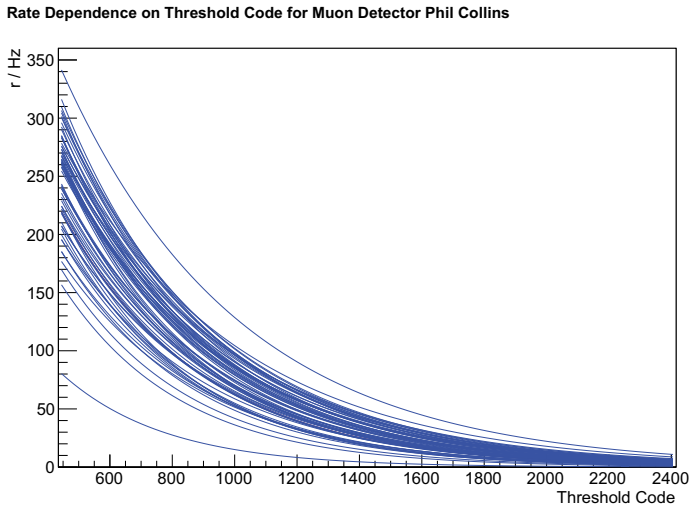


Figure 5.12: Distribution of the fit functions for all 64 channels of the MD module associated with the SD station *Phil Collins*. The fits were performed on data of a calibration measurement of the 29th of February 2012.

its maximum of 1024 Hz. The reason for this limitation is the implementation of the counter as a 10-bit number in the FPGA. The parameters are finally copied to a configuration file on the SBC.

The distributions of the fit functions for all channels of Setup 7, installed at the SD station *Phil Collins*, is shown in Figure 5.12. The distribution shows a wide spread of the functions for the different channels and thus emphasises the need for an individual treatment of the channels.

It is now possible to set the thresholds of the DACs according to a given rate per channel. For this, an SBC script needs to be executed, which itself invokes an SBC application, using the parameters from the configuration file and the required rate.

Chapter 6

Results

The readout electronics, which was partially developed and completely produced and tested in Siegen, is now installed at the experimental site in Argentina as part of the muon detector (MD) modules of the pre-unitary cell (PUC) of the Auger Muon and Infill for the Ground Array (AMIGA) enhancement of the Pierre Auger Observatory.

In the first part of this chapter, the results obtained in the full system tests are summarised. The systems under test were the first of their kind ever built. The results of the tests thus may serve as reference values for future productions.

Since a malfunctioning of a few channels in the test stand was detected in 2012 (Section 5.1), this malfunctioning and its consequences on the evaluation of the tests are discussed first in Section 6.1.

From 2009 onwards, data taking has taken place. Starting in June 2012, the MD was operated in synchronised trigger mode with the existing surface detector (SD) array. Only then it became possible to combine the data of the two detector systems. In Section 6.3, a test is presented, which evaluates the percentage to which the synchronisation works on the earliest level in which the electronics is directly involved. This test also serves as an indicator for the quality of the software and firmware modules involved.

A method for the detector calibration was developed in parallel (Section 5.14), its results are discussed in Section 6.4. A measurement of the stability of the high voltage (HV) for the photo multiplier tubes (PMTs) is presented in Section 6.5.

In the last part of this chapter, starting with Section 6.6, a combined analysis of MD and SD data, recorded between June and October 2012, is presented. With N_{Trig} , being the number of detected pulses in a certain period of time, a direct observable is defined, which is a measure for the signal strength on module level in an event recorded with an MD module. This observable does not depend on any interpretations obtained in simulations but can directly be extracted from the recorded data. The procedure is described in Section 6.6.7.

N_{Trig} is then compared with the signal strength measured in the SD station associated to the respective MD module. In order to avoid effects of signal saturation close to the shower cores, the reconstructed lateral density function (LDF) is evaluated at the position of the respective SD stations instead of using the raw data. Since muons are, in general, mainly responsible for the signal in the SD stations, a correlation be-

tween the signal strength in the SD data and in the MD data is expected. The results of this analysis are discussed in Section 6.6.8.

6.1 Test Stand

In 2012, more than 20 electronics readout systems were produced. The resulting data were looked at with attention to systematic effects which could possibly originate from the test stand devices themselves (Section 5.1).

The break between the production for the MD prototypes and a possible future mass production was used to perform concluding measurements on the test stand. The complete internal resistance of the individual channels was therefore measured multiple times. The waveform generator [4] was disconnected and the detached cable was connected to a multimeter [28]. The second probe was consecutively connected to the corresponding channel on the test stand interface board (TIB). The channels were selected and the resistance was recorded. This measurement was repeated various times.

In order to avoid systematic effects of the multimeter, the measurement was also performed with another device [29], implementing a four-point measurement, with identical results. The measured values of the internal resistances per channel are shown in Figure 6.1.

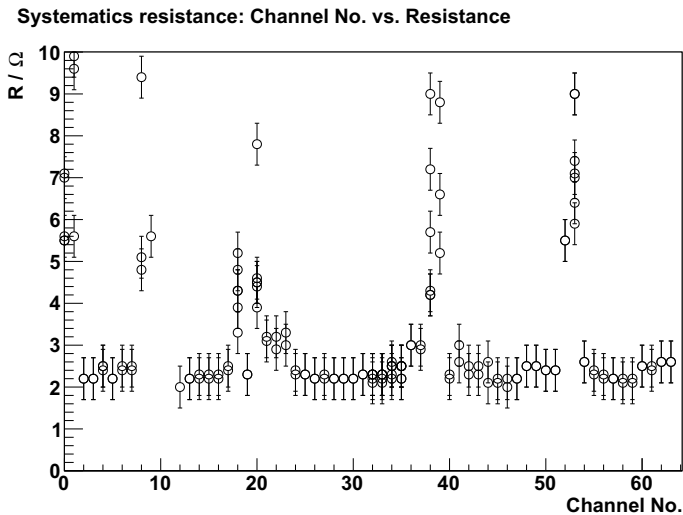


Figure 6.1: Various measurements of the internal resistance of the test stand. The error of a single measurement amounts to $0.1\ \Omega$ and is due to the uncertainty of the digital multimeter [28].

Each switching contact inside the multiplexing unit should provide an internal resistance of less than $1\ \Omega$ and a lifetime in the order of 300,000 switching operations [Agi12]. Thus, by cascading three switching contacts per channel (Figures 5.1(a),

5.1(b) and 5.1(c)), the expected internal resistance of one channel should be below $3\ \Omega$.

In the measurements, most of the channels showed internal resistances below $3\ \Omega$. Assuming a tolerance for the additional resistances of the cables and connectors of $0.5\ \Omega$ per channel, two groups of channels can be distinguished: those with $R_{in} < 3.5\ \Omega$ and those with $R_{in} > 3.5\ \Omega$.

Channels belonging to the first group behave in agreement with the datasheet information. They are referred to as normal channels. Remeasuring normal channels results again in values for R_{in} below $3.5\ \Omega$. Channels belonging to the second group, on the contrary, behave abnormal. The change of the internal resistance value of an abnormal channel only occurs after switching operations. Values up to the $k\Omega$ range and thus much higher than the limit of the normal values were seen. The measured internal resistance is not stable and may change after a switching operation. It can be assumed, that the quality of the contact within a relay leads to that behaviour. A total amount of 11 channels were found to behave abnormal.

Switching higher currents might clean the contacts from oxide layers within the multiplexer. It is recommended to do this before any further usage of the device. Furthermore, the internal resistances should be monitored during a possible mass production by repeating the measurement described above.

Results of the characterisation tests originating from the threshold scan were calculated while underestimating the internal resistance with $R_{in} = 0$. The exact status of the internal resistances of the abnormal channels at the time of the system characterisation is not known. Therefore, the obtained results for these channels cannot be corrected. Corrections can be applied, however, to the results of normal channels. The input circuit is represented in Figure 6.2.

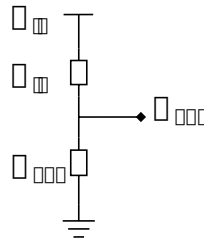


Figure 6.2: Input circuit used for the tests that are to characterise the readout electronics. $R_{out} = (71.8 \pm 0.1)\ \Omega$, R_{in} depends on the channel. V_{out} is used as input for the readout electronics.

The voltage V_{out} , that enters the readout electronics, is the voltage which drops at R_{out} . It can be determined through Equation 6.1:

$$V_{out} = \frac{R_{out}}{R_{in}^i + R_{out}} \times V_{in} =: r_i \times V_{in}, \quad \text{where } i = 0 \dots 63. \quad (6.1)$$

From Figure 6.1, the mean value for the resistance of normal channels can be derived to be $R_{in}^{mean} = (2.40 \pm 0.01)\ \Omega$ and with $R_{out} = (71.8 \pm 0.01)\ \Omega$, the correction factor becomes $r_i = 0.97$.

That means: thresholds, which are set to reject pulses with amplitudes below V_{in} , actually reject pulses with the lower amplitude $r \times V_{in}$ and hence, more pulses will pass the cut. To overcome this, the threshold has to be raised by a factor of $1/r$.

6.2 Results of the Full System Tests

6.2.1 Channeltest and Crosstalk Test

Every setup under test is required to pass the initial tests described in Sections 5.2 to 5.5 before the sequence of tests is continued with the threshold scan.

All setups passed the channeltest. Solely in Setup 26 two channels were detected to be short-circuited. These channels could not be recovered. In the crosstalk test, a lower limit for the thresholds was determined at which no electrical crosstalk appears yet. The distribution of the threshold limits is given in Figure 6.3 for the setups 1 and 6 to 26, excluding Setup 21 for which the threshold scan failed. The setups 2, 3 and 5 were already deployed when the final crosstalk test was not developed yet. Setup 4 was shipped to Argentina before the completion of all tests.

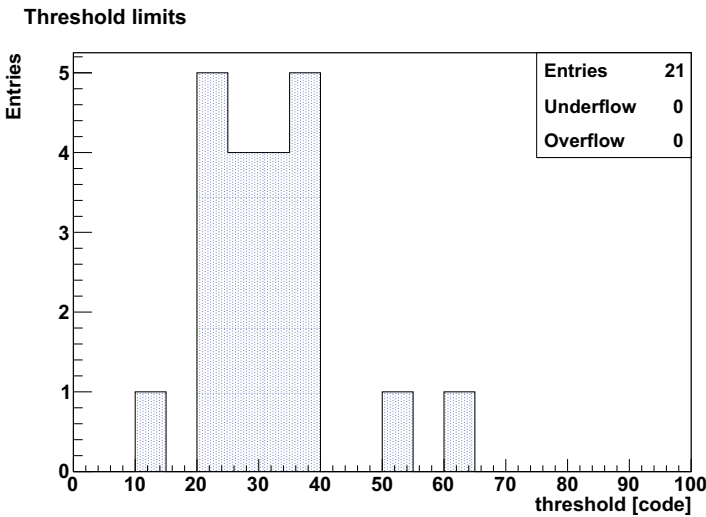


Figure 6.3: Distribution of the minimal thresholds for which no electrical crosstalk could be observed yet. The thresholds were adjusted at the DACs of the ABs.

For all channels the region, in which electrical crosstalk needs to be taken care of, ranges well below any threshold, that corresponds to trigger rates of physically interesting values. Aiming at e.g. 100 Hz per strip results in threshold values above 400 in units of programming code (Figure 6.15). Therefore, electrical crosstalk does not affect the data acquisition.

6.2.2 Threshold Scans

The aim of the system tests is to assure the full functionality of an electronics readout system after assembling the single boards and to characterise the system.

It was planned to obtain a precise conversion function between the programming code for the threshold voltage of the DACs on the ABs and the threshold voltage itself for every individual channel. The corresponding threshold scan was performed using the test stand as described in Section 5.1. However, the analysis of the internal resistances of the test stand revealed unexpected deviations from the expected values for eleven channels, which forbids the interpretation of the obtained data as the correct conversion functions.

A measurement of a single channel can consist of several remeasurements due to the test being halted for any reason and then continued. Since, in the first instance, it was assumed, that the test stand provides constant conditions to the electronics, the different measurements could be used as one dataset. Figure 6.4 shows the different measurements, that were performed for channel 54 of Setup 11. At least three data points per measurement are required before a linear fit is performed. It was found that different measurements may result in incompatible results for the linear fits. It is likely that this behaviour does not originate from the electronics under test but from the test stand and/or the interconnections to the electronics. It is recommended to improve the electrical interconnection between the TIB and the readout electronics in further measurements if a precise characterisation is required.

The ranges of thresholds that were scanned are comparable for Setup 2 and from Setup 5 onwards, excluding Setup 21. Setup 1 is used in a laboratory setup in Siegen, which was installed before the development of the final threshold scan. Setup 3 and Setup 4 were shipped to the experimental site in Malargüe before the completion of the test. For Setup 21, the thresholds could not be programmed anymore after the assembling. This setup was therefore held back. In Setup 9 and Setup 15, on ABs 1 and 3, respectively, the reference voltage for the threshold voltages could not be programmed anymore after the assembling and thus, the thresholds could not be varied. These setups could be used at the experimental site when excluding the non-operational channels from data taking. However, it was decided not to use them there but to use them as laboratory setups to support e.g. the development of the trigger processing software or the firmware for the field-programmable gate array (FPGA) of the digital board (DB).

In the Figures 6.5(a) and 6.5(b), the distribution of the fit parameters of all threshold scans, slope and offset, are shown. Gaussian distributions around the nominal values of 2 mV^{-1} and 0 are expected. The slope parameter shows an asymmetric distribution below the nominal value with an overpopulation of the left tail. The offset parameter shows an almost Gaussian distribution around value for the offset of about 17. The scatter plot of the two fit parameters (Figure 6.5(c)) shows no correlation between the two of them. Only normal channels are shown, i.e. channels for which the internal resistance in the test stand ranges below $R_{\text{in}} = 3.5 \Omega$.

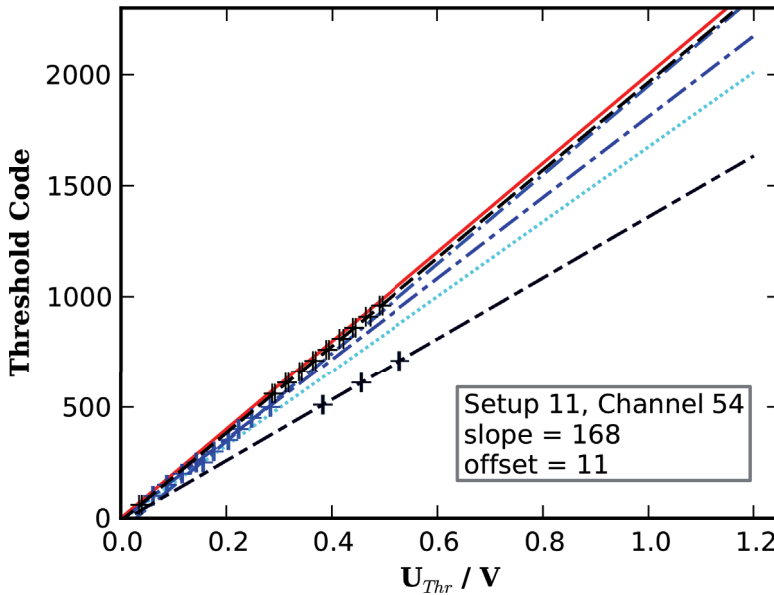
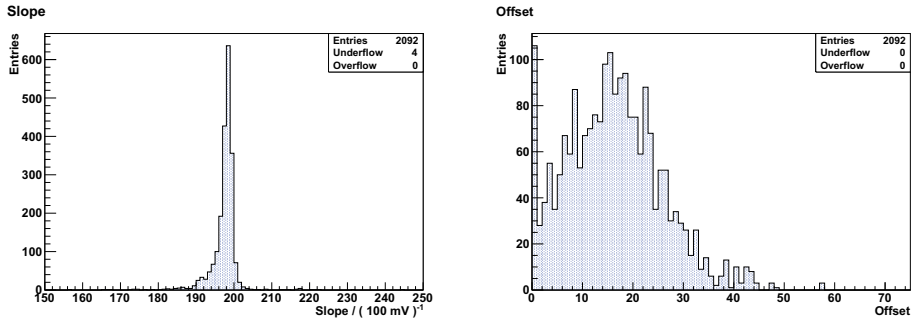
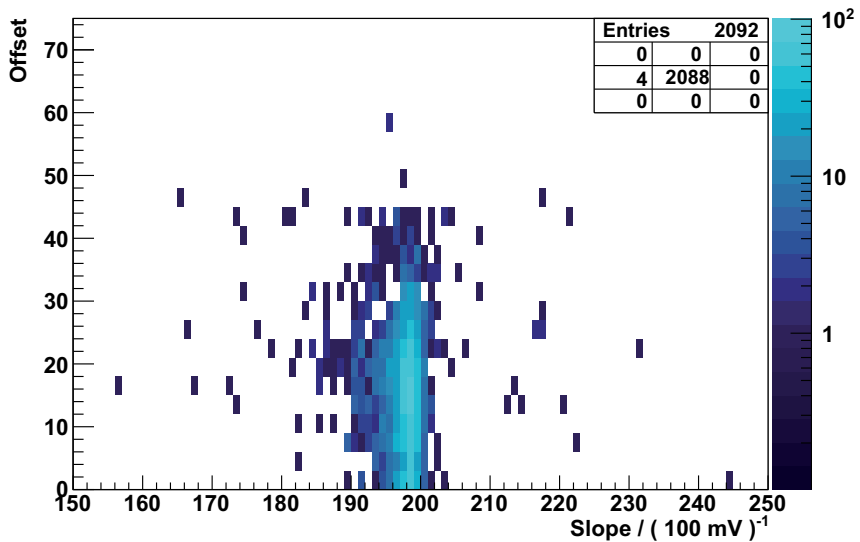


Figure 6.4: Results of the threshold scans performed for channel 54 of Setup 11. Different measurements are represented by different dash-dotted blue lines. The solid red line represents the theoretical expectation as given in the data sheet of the DAC [27] on the ABs. All measurements are compatible with a linear function but the linear functions are incompatible amongst each other. The dotted light blue curve is a fit to the combined measurements, which does not describe the full data. The linear behaviour can be verified through the threshold scan whereas the precise characterisation is not possible. Since an independent procedure was found to calibrate the detector (Section 6.4) it is acceptable to discard the characterisation in the threshold scans.



(a) Slope parameters from the linear fits. (b) Offset parameters from the linear fits.

Slope vs. Offset



(c) Scatter plot for the two fit parameters.

Figure 6.5: Results of the threshold scans. (a,b) Distribution of the fit parameters of the linear fits for all channels and all setups under test. (c) Scatter plot for the fit parameters slope and offset. Only channels are shown for which the internal resistance in the test stand ranges below $R_{in} = 3.5 \Omega$ and which are defined as normal channels.

6.2.3 Monitoring Voltages and Temperatures

The full monitoring test was developed in 2011. Therefore, full data are available only for setups 1, 9 and 14 to 26. The monitoring part of the other setups, however, was checked for functionality without further characterisation. Since the test foresees a repetition with different HVs set, more than one dataset per setup and monitored voltage exists.

Table 6.1 lists the mean values of the voltages, that enter the monitoring circuits, as measured with a multimeter. The mean values of the monitored analogue voltages (entries 5 to 7 in the table) significantly deviate from the nominal values. However, the deviations are well within the specifications of all supplied components in the analogue circuits and therefore constitute no constraint to the functionality.

monitored voltage	$\langle U_{mon,meas.} \rangle / V$	$U_{nom.} / V$
VCC_PLL_2.5V	2.499 ± 0.003	2.5
VCC_PLL_1.2V	1.196 ± 0.003	1.2
VCC_3.3V	3.285 ± 0.003	3.3
VCC_1.2V	1.200 ± 0.003	1.2
-3.3V_ANALOG	-3.184 ± 0.003	-3.3
+3.3V_ANALOG	3.281 ± 0.003	3.3
12V_ANALOG	11.799 ± 0.003	12.0

Table 6.1: Mean monitored voltages (U_{mon}) as determined in 15 single measurements with a digital multimeter. The nomenclature is chosen according to the schematics of the DB for the first four entries and according to the schematics of the MB for the last three entries [Kol12].

To obtain the precision of the voltage monitoring in units of ADC counts (analogue-to-digital converter), the differences between the expected values and the ADC values, as read out with the microcontrollers, are calculated. The expected values therein are derived from measurements of the voltages with a digital multimeter [28] and a reconversion to ADC counts following Table 5.1.

The distribution of the differences is shown in Figure 6.6 for the voltages listed on positions 1 to 4 in Table 5.1. These voltages are generated on the DB and are referred to as digital voltages in the following.

The same ADC is used inside the multi buffered analogue-to-digital converter (MibADC) of the microcontroller for all input voltages. This way, a combined evaluation is possible. A Gaussian was fitted to the distribution. For the digital voltages, the width of the Gaussian is

$$\sigma_{mon,dig} = 2.3 \pm 0.2 . \quad (6.2)$$

The same analysis is repeated for the second class of voltages listed as entries 5 to 7 in Table 5.1. The distribution of the differences between expected and measured ADC values are shown in Figure 6.7.

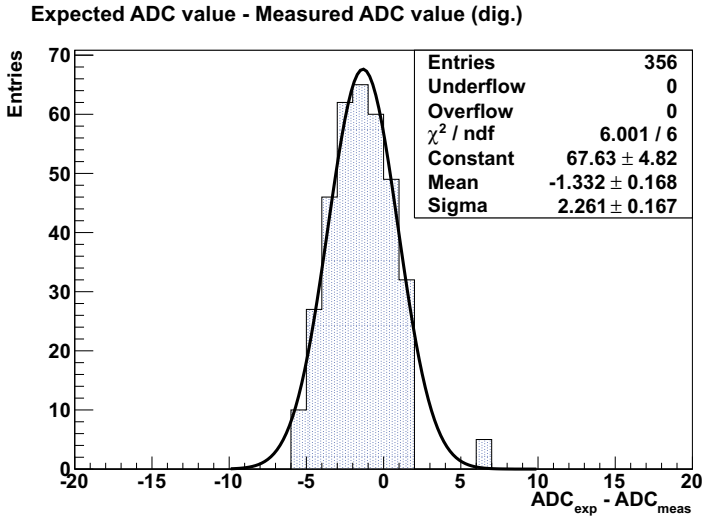


Figure 6.6: Precision of the monitoring part for the digital voltages. A Gaussian was fitted to the distribution of the differences between expected and read out ADC values. The expected value was calculated taking into account the voltage that was measured with a multimeter and which was then converted using Table 5.1. The width $\sigma_{mon,dig} = 2.3 \pm 0.2$ of the Gaussian serves as an estimator for the precision of the monitoring circuits.

The underflow in the distribution originates from the monitored analogue 12 V (last entry in Table 5.1) in all six measurements for Setup 19. Here, the mean voltage, as reconverted from the ADC values, ranges below 10 V. The voltage measured with a multimeter, instead, resulted in (11.82 ± 0.01) V, which hints at a voltage drop in the monitoring circuit.

Again, a Gaussian fit was performed to the distribution. The width of the Gaussian results in

$$\sigma_{mon,ana} = 3.8 \pm 0.3 . \quad (6.3)$$

The two classes of voltages are separated since they are generated with different precision on different boards. Voltages belonging to the first class supply digital components on the DB and therefore need to be more stable. Those components supplied with voltages from the second class tolerate a larger variance.

The distributions are expected to have a mean value around zero. However, the two distributions show systematic shifts of their mean values to $\text{mean}_{dig.} = -1.3 \pm 0.2$ and $\text{mean}_{ana.} = -1.5 \pm 0.3$, respectively. This translates into an effect in the determination of the monitored voltages in the order of $\mathcal{O}(2.5 \text{ V} / 1024) = \mathcal{O}(1 \text{ mV})$ (Table 5.1). This uncertainty is irrelevant for the overall functionality of the electronics. The origin of the effect is located in the level of the reference voltage U_{REFHI} (Equation 5.7). A voltage drop in the range of mV does explain it completely. Example measurements on five microcontroller boards (MCUBs) resulted in a average reference voltage of $\langle U_{REFHI} \rangle = (2.4942 \pm 0.0004) \text{ mV}$ with an uncertainty of 1 mV for a single measure-

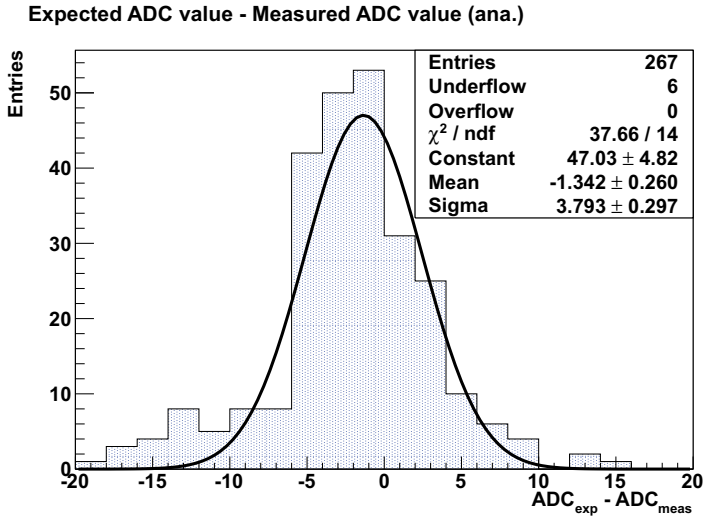


Figure 6.7: Precision of the monitoring part for the analogue voltages. A Gaussian was fitted to the distribution of the differences between expected and measured ADC values. The expected value was calculated taking into account the voltage that was measured with a multimeter. The width $\sigma_{mon,ana} = 3.8 \pm 0.3$ of the Gaussian serves as an estimator for the precision of the monitoring circuits.

ment. Variations in this range may occur already due to temperature changes below 25°C [17].

The calculated widths of the distributions prove, that the circuits are sufficient to monitor the correct functionality of all voltages during data acquisition (DAQ) with a resolution of a few ADC counts. Severe voltage drops, which could limit the functionality, can be detected with the system. The smaller width of the distribution of the digital voltages compared to the one of the analogue voltages shows, that the digital voltages are generated with less tolerances.

6.2.4 High Voltage Characterisation

In Table 6.2, the results of the HV characterisation for the single setups are given. The dependence between the programming value $code_{HV}$ and the resulting HV output U_{HV} is described by Equation 5.5 (Section 5.10). The fit parameters as shown in the table can be used to adjust precise voltages to the PMT. All 25 electronics readout systems that were under test passed the HV characterisation. Setup 4 was delivered to the collaborating institute in Buenos Aires before all tests. Two setups, Setup 2 and Setup 3, show noticeable deviating results for the value. This is due to an earlier version of the MCUB with a differently designed control part being part of these systems. The design was changed to allow for a more precise adjustment of the output voltage U_{HV} .

Setup	$Slope_{HV}/V^{-1}$	$Offset_{HV}/1$	Setup	$Slope_{HV}/V^{-1}$	$Offset_{HV}/1$
1	3277	5	14	3301	10
2	1754	6	15	3270	6
3	2158	45	16	3295	14
4	-	-	17	3302	6
5	3316	11	18	3283	0
6	3280	6	19	3298	10
7	3303	13	20	3297	9
8	3305	6	21	3288	6
9	3304	7	22	3289	7
10	3291	13	23	3303	7
11	3292	10	24	3279	4
12	3274	6	25	3287	1
13	3284	5	26	3281	1

Table 6.2: Parameters of the HV characterisation determined for the single setups. Setup 2 and Setup 3 were assembled with a prototype version of the MCUB, which mainly differs in the monitoring circuit and its size from its successors. Different resistors are soldered to the control part of the HV. Setup 4 was delivered to Buenos Aires before any test could be performed.

6.2.5 Power Consumption of the Electronics

The power consumption of the electronics was measured exemplarily with the electronics setup Setup 9 in the laboratory test stand. Supplied with $(24 \pm 0.1)V$, the drawn current was measured as $(217 \pm 1)mA$ when the FPGA on the DB is in an unconfigured state, as $(227 \pm 1)mA$ when the FPGA is configured with the AMIGA data acquisition firmware [s3], and as $(238 \pm 1)mA$ under load, which was simulated by setting the HV to 1000V and by acquiring data with occupancy 0 trigger and the lowest thresholds possible set on the ABs. The power consumption thus ranges between 5.2W and 5.7W.

In these tests, no PMT was connected. However, the power consumption of this device does change the total consumption of the system only in the order of mW.

The power consumption was not recorded for every setup but it was taken care, that a maximum current of 300 mA at 24 V is not exceeded in operation. Higher currents are hints to malfunctions in the electronics.

The surface part of the AMIGA MD electronics, namely the single board computer (SBC) with the controller area network (CAN) module and the auxiliary board SBC (AuxSBC) with its CPLD (complex programmable logic device) configured with the firmware for trigger synchronisation [s1], was measured in the laboratory to consume $(120 \pm 1)mA$ at 24V, i.e. around 3W, in operation.

The batteries, which power the AMIGA MD modules, provide approximately 100Ah

at 24 V [Con12b]. The maximum runtime for a pair of MD surface and underground electronics is therefore about 240 hours, which is sufficient to overcome night times or cloudy days during which the solar panel can not charge the battery at full efficiency.

6.2.6 Addressing of Individual Channels

The nomenclature of the single PMT pixel changes for different stages in the signal processing chain due to the distribution of the development process over different institutes. Be it the channel ordering on the PMT data sheet, the naming of channels on the MB or on the ABs, in the different modules of the FPGA firmware, and finally in the control commands from the SBC: it has to be assured, that the individual channels are addressed correctly. A routine to test the correct addressing of the channels was developed. Firstly, all channels are configured with a high threshold. Then, one threshold is lowered. A pulse, which theoretically can not be seen by the high threshold channels, is sent to all channels consecutively. Only the single channel with low threshold should detect the signal. It was found that all channels behave as expected. Since this test constitutes a test of the firmware and software modules involved rather than a test of a specific single readout electronics, it does not need to be performed for all assembled setups. However, changes in the firmware or software might invoke the need to check the behaviour again, therefore the test is mentioned here.

6.3 Advanced Trigger Tests

The test for external trigger acceptance as described in Section 5.8 was passed successfully by all setups under test. It ensures the functionality of one part of the full signal processing chain of T1 trigger signals. The determination of the event request efficiency combines the Local Station (LS), the auxiliary boards, the SBC and the readout electronics in one test. Besides a check of the functionalities of the actual devices in use, the test also provides information about the quality of software and firmware involved. It is described in the following two sections.

6.3.1 Event Request Efficiency

The synchronisation of a MD module with the associated SD station was tested in two ways in the framework of this thesis.

In the first test, the specially designed pattern board (PaB), an SBC and a waveform generator [4] are used. The setup of the test is given in Figure 6.8. The SBC controls the waveform generator via the serial port. It is connected to the readout electronics through the usual CAN bus. The waveform generator is used to trigger the PaB. The PaB is based on an FPGA. It simulates PMT and trigger signals for the AMIGA readout electronics. The FPGA on the PaB is configured such that 2048 trigger signals, each consisting of a T1 pulse and a known local timestamp, are consecutively sent to the readout electronics after an input signal from the waveform generator is detected. The trigger rate to the readout electronics is set to 100 Hz. The readout electronics is operated in data acquisition mode in the test.

After sending all 2048 trigger signals, the SBC is programmed to request events from the readout electronics. Every 50th event between event number 0 and 2047 is chosen for the request. This procedure constitutes one run, and a sequence of 999 runs is processed. The list of timestamps inside the FPGA is overwritten after each run.

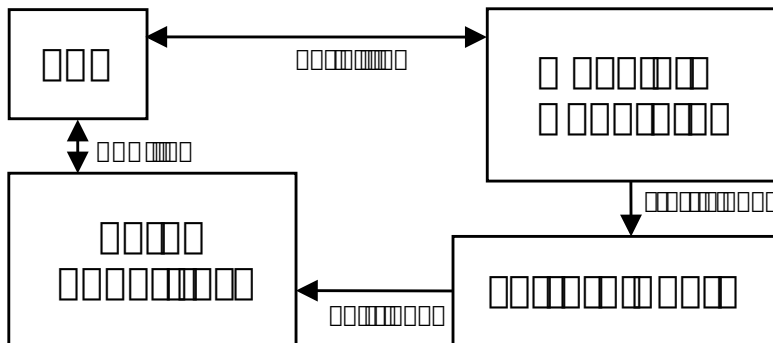


Figure 6.8: Interconnection of the devices used in the trigger test with the pattern board (PaB).

It was found that every event request resulted in a successful readout and storage of the data. The result of this first test is twofold: it can be concluded, that all local

timestamps, that have been sent, are correctly stored inside the FPGA of the DB, and further, that the event identification logic inside the FPGA and the software modules operate as expected.

The second test was performed at the experimental site with the MD module at the SD station *Heisenberg*. The LS electronics, the two auxiliary boards (AuxLS and AuxSBC) and the SBC are thus incorporated in the test. This corresponds to a configuration close to the situation at the experimental site. Figure 6.9 schematically shows the setup of the test. The three PMTs of the SD station constitute the input for the LS electronics. The LS electronics is operated in standard data acquisition mode, which means that the high voltages of the PMTs are adjusted such that a T1 trigger is generated at a rate of approximately 100 Hz. Upon each T1 trigger generation, the LS electronics forms a trigger signal for the MD module. This trigger signal consists of a T1 pulse and a local timestamp generated by a free running counter inside the FPGA of the LS electronics. These signals are provided to the underground readout electronics via the two auxiliary boards. The LS further generates a global timestamp. The pair of local and global timestamp is sent to the SBC, also using the auxiliary boards. The SBC stores the last 2048 pairs in a list. The underground electronics is set into data acquisition mode and stores the last 2048 local timestamps received. From the list of the last 2048 pairs of timestamps in the SBC, every 50th position is chosen for an event request. This constitutes one run. The requests are processed sequentially, starting with the oldest timestamp. For every pair of timestamps, that is stored in the SBC, the corresponding data should be available in the underground electronics. During the event requests the acquisition of new data continues. It is therefore expected that the oldest data are already overwritten by new data when the actual event request is executed. A sequence of 1000 runs is processed.

The number of successful requests against the corresponding event number in the list of timestamps is shown in Figure 6.10. The error is calculated using the method discussed in [UII07]. An error function, following Equation 6.4, is fitted to the data:

$$\text{Erf}(x) = \frac{p_0}{2} \cdot \text{erf} \left[\frac{x - p_2}{p_1} + \frac{1}{2} \right], \text{ with } \text{erf}[u] = \frac{2}{\sqrt{\pi}} \int_0^u e^{-t^2} dt, \quad (6.4)$$

where p_0 , p_1 and p_2 are free parameters for the fit.

The fit results in

$$\varepsilon_{max} = p_0/N = (96.6 \pm 0.08) \% . \quad (6.5)$$

Old events have low event numbers and only fractions of them can be requested successfully as expected. The younger events are requested with a maximum efficiency of $\varepsilon_{max} = p_0/N$, where N is the number of runs. The missing approximately 3 % are lost in the signal processing chain of the timestamp signals. Possible sources of this effect might be located

- in the LS electronics,
- in the AuxSBC, when storing the timestamp pair,
- in the AuxSBC, when providing the timestamp pair to the SBC,

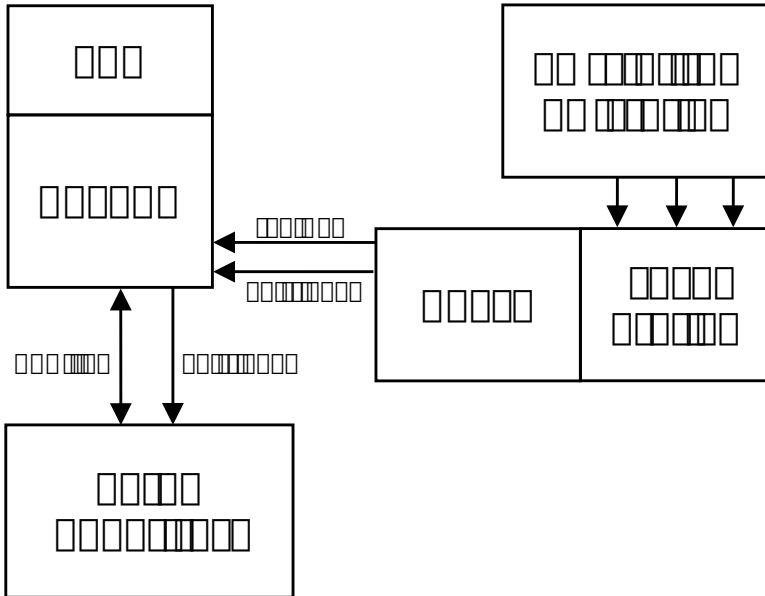


Figure 6.9: Interconnection of the devices used in the trigger test with the Local Station (LS).

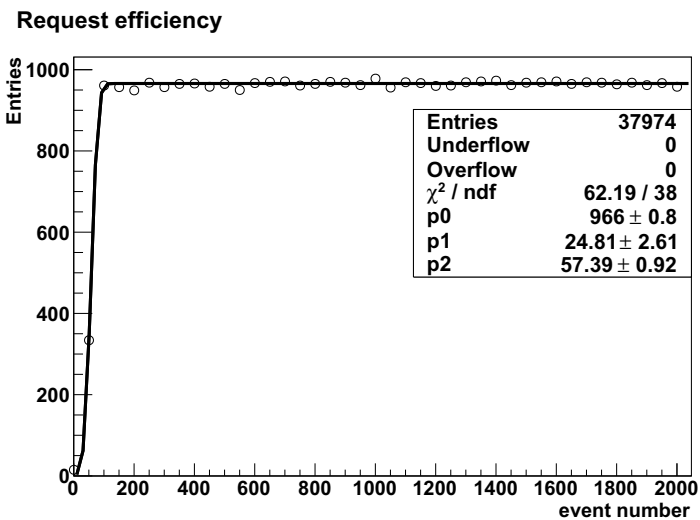


Figure 6.10: Event request efficiency using the modified firmware for the FPGA on the LS. An error function (Equation 6.4) was fitted to the data. The maximum efficiency is determined from the fit parameter p_0 .

- in the underground readout electronics, when it needs to process event requests and data acquisition in parallel,
- or in a combination of the options above.

The first option will be discussed in the next section (Section 6.3.2). It explains the largest fraction of the missing efficiency. Therefore, studies of the other three options are postponed to the future.

The number of events, that are still available for requests, can be derived from parameter $p_2 = 57.4 \pm 0.9$ in the fit. This parameter denotes the position in the timestamps list for which the corresponding event can be requested with an efficiency of 50 %. Assuming a mean trigger rate for T1 of 100 Hz, events recorded within the last 19.4 s are available. This exceeds the storage time of events in the electronics of the SD stations, which ranges at approximately 10 s and is thus fully sufficient.

The parameters p_1 and p_2 heavily depend on the workload on the SBC. If the starting time for an event request is systematically delayed (e.g. by a lot of parallel processes in the SBC), p_2 will increase and the availability of the older events will reduce. If the workload has large fluctuations, the parameter p_1 , describing the width of the slope, will increase.

6.3.2 Local Timestamp Identity in the Trigger Signals

In the previous section, the request efficiency for events, which were stored in the electronics of an MD module, was determined to be $\varepsilon_{max} = (96.6 \pm 0.08)\%$. From the list of possible error sources that cause the missing efficiency, the first item is discussed here.

In Section 5.13.2, the trigger strategy for the MD is described. To associate MD events with the corresponding SD events, it is essential, that the two signals, T1+LTS and LTS GTS as provided by the SD electronics, contain the same information for the local timestamp (LTS). If this is not the case, the MD information of this event is lost since it can not be requested from the electronics. The identity of the two signal parts is tested with the following procedure.

A minimal setup, consisting of the LS electronics [Abr04, Sza09a], a digital waveform generator [4], and a digital multi-channel sampling oscilloscope [7] has been used. The waveform generator is programmed to send inverted pulses with an amplitude of -1.5 V and a width of $1 \mu\text{s}$ at a frequency of 100 Hz to the dynode input for PMT 1.

The LS was configured with modified firmwares [s7] for the FPGA and the microcontroller in order to obtain the trigger signals from the LS. The LS electronics is operated in DAQ mode.

The oscilloscope is programmed to trigger on the rising edge of the T1+LTS signal and to store the data from the three signals. Since the SPI signals LTS GTS and SCLK have a delay of approximately $140 \mu\text{s}$ with respect to the T1+LTS signal, the skew parameter for these two signals is set to $140 \mu\text{s}$ in order to display all three signals on the same screen. An example of the oscilloscope output is provided in Figure 6.11(a). Another example event, generated by the modified firmware is shown in Figure 6.11(b) as the output of the offline analysis application. An algorithm was written to find the sample points at which the signals need to be evaluated. The sample points are represented by asterisks in the figure. The bit mismatch on the last

position between the timestamp strings is observable: the last bit in the T1+LTS is a digital 0, whereas the last bit in the LTS GTS signal is a digital 1.

The data files are analysed offline. The bit string, that follows the 200 ns wide trigger pulse after a break of 300 ns has to be identical to the first 24 bits that constitute the LTS GTS signal. The T1+LTS signal is evaluated at 550, 650, ... 2850 ns after the position at which the first edge is detected in the data. The LTS GTS signal has to be evaluated at the points in time of the first 24 rising edges in the SCLK signal. The LTS GTS signal is generated by an interrupt handler, which is programmed into the microcontroller of the LS electronics. Thus, the distance of time with respect to the T1+LTS signal varies. In the analysis only those events that include the complete timestamp signals were chosen from the full sample (Figure 6.11(b)).

A total amount of 212,007 valid recordings were evaluated from which 6528 recordings were found to contain at least one bit mismatch when comparing the two signals T1+LTS and LTS GTS. The ratio of non-identical events can thus be expressed as

$$r_m = (3.08 \pm_{-0.04}^{+0.04}) \% , \quad (6.6)$$

where the errors are calculated following [Ull07].

The distribution of the positions of the bit mismatches is shown in Figure 6.12 for the modified FPGA firmware [s7]. The least significant bits are mostly affected, which points at instabilities in the signal handling inside the FPGA firmware.

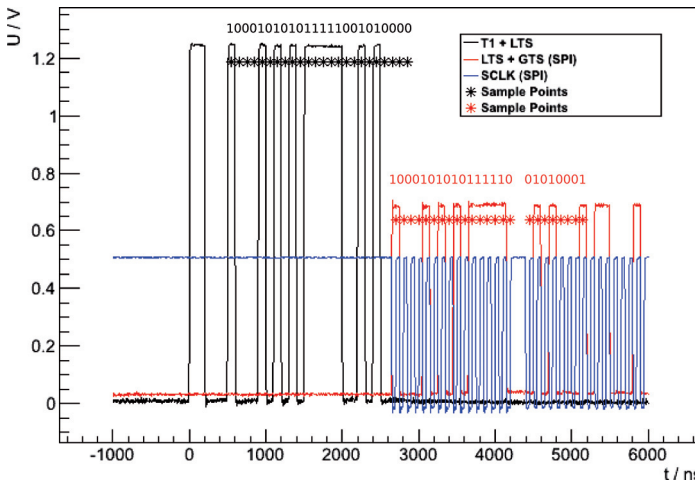
This gave reason for a revision of the firmware in which outputs of state machines inside the FPGA code are latched and the signals are thus stabilised [s5]. The test on the timestamp identity was repeated with the revision. A total amount of 202,484 recordings was evaluated and no bit mismatch could be detected anymore. The ratio of non-identical events thus results in

$$r_r = (0 \pm_0^{+0.001}) \% . \quad (6.7)$$

Based on these tests, it is recommended to apply the corrections on the output of state machines to all parts inside the FPGA firmware and to use the revised modified firmware for future measurements.



(a) An example event as displayed by the oscilloscope. See text for detailed explanations.



(b) Another example event as reconstructed offline. Scale factors of 2, 5, and 5 were applied to the representations of the T1+LTS, the LTS GTS and the SCLK signal, respectively. The sampling points were computed at fixed distances in time with respect to the trigger position for the T1+LTS signal and at the rising edges of the SCLK signal for the LTS GTS signal. The chosen event shows a timestamp mismatch in the two signals on the LSB. The decoded timestamps were added above the curves.

Figure 6.11: Examples of events as displayed by the oscilloscope (top) and as reconstructed in the analysis (bottom).

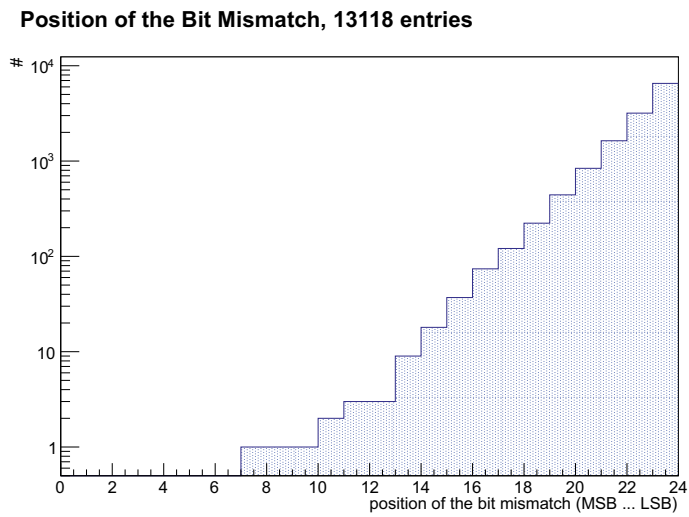


Figure 6.12: Position of the bit mismatches detected in the events that were recorded using the initial modification of the FPGA firmware for the LS electronics. The least significant bits are affected mostly, which points at instabilities in the signal handling inside the firmware.

6.4 Results of the Detector Calibration

The detector calibration (Section 5.14) was performed for all seven MDs of the PUC. An exponential function (Equation 5.9) was fitted to the data of each channel. After the calibration procedure, the rate dependence on the threshold $r_i(x)$ is known for all channels i . The results of the procedure are discussed in the following section.

The recording time per strip and threshold was set to 4 s and threshold codes between 600 to 2250 have been scanned.

The trigger rate is expected to decrease with increasing threshold. It was found in test runs, that random signals with mean rates between 200 to 250 Hz and above may result in numbers that would contradict this expectation. It was therefore decided to exclude data points which show a decrease of the rate at low thresholds. An example of this behaviour is shown in Figure 6.13. The data point at the threshold code 600 was excluded. Since the final external trigger rate will not exceed 200 Hz as a consequence of a limit in the LS electronics of the SD station, the origin of this behaviour was not investigated. Thus, the internal trigger mode may create pathological rates, which will never need to be handled by the firmware of the FPGA on the DB in DAQ mode and for which the firmware was not optimised for.

A list of channels, for which such data points were seen is given in Table 6.3. Results, that are presented in the context of the calibration procedure itself are based on the data that was cleaned from pathological rates.

However, the detectors of the PUC are configured with calibration curves in which also these data points were taken into account. In the analysis presented in Section 6.6, data recorded with the affected channels are therefore ignored.

The MD module associated to *Corrientes* has five channels which have no fibres connected to the PMT to study crosstalk behaviour. These channels can clearly be identified throughout the calibration procedure for they result in exponentials with a low slope. They are also listed in Table 6.3. Since they qualitatively differ from all other channels, they were also excluded from later analysis runs.

The distributions of the fit parameters are shown in Figures 6.14(a) and 6.14(b). The two fit variables are expected to be independent. The scatter plot in contrast shows a negative correlation. This correlation, however, is caused by the tails in the distributions of the two parameters p_0^i and p_1^i only. Cutting on values $p_0^i > -0.003$ and $p_1^i < 7.5$ results in an uncorrelated population.

Generally, the exponential function was found to be systematically too flat for low thresholds. In an improved ansatz e.g. a double exponential function could be introduced to describe the data better.

However, the exponential function is sufficient to describe the rate dependence on the thresholds as a first ansatz in a wide range of thresholds.

Channel 11: Threshold Code vs. Rate

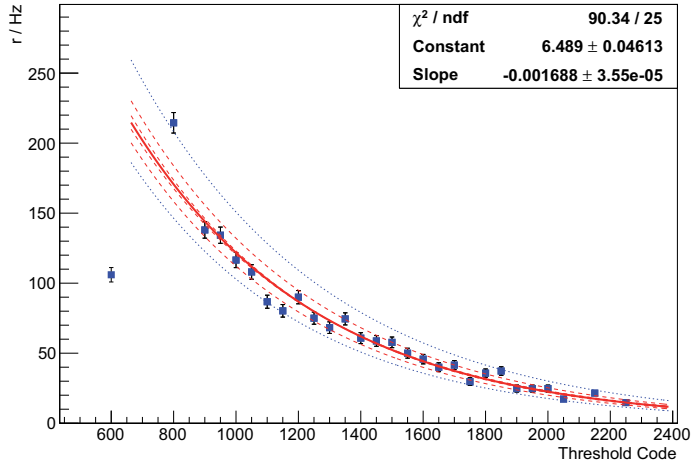
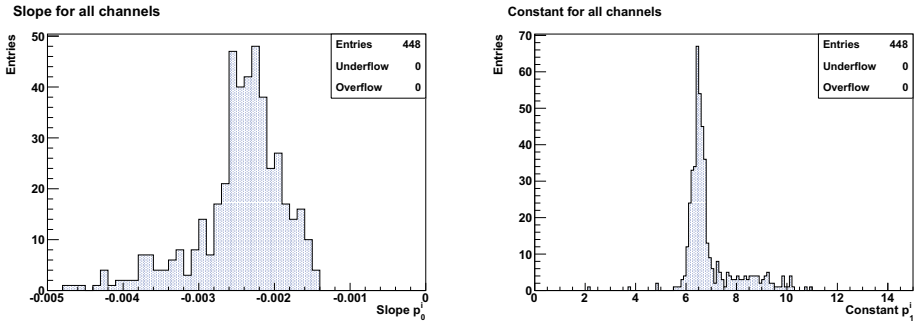


Figure 6.13: Measurement of the rate dependence $r_{11}(x)$ on the threshold for channel 11 of Setup 7. The first data point was excluded from the fit, since the expected value is larger than 250 Hz. The given uncertainties on the data points are calculated from counting errors as \sqrt{N} . The error band is represented by the red dashed exponentials with parameters $\rho_0^{11} \pm \Delta\rho_0^{11}$ and $\rho_1^{11} \pm \Delta\rho_1^{11}$ in all four possible combinations. The blue dotted lines represent the range of fluctuations as determined in two independent calibration runs.

<i>SD station, Setup</i>	<i>channels</i>
Corrientes, Setup 2	0*, 10*, 14*, 48*, 51*
Heisenberg, Setup 8	-
Kathy Turner, Setup 13	7, 13, 17, 25, 30, 31, 35, 37, 39, 41, 47, 48, 50, 60, 62, 63
Los Piojos, Setup 11	14, 15, 23, 34, 38, 48, 63
Phil Collins, Setup 7	11, 43
Toune, Setup 12	-
Yeka, Setup 19	-

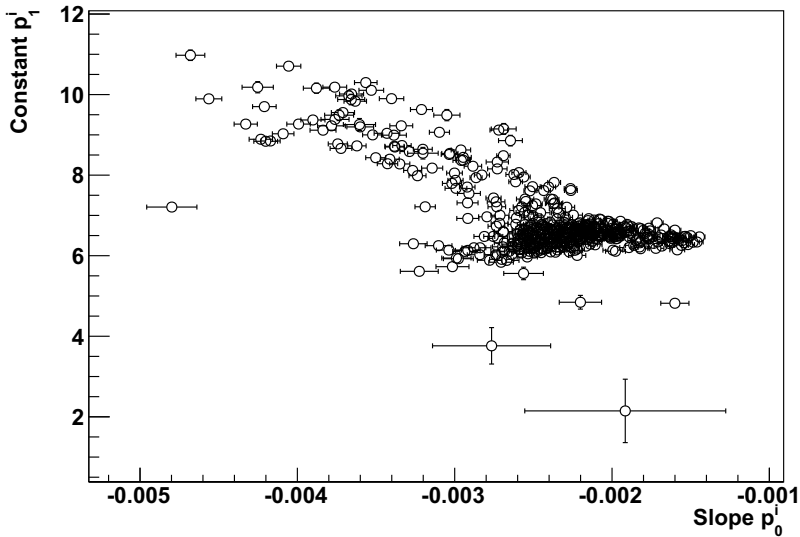
Table 6.3: Channels for which data points need to be ignored in the fit for the given reasons. Those channels marked with (*) have no fibres connected to the PMT. They can clearly be identified with the calibration procedure. All the channels listed here are ignored in the analysis in Section 6.6.



(a) Parameter Slope p_0^i .

(b) Parameter Constant p_1^i .

Slope vs. Constant for all channels



(c) Scatter plot for the two fit parameters.

Figure 6.14: Distribution of the fit parameters of $r_i(x)$ (Equation 5.9) for all channels and all MD modules of the PUC and the scatter plot for p_0^i and p_1^i .

Rate Dependence on Threshold Code for all Muon Detectors

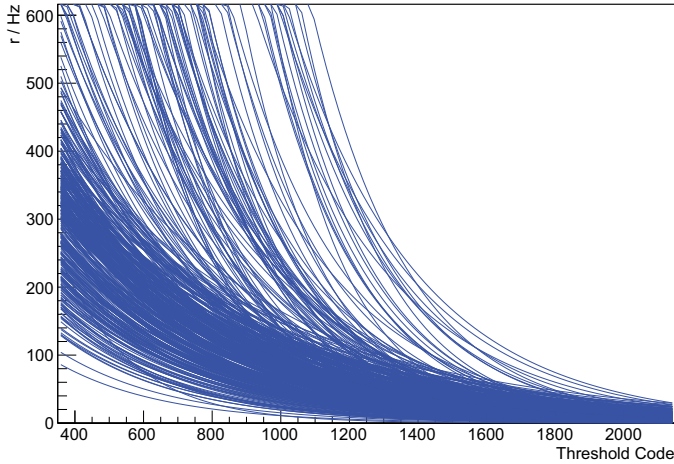


Figure 6.15: Distributions of the fit functions for all MD modules of the PUC. The plot excludes the five channels which have unconnected fibres at *Corrientes*.

To achieve a detector configuration in which the signal rate is the same for all channels, different thresholds have to be set. Figure 6.15 shows the fit functions for all MDs of the PUC as determined through the calibration procedure. Included are also the channels which are listed in Table 6.3 except for the channels of *Corrientes*. Pathological data points were removed for the fits. A wide spread of the functions can be observed. In Figure 6.16, distributions of the threshold code are shown exemplarily for four different rates. It may happen, that negative values for the threshold codes are computed. This would result in the minimal adjustable threshold for the channel and thus in a noisy behaviour. To avoid this, a threshold code of 4095 is set instead. This means disabling the channel for the measurement.

Since the MDs of the PUC are the first ones of their kind ever being operated, the obtained results can not be validated. Instead, they serve as a basis for the next detectors to be build. All detectors deliver data, hence, the entirety of results can be understood as parameter ranges in which fully functional detectors operate.

Stability of the Fit Parameters

The MD *Phil Collins* was chosen for a rerun of the calibration procedure. The calibration measurement of the 29th of February 2012 in the afternoon was repeated on the 30th August 2012 in the morning hours, which means that the calibration was performed once in the winter and once in the summer season. Figure 6.17 shows the differences of the fit parameters Slope $p_{0,Aug}^i - p_{0,Feb}^i$ and Constant $p_{1,Aug}^i - p_{1,Feb}^i$ (Equation 5.9) for the individual channels. A Gaussian, was fitted to each distribution to obtain the range of the fluctuations for both parameters. The distributions of the differences are

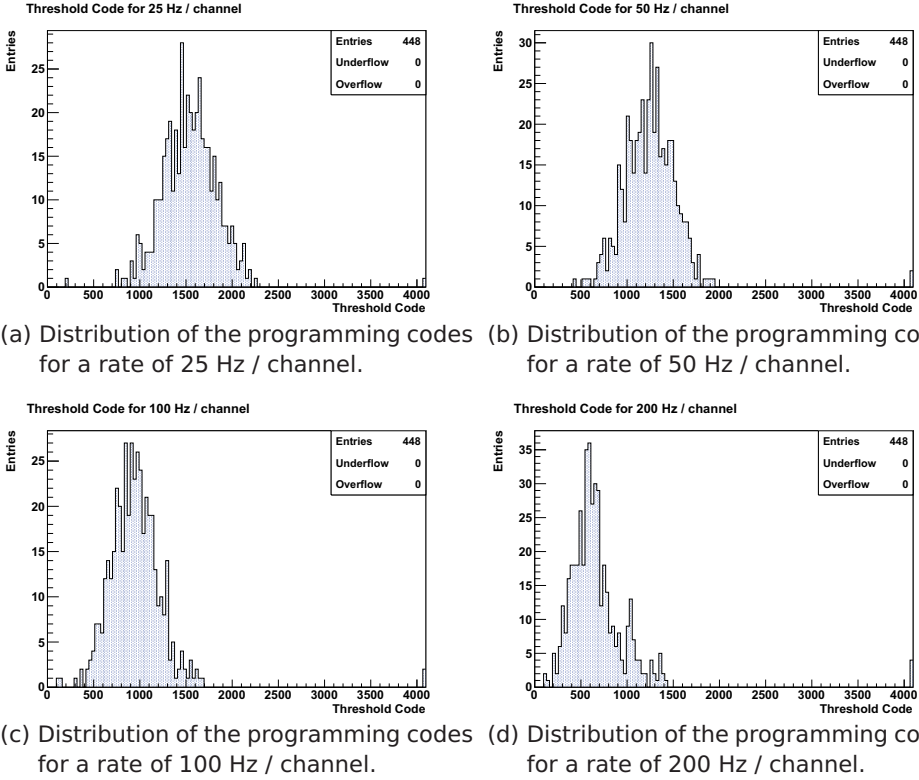
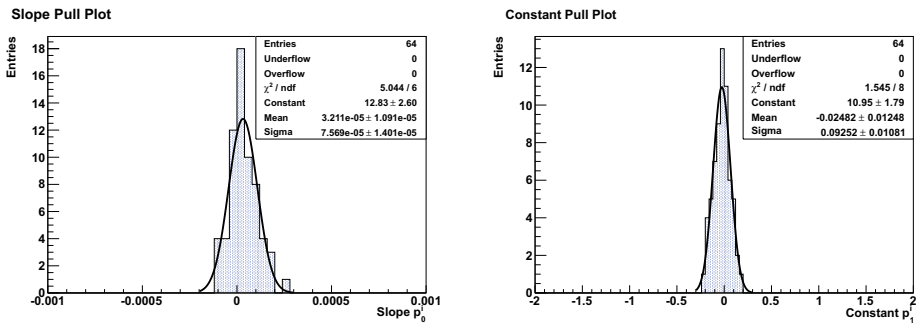


Figure 6.16: Distribution of the programming values x to achieve the same signal rate per channel for all detectors. For calculations, that would result in negative codes, the threshold code is set to 4095.

expected to have a mean value of zero. The mean values of the fits are compatible with that within three standard deviations. The widths of these Gaussians are added to the corresponding parameters p_0^{11} and p_1^{11} in Figure 6.13 to display the band of fluctuations. The resulting widths are

$$\sigma_{\text{slope}} = (7.6 \pm 1.4) \times 10^{-5} \quad \text{and} \quad \sigma_{\text{Constant}} = 0.09 \pm 0.01 . \quad (6.8)$$

The temperature measurements for the days of calibration runs can be obtained from the monitoring website of the Pierre Auger Observatory [Rau12]. The temperatures, measured near the PMTs of the SD station *Phil Collins*, range between $T = 18^\circ\text{C}$ and 24°C in February and between $T = 6^\circ\text{C}$ and 19°C in August 2012. For the times of the calibration runs, the monitoring system of the Pierre Auger Observatory shows $T \approx 20^\circ\text{C}$ for February and $T \approx 6^\circ\text{C}$ for August, respectively. A possible influence from the different temperatures on the rate curves is included in the observed fluctuations of the parameters. If future analysis shows the necessity, the dependence on the temperature needs to be studied in more detail.



(a) Differences for the parameter Slope $p_{0,Aug}^i - p_{0,Feb}^i$ (b) Difference for the parameter Constant $p_{1,Aug}^i - p_{1,Feb}^i$

Figure 6.17: Distribution of the differences in the fit parameters of $r_i(x)$ for data of the two calibration runs for the MD module at *Phil Collins* in February 2012 and in August 2012. A Gaussian was fitted to each distribution.

6.5 Temperature Dependence of the High Voltage

In June 2012, a dedicated monitoring run was performed with the MD readout electronics Setup 8 at the SD station *Heisenberg*. Temperature values from the two temperature sensors and the outputs of the HV monitoring circuits were recorded for several days. The results are shown in Figures 6.18 and 6.19.

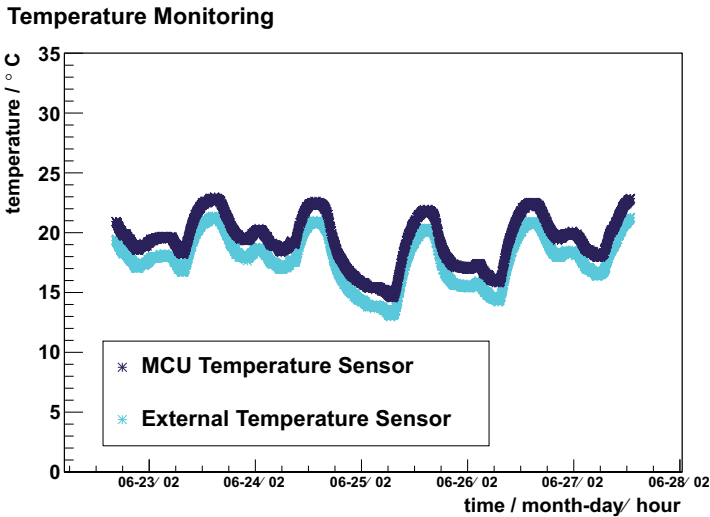


Figure 6.18: Monitoring values for the temperature sensors of the electronics Setup 8, deployed at *Heisenberg*. The data was taken in a dedicated monitoring run from the 24th of June to the 27th of June in 2012. Temperature variations from day to night are visible.

While the temperature curves range between 12°C and 25°C (Figure 6.18), the HV does not show any reaction to these variations (Figure 6.19). There is also no structure in the data in smaller time periods. However, a constant variation of the monitoring voltage of $\Delta U_{HV,mon} = 0.1\text{V}$ around the nominal value of 1V could be observed. The voltage U_{HV} can be converted to the HV value by multiplication with a factor of 1000 (Section 5.10).

The test was also performed at a constant temperature of 23°C with the electronics readout Setup 15 in a laboratory without a PMT being connected. The same variations of 0.1V around the nominal value can be observed for the monitoring voltage (Figures 6.20(a) and 6.20(b)). Thus, it can be concluded that the variation of $\Delta U_{HV,mon} = 0.1\text{V}$ is an unavoidable effect of the electronics itself. It could originate from the HV module itself, from the monitoring part or from a combination of both. This variation by 1% was not found to be critical with respect to the start of data taking. Therefore, a more detailed investigation was not performed in the context of this thesis.

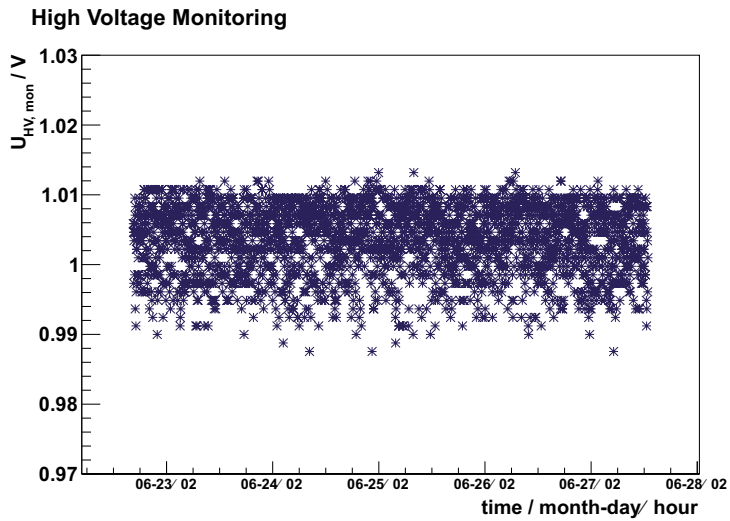
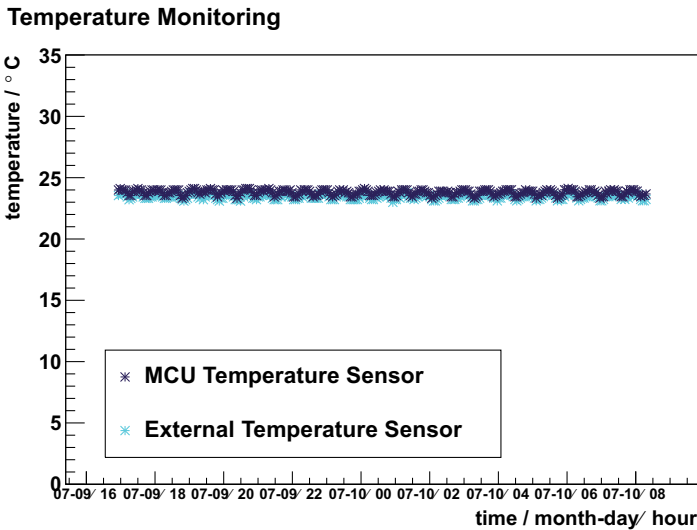
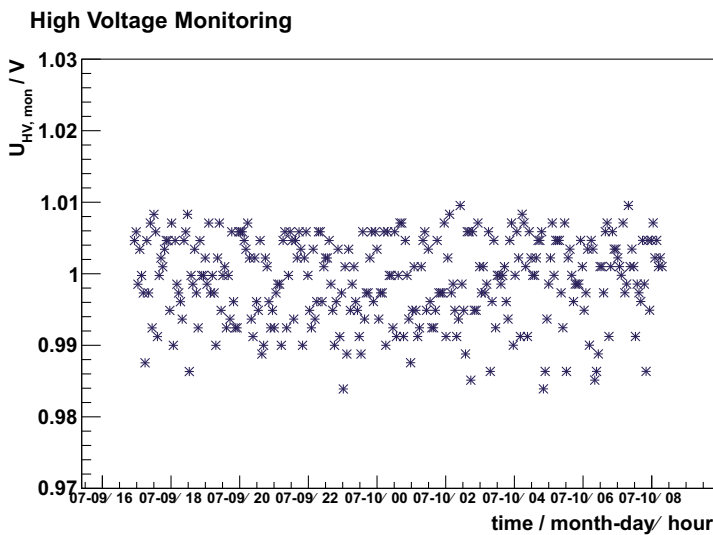


Figure 6.19: Values of the HV monitoring voltage $U_{HV, mon} = U_{HV}/1000$ recorded with the electronics Setup 8, deployed at *Heisenberg*. The data taking was performed in a dedicated monitoring run from the 24th of June to the 27th of June in 2012. No dependence on the temperature variations (Figure 6.18) can be observed. A spread by $\Delta U_{HV, mon} = 0.1$ V around the nominal value of 1 V was detected.



(a) Temperature monitoring in a laboratory measurement.



(b) HV monitoring in a laboratory measurement.

Figure 6.20: Monitoring temperature and HV monitoring voltage $U_{HV,mon} = U_{HV}/1000$ in a laboratory measurement with the electronics Setup 15 at a constant temperature of 23 °C. The data was taken in a dedicated monitoring run in from the 9th of July to the 12th of July in 2012. The temperature varies only due to the air conditioning cycles. A spread by $\Delta U_{HV,mon} = 0.1 V$ around the nominal value of 1 V of $U_{HV,mon}$ can also be observed here.

6.6 Combined Analysis of SD and MD Data

6.6.1 Datasets and Event Selection for the SD

Reconstructed SD data recorded with the detectors of the infill array from the 19th of June to the 15th of October 2012 were selected from the advanced data summary tree (ADST) files [Mar06] provided by [Dem12].

In a first step, quality cuts on the reconstructed SD data were applied. The reconstruction needs to result in a successful determination of the LDF (Section 3.3). Only those events for which the shower axis was reconstructed with a zenith angle between 0° and 60° and for which at least the T5 trigger condition was fulfilled (Section 3.5) are taken into account for the following analysis.

In a second step, it is assured that events for the analysis contain at least one SD station of the PUC, which are *Corrientes* (station ID 93), *Heisenberg* (1773), *Kathy Turner* (1764), *Los Piojos* (1574), *Toune* (688), *Phil Collins* (1622) and *Yeka* (1570).

The MD events as well as the SD data both include the GPS time (Global Positioning System) of recording. In the analysis, a muon event is identified to be related to an SD event if it was recorded in the same GPS second. In future, the analysis can be refined by comparing also the fraction of the GPS second, i.e. the GPS nanosecond, in which the events were recorded. Meanwhile, this information has been added to the muon data. It was technically not available for the data used in this thesis.

6.6.2 Reconstructed Energy and Arrival Direction of the SD Events

In Figure 6.21 the distribution of the reconstructed energies for the primary particles of the extensive air showers (EASs) as determined from the selected SD data is shown.

Since the PUC is part of the infill array of the SD, the full trigger efficiency of the SD is reached for EAS with primary energies around 10^{17} eV. The distribution of reconstructed energies should have its maximum in this region, which can be seen in the data. The decreasing amount of events for increasing primary energy is consistent with the measurements of a decreasing flux of cosmic ray particles with increasing energy (Section 2.2.1). This serves as a cross check of the integrity of the selected SD data and ensures that an unbiased sample is under study.

Looking at the angular distribution of the incoming directions of the detected EASs in Figure 6.22(a), the cut of $\theta < 60^\circ$ becomes visible besides the typical proportionality to $\sin\theta \cos\theta$. The latter is a result of the changing effective detector area and the decreasing flux with increasing zenith angle. Deformations and the position of the peak are caused by the detector layout and the efficiency of the trigger algorithms. The shape of the zenith angle distribution on the right-hand tail is due to the larger depth of atmosphere that inclined showers have to pass through compared to vertical ones with the same primary energy. Therefore, more interactions will take place and less particles will reach ground level. This might lead to a non-fulfillment of the trigger conditions of the SD and the shower will not be recorded as an event.

The azimuth angle (Figure 6.22(b)) however, remains untouched of these effects and covers its full range of values between 0 and 360° . The azimuth angle is expected to be independent on the signal strength in the MD and will be used as a counterexample

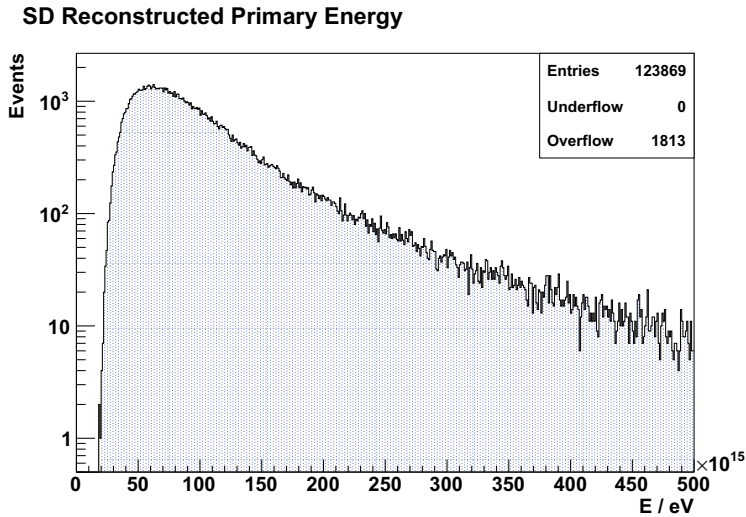


Figure 6.21: Reconstructed energies of the primary particles in the selected SD data.

to expected dependencies.

6.6.3 Reconstructed Signal Strength in the SD Stations

The following analysis requires an observable of the SD which is proportional to the signal strength in an individual SD station. Rather than directly comparing the measured signal strength S , the reconstructed LDF function is evaluated at the actual distance r of the MD module to the shower core. The value $S_{LDF}(r)$ is then compared with the observable N_{Trig} as measured with the MD module (Section 6.6.7). This uses the measurement with the detector array and thus effects of single detector properties, such as signal fluctuations, are reduced. Stations that were rejected in the SD reconstruction for any technical reason, in software or in hardware, but which should have recorded a signal, are thus recovered for the analysis. Stations that triggered accidentally (i.e. stations which were not triggered by shower particles) are already identified and excluded during the event reconstruction.

6.6.4 Data Taking Periods of the MD

The installation of the detectors of the PUC was finished in March 2012. In parallel, a monitoring tool was developed to check the availability of the SBCs via the wireless communication network every 30 minutes from April 2012 to October 2012. Figure 6.23 shows the availability of the SBCs which is the requirement for any measurement. In June 2012, the replacement of the existing wireless radio system by a new one, based on the Institute of Electrical and Electronics Engineers (IEEE) 802.11 standards, was installed and lead to an improved stability of the availabilities of the SBCs. From the time of the radio upgrade onwards, stable data acquisition with the MD became

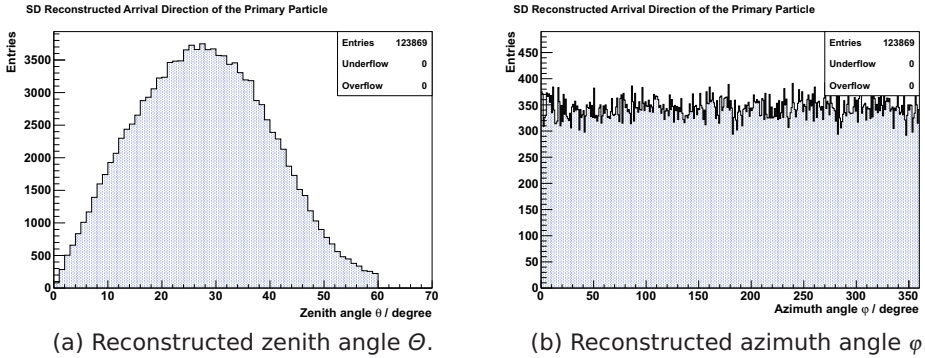


Figure 6.22: Reconstructed zenith angle Θ and reconstructed azimuth angle φ of the arrival directions of the incoming primary particles in the selected SD data. The cut of $\Theta < 60^\circ$ can be observed.

possible. data acquisition needs to be started explicitly. This start is not yet an automated process after a failure or a power cut.

The data acquisition runs of the PUC were also used to identify and fix problems in the software. Therefore, acquisition was stopped and relaunched from time to time, which resulted in e.g. inconstant event rates and files with test data which have to be excluded from the analysis. The parameters, that were varied in the different runs, are the thresholds for the comparators on the ABs. In a first run, a global threshold was set, whereas in the following runs, the thresholds were adjusted such that the same constant rate per channel was achieved for all modules. First results from the calibration procedure as described in Section 5.14 were used. Refined results, as discussed in Section 6.4, however, were not yet applied. In Table 6.4, all data taking runs, that were analysed in the context of this thesis, are listed.

As discussed in Section 5.14, the expected rate of background muons per scintillator strip is $r_{strip} \approx 27 \text{ s}^{-1}$. Therefore, the choice of the minimal rate ranges around at this value. The other settings were chosen arbitrarily to study the detector performance.

6.6.5 Analysis of the MD Data

The MD array in its final configuration (Section 4.2.1 and 4.4.1) is supposed to provide an additional exact measurement of the number of muons N_μ to a given EAS as recorded by the Pierre Auger Observatory. For the present analysis, the direct observable N_{Trig} for the signal strength in a MD module is chosen. N_{Trig} is defined as the number of timebins, in which the analogue input signals on the ABs were above threshold within a certain time window, i.e. the number of digital ones in a certain region in the event data. This variable does not require any prior interpretation of the data based on simulations such as N_μ does. At most, a dependency on the discrimination threshold for the amplified PMT signals is expected. Further, decreasing the width of a single time bin to 3.125 ns (Section 4.4.1), will have an effect on N_{Trig} which could not be studied yet with data from the experimental site. Data is recorded during

Muon Detector Availability

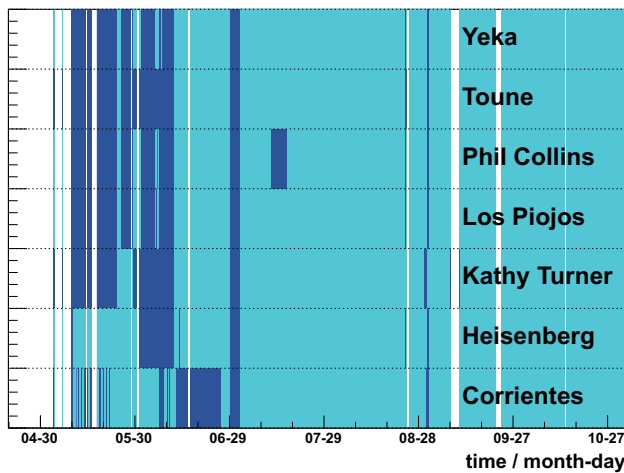


Figure 6.23: Availability of the SBCs of the MD modules of the PUC. The status of each SBC is checked every 30 minutes via the wireless communication system. Light blue areas indicate an available SBC, dark blue areas represent unavailable systems whereas white areas represent periods in which the monitoring system itself was not active. After the replacement of the radio hardware in June 2012, the availability became constant, which allows for stable conditions for measurements.

<i>start (UTC time)</i>	<i>end (UTC time)</i>	<i>comment</i>
2012-06-19 21:17:00	2012-07-05 05:14:59	200 mV global threshold
2012-07-05 05:15:00	2012-07-19 11:16:37	50 Hz / strip
2012-07-19 11:22:16	2012-08-09 07:23:40	100 Hz / strip
2012-08-09 07:43:55	2012-08-30 08:55:36	25 Hz / strip
2012-08-30 08:55:37	2012-09-05 20:16:59	test of firmware [s4] and communication maintenance (+)
2012-09-05 21:17:00	2012-10-15 23:59:59	300 Hz / strip
2012-09-22 00:00:00	2012-10-02 18:45:00	300 Hz / strip (*)
2012-10-02 18:45:01	2012-10-05 22:06:00	300 Hz / strip (**)
2012-10-05 22:06:01	2012-10-16 00:00:00	300 Hz / strip (***)

Table 6.4: Data taking periods for the MD modules of the PUC which are analysed in the context of this thesis. Data recorded with firmware [s4] is excluded from the analysis. Major maintenance work, that influenced the number of recorded events, was done in the last three periods are marked with asterisks.

the different stages of installation of the PUC and while the development of software is still ongoing. As a result, the MD modules of the PUC have different operational availabilities. Looking at the data on the level of the single MD modules, however, is not affected by these restrictions.

6.6.6 Event Layout of the MD Data

One event of a single detector of the MD consists of the information of all 64 PMT channels provided in 768 time bins. Depending on the firmware [s3, s4] of the FPGA, one time bin represents 12.5 ns or 3.125 ns. Data is permanently written into a ring buffer with a length of 256 time bins. A trigger signal to the electronics ends the writing process into this ring buffer and continues the writing process in a serial buffer with a width of 512 time bins. Therefore, time bin 255 represents the arrival time of the trigger. Information before and after the arrival time of the trigger are provided. The time structure of the MD events was chosen similar to the time structure of the SD events.

A shower front of an EAS will pass the SD station first, then penetrate the soil and, with some delay due to the time of flight of the shower particles, generate a signal in the associated MD module. Assuming the shower front to move at the speed of light and a distance of 10 m between SD station and MD module, the time of flight between the two detectors can be estimated to range at 30 ns. If the signal in the SD station fulfills the conditions for a T1 trigger, the trigger is formed in the SD electronics and given to the underground readout electronics of the MD module. The trigger forming process takes time in the order of μs . Therefore, physically relevant data of the shower front are expected to be recorded in the first third of a muon event and hence in the time bins 0 to 255.

The two delays, which are the time of flight and the time for trigger generation and

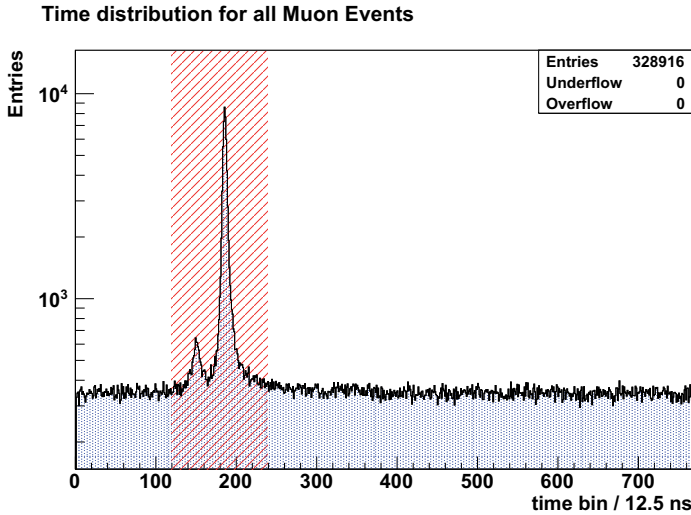


Figure 6.24: Time distribution of the signals in all events recorded with the MD modules in the given data taking periods. The red dashed area between time bin 120 and time bin 239 defines the trigger region. The observable N_{trig} , i.e. the number of logic 1s in this trigger region, is compared with the calculated signal strength in the reconstructed SD data. The double-peak structure in the shown distribution is due to the two different classes of T1 trigger, the T1-ToT (first peak) and the T1-TH (second peak).

processing, are reflected in the number of bins between the signals and the time bin 256. This number of bins is expected to be a detector-specific constant.

6.6.7 Definition of N_{Trig}

In Figure 6.24, an overlay of the time distribution of all recorded events is shown. The events were recorded with all MD modules of the PUC during the data taking periods mentioned in Table 6.4. A region around the signal peak is defined as trigger region. It includes data in the time bins between 120 and 239, corresponding to approximately $1.5 \mu\text{s}$ of recording time. N_{Trig} is defined as the number of timebins, in which the analogue input signals on the ABs were above threshold within a certain time window. Thus, N_{Trig} is the number of digital ones in this region. It can range between 0 and a maximum of $119 \times 64 = 7616$ in case that all 64 channels measured signals in all time bins.

A double-peak structure can be seen, which can be referred to the two kinds of T1 trigger of the SD. It can thus only occur in the DAQ mode synchronous with the SD array and not in the self-triggered occupancy trigger mode.

The first peak is due to events that fulfill the T1-ToT trigger conditions of the SD station. Its maximum is located in time bin $t_1 = (149 \pm 1) \times 12.5 \text{ ns}$ in the muon data for all MD modules of the PUC except for *Corrientes*, which shows a larger delay

for the peak. The second peak is due to the T1-TH trigger. It is found in the time bin $t_2 = (186 \pm 1) \times 12.5$ ns in the muon data. The generation of a T1-ToT trigger in the electronics of the SD station takes longer than the generation of a T1-TH trigger (Section 3.5.1). Information originating from particles in EAS thus reside longer in the buffers of the readout electronics of a MD modules with respect to the arrival time of the trigger.

Simulations predict this double-peak structure [San12] and can henceforth be confirmed with data. The distance in the peaks in simulations ranges around $t_{pp}^{sim} = 400$ ns, where $t_{pp} = (37 \pm 1) \times 12.5$ ns $\approx (460 \pm 12.5)$ ns is derived from the data.

From the position of the second peak in the data, the time that passed from the generation of a trigger signal in SD electronics to the time of the recording of an event in the FPGA of the MD underground electronics is determined to be $\Delta t = (255 - 186) \times 12.5$ ns ≈ 860 ns.

At *Corrientes*, the maxima of the peaks lie at $t_1 = (145 \pm 1) \times 12.5$ ns and $t_2 = (181 \pm 1) \times 12.5$ ns, corresponding to $\Delta t_{Corrientes} \approx 925$ ns. It is the only prototype detector, that has two detector modules installed, which is assumed to be the origin of the additional delay.

6.6.8 Combination of Data

The number of successfully reconstructed SD events per six hour in the selected dataset is shown in Figure 6.25. The number of events varies around 80 events per six hours. No events could be recorded or reconstructed around the 21st of June, the 15th of July, the 12th of August and the 9th of September 2012.

Additionally, the number of transmitted events by the MD to the Central Data Acquisition System (CDAS) is shown in Figure 6.25. The periodical peaks, e.g. between the 9th and the 28th of July 2012, originate from the operational time of the fluorescence detector (FD). If an EAS is detected by the SD and by the FD, both detectors generate trigger signals on T3 level and two event requests are sent by the CDAS to the SD array and respectively to the MD modules. One event measured by the MD may thus be stored twice in the raw data.

Figure 6.26 focuses on July 2012. The number of transmitted MD events and the uptime of the FD stations *Coihueco* and *HEAT* are shown. The uptime is defined as the time in which a telescope was in DAQ mode and thus as the time in which it was capable of generating T3 trigger requests. The widths of the peaks in the MD data as well as the widths of the uptime bars in Figure 6.26 shows a maximum around the 19th of July. This is due to the new moon in this night, which allows the longest DAQ time of the FD data taking period in July 2012.

The different data taking periods (Table 6.4) for the MD periods of maintenance work on the MD software are illustrated in the gray bar at the top of Figure 6.25.

Maintenance work on the data acquisition software of the MD modules requires to exclude data recorded on the 29th of September, the 24th and the 25th of August. No events of the MD were stored between the 12th and the 21st of August (Figure 6.25) because of a software failure. Data recorded in the beginning of September (data taking period marked with “+” in Figure 6.25) were excluded from the analysis since the firmware [s4] was installed and under test and additionally, maintenance work on

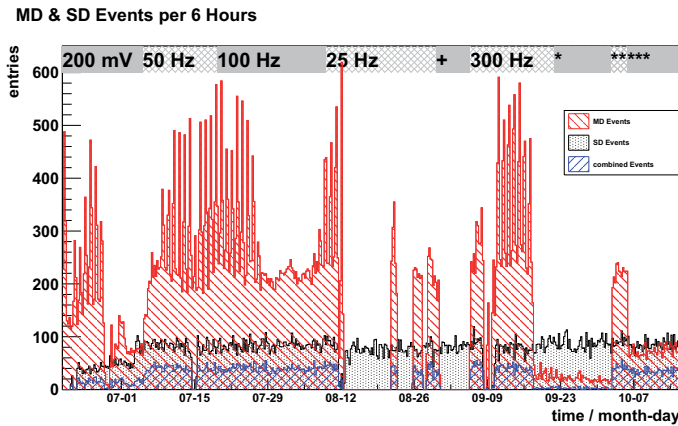


Figure 6.25: Number of recorded events per six hours for the SD (black dotted area) and for the MD (red hatched area, see legend). Events that were recorded in the same GPS second are drawn as combined events (blue hatched area, see legend). Data taking periods and periods of maintenance work are given in the gray bar at the top. The different features in the MD data are explained in the text. The number of transmitted muon events is expected to outnumber the number of reconstructed SD events, which cannot be observed. The rates are very similar to each other after the last software maintenance, which is marked with three asterisks.

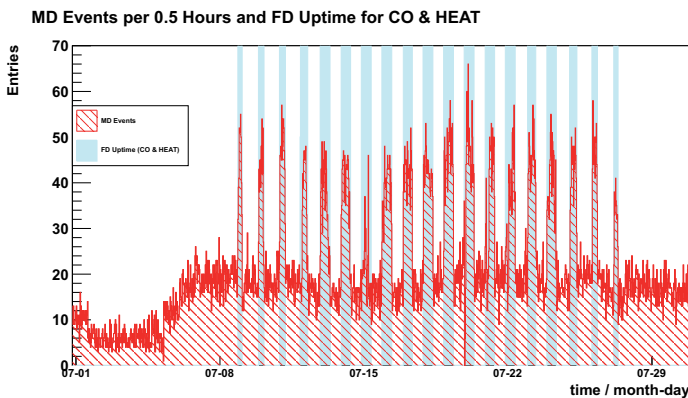


Figure 6.26: Number of recorded events per 30 minutes for the MD and uptime of the FD telescopes *Coihueco* and HEAT during July 2012. The uptime is put in arbitrary units different from zero if at least one of the telescopes was in DAQ mode.

the communication system was performed between the 30th of August 2012 and the 5th of September 2012.

The raw data rate is expected to be identical for the two detector arrays of MD and SD. However, this can not be observed even in the latest data taking period marked with asterisks. Since in this analysis raw muon data are compared with SD data after reconstruction, the amount of MD events is expected to outnumber the amount of reconstructed SD events in Figure 6.25. Instead, the rates are comparable after the last software update. This situation is currently under investigation. However, the amount of events that are recorded with both the MD and the SD ranges around a constant level of approximately 40 per six hours after the 5th of June, independent of software changes.

No dependence of the event rates on the configurations of the threshold levels on the ABs is observed. This is expected, since these are internal settings of the MD modules whereas the trigger is generated by the external SD station.

In total, 35,189 events could be reconstructed with the SD in the given time period. The MD transmitted 77,753 events to the CDAS. From these datasets, 11,144 pairs were identified, which were recorded in the same GPS second. For each of these events the participating MD modules are identified. The observable N_{trig} is then extracted for each module. The signal strength $S_{LDF}(r)$ at the position of the associated SD station is calculated using the LDF, which was determined in the reconstruction procedure. This way, 20,730 pairs of observables were extracted.

An example event (SD ID 20061843), recorded on the 7th of September 2012 at 12:28:07 UTC, from the combined dataset is shown in Figures 6.27 and 6.28. The first figure shows the infill array in black open circles. Filled coloured circles describe the SD stations which took part in the event. The size of the circles therein represents the strength of the measured signals, the colour code describes the time of trigger (T2) of the individual station going from yellow (early) to red (late). Filled dark gray circles represent off-grid stations, which triggered on T2 level but which are not included in the regular SD event reconstruction. The line shows the reconstructed shower axis. It ends at the calculated impact point on ground. The axes are scaled in site coordinates with the origin within the SD array.

A primary energy of $E = (6.26 \pm 0.35) \times 10^{17}$ eV and an arrival direction with zenith angle $\Theta = (18.7 \pm 0.4)^\circ$ and azimuth angle $\varphi = (352.1 \pm 1.3)^\circ$ were reconstructed for this event. The impact point of the shower axis on ground at $x = (-26.77 \pm 0.03)$ km and $y = (15.86 \pm 0.02)$ km in site coordinates lies within the triangle of the three SD stations with the strongest signals, as it is expected.

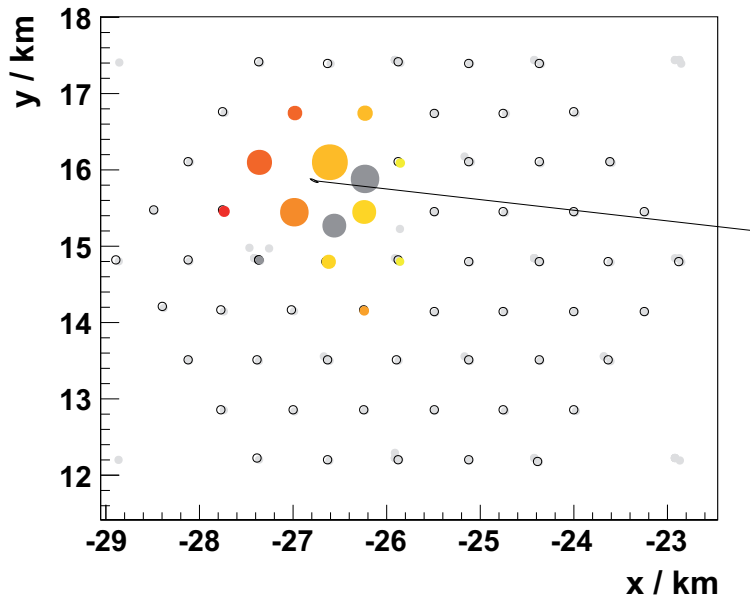


Figure 6.27: The SD part of an example event recorded simultaneously with the SD and the MD. Stations of the infill array are plotted as black open circles. Filled coloured circles represent the measured signal strength by their size and the time of trigger (T2) by their colour going from yellow (early) to red (late). Off-grid stations, which are ignored in the SD event reconstruction but which triggered on T2 level, are drawn as filled gray circles. The line shows the reconstructed shower axis and ends at the calculated impact point on ground.

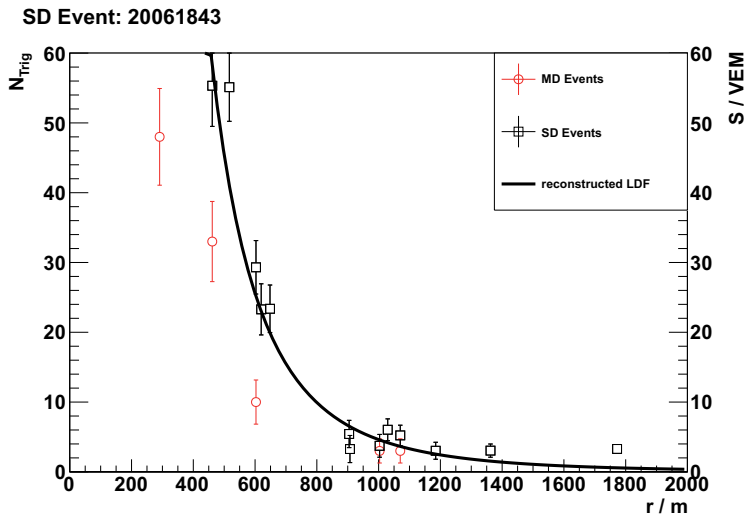


Figure 6.28: An example event recorded simultaneously with the SD and the MD. Shown are the signal strengths N_{Trig} for the MD modules (red open circles, left-hand scale) and $S_{LDF}(r)$ for the SD stations (black open squares, right-hand scale) taking part. The signal strengths are plotted against the distance r of the detectors to the reconstructed shower axis. An LDF following Equations 3.1 and 3.2 was fitted to the SD data.

The second figure shows the measured signal strengths N_{Trig} and $S_{LDF}(r)$ of MD modules and SD stations plotted against the distance r of the detectors to the reconstructed shower axis. An LDF following Equations 3.1 and 3.2 was fitted to the SD data. The fit parameters were determined as $S_{450} = (62.9 \pm 3.5(\pm 0.3)_{sys})$ VEM and $\beta = -2.19(\pm 0.15)_{sys}$ while $\gamma = 0$ was kept a constant.

Qualitatively, a decrease of the signal strength of the muon signal N_{Trig} with distance r can be observed. This event was chosen as an example from the combined dataset since all seven SD stations of the PUC show signals for the SD part (Figure 6.27) and five MD modules (*Heisenberg*, *Los Piojos*, *Phil Collins*, *Toune* and *Yeka*) show a non-zero signal and therefore were available and in DAQ mode (Figure 6.28). The missing two modules shall be mentioned briefly. The MD module of the SD station *Kathy Turner* had already been disassembled at the time of the measurement to test a different electronics readout system. Although the SD station *Corrientes* was found to be part of the event as an off grid detector (bottom dark gray circle in Figure 6.27), muon data should be available for the corresponding MD module. Albeit, due to a known technical limitation in the memory depth of the readout electronics of this MD module, the module is permanently configured to accept only 10 % of all external triggers and may thus have missed the event.

The following study investigates possible correlations between the signal strengths in the MD modules and their associated SD stations by determining an estimator for the correlation coefficient between the two observables.

Following e.g. [Cow98], the estimator r for the correlation coefficient ρ of two sets of variables x_i and y_i , with $i = 1, \dots, n$, is defined as

$$r = \frac{\sum_{i=1}^n (x_i - \bar{x})(y_i - \bar{y})}{\left(\sum_{j=1}^n (x_j - \bar{x}) \cdot \sum_{k=1}^n (y_k - \bar{y})\right)^{1/2}}, \quad (6.9)$$

where \bar{x} and \bar{y} are the sample means for the sets of x_i and y_i and n denotes the number of measurements. The definition of r implies $r \in [-1, 1]$. The uncertainty σ_r for r was chosen to be proportional to the square root of the inverse of n in the dataset

$$\sigma_r = \frac{1}{\sqrt{n}}. \quad (6.10)$$

The weighted mean $\langle r \rangle$ of a set of estimates r is calculated following Equation 6.11:

$$\langle r \rangle = \frac{1}{\mathcal{N}} \sum_t \frac{r_t}{(\sigma_r)_t^2}, \quad \text{with } \mathcal{N} = \sum_t \frac{1}{(\sigma_r)_t^2}, \quad (6.11)$$

where t loops over all estimates r of the set and \mathcal{N} denotes the normalisation.

The uncertainty $\sigma_{\langle r \rangle}$ on the weighted mean $\langle r \rangle$ is calculated such that $p = 68.27\%$ in a subset. Therein, p is defined following Equation 6.12:

$$p = \frac{1}{\mathcal{N}} \sum_j \frac{1}{\sigma_r^2} = \frac{1}{\mathcal{N}} \sum_j n_j, \quad (6.12)$$

where \mathcal{N} again is the normalisation but j loops over all determined estimates r of a the set for which $r \in [\langle r \rangle - \sigma_{\langle r \rangle}, \langle r \rangle + \sigma_{\langle r \rangle}]$ holds.

The quantity r is calculated for the observables $(x, y) = (N_{Trig}, \varphi)$ and $(x, y) = (N_{Trig}, S_{LDF}(r))$ with the full dataset divided in sub-sets of six hours each. The different measurement periods are treated separately.

The azimuth angle φ is expected to be independent of the signal strength N_{Trig} measured with a MD module and serves as a cross check for the analysis of the observables $(N_{Trig}, S_{LDF}(r))$.

The scatter plot for all pairs (N_{Trig}, φ) is shown in Figure 6.29. The range of possible values of the azimuth angle φ between 0 and 360° is isotropically covered. The uncertainties for φ are determined in the reconstruction procedure, the uncertainties for N_{Trig} are defined as $\sigma_{N_{Trig}} = \sqrt{N_{Trig}}$.

The correlation estimator r for the observables (N_{Trig}, φ) against time is shown in Figure 6.30. The measurement periods are also shown in this figure. The weighted means of the distribution $\langle r_\varphi \rangle$ with their uncertainties $\sigma_{\langle r \rangle}$ for the different measurement periods are given in Table 6.5 and are drawn as solid and dashed lines and shaded areas in Figure 6.30.

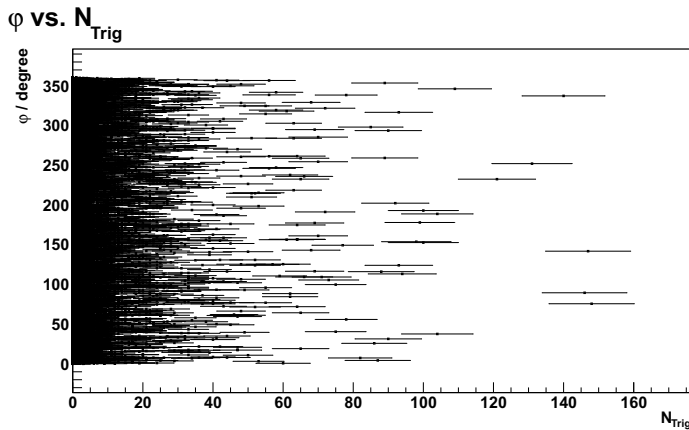


Figure 6.29: Scatter plot of the two observables N_{Trig} and φ . The azimuth angle φ covers all possible values between 0 and 2π isotropically.

The mean values $\langle r_\varphi \rangle$ as determined with the combined dataset are given in Equation 6.5. They are compatible with zero, which confirms the expectation, since N_{Trig} and φ constitute two independent variables.

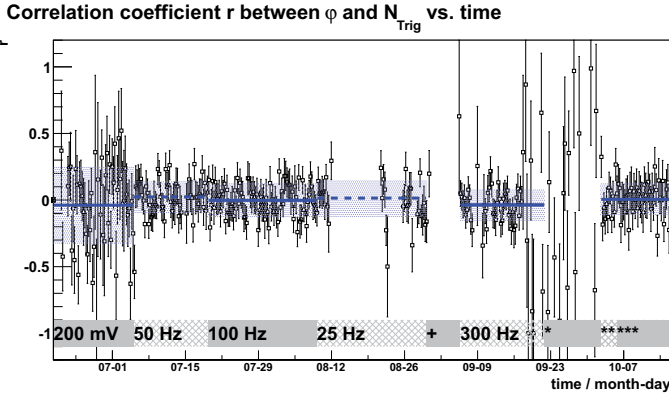


Figure 6.30: Correlation coefficient r_ϕ between ϕ and N_{Trig} in bins of six hours. Uncertainties are calculated as explained in the text. Different measurement and maintenance periods are shown. The weighted means are compatible with zero, which is in agreement with the expectation.

MD DAQ period	$\langle r_\phi \rangle$
200 mV	0.0 ± 0.3
50 Hz	0.0 ± 0.1
100 Hz	0.0 ± 0.1
25 Hz	0.0 ± 0.1
300 Hz	0.0 ± 0.1
300 Hz **/**	0.0 ± 0.1

Table 6.5: Mean correlation estimator $\langle r_\phi \rangle$ calculated as the mean of the estimators r_ϕ of data subsets of six hours. See Table 6.4 for the DAQ periods. The uncertainty bands include 68.27 % of the results in the defined period.

Figure 6.31 shows the scatter plot for all pairs $(N_{Trig}, S_{LDF}(r))$. The uncertainties on $S_{LDF}(r)$ are estimated using Equation 6.13:

$$\sigma_S = (0.32 + 0.42 \times \sec \Theta) \times \sqrt{S}. \tag{6.13}$$

The uncertainty σ_S is derived from measurements with pair tanks [Ave07]. Since it is the uncertainty on the signal S as measured in a an SD station, it is an over-estimation for the reconstructed LDF $S_{LDF}(r)$.

The correlation estimators r for the observables $(N_{Trig}, S_{LDF}(r))$ are shown versus the time in Figure 6.32. Also shown are again the measurement periods and the weighted means with their uncertainties. Table 6.6 lists the weighed means $\langle r_S \rangle$ with their uncertainties. For all measurement periods, the means are compatible with each other within the calculated uncertainties.

No dependence on the different settings in the MD modules is observable. The

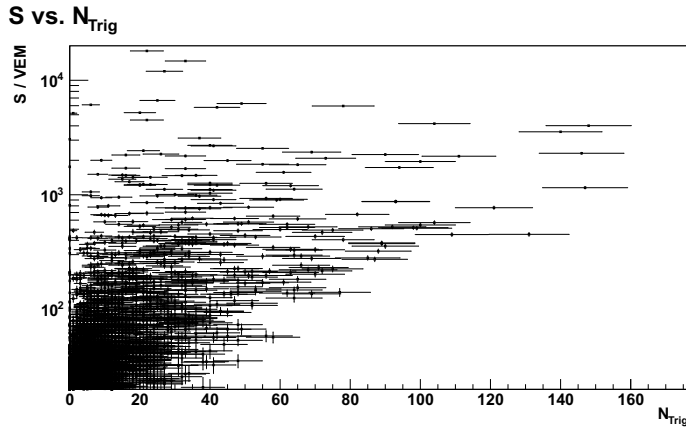


Figure 6.31: Scatter plot of the two observables N_{Trig} and $S_{LDF}(r)$.

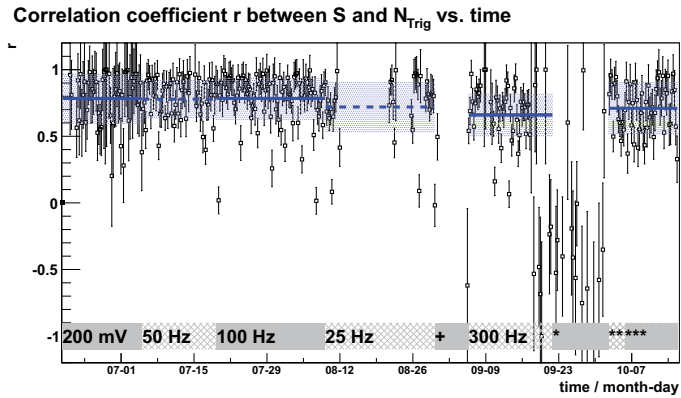


Figure 6.32: Correlation coefficient r_S between $S_{LDF}(r)$ and N_{Trig} in bins of six hours. Uncertainties are calculated as explained in the text. Different measurement and maintenance periods are shown.

MD DAQ period	$\langle r_S \rangle$
200 mV	0.8 ± 0.2
50 Hz	0.8 ± 0.1
100 Hz	0.8 ± 0.2
25 Hz	0.7 ± 0.2
300 Hz	0.7 ± 0.2
300 Hz**/**	0.7 ± 0.2

Table 6.6: Mean correlation estimator $\langle r_S \rangle$ calculated as the mean of the estimators r_S of data subsets of six hours. See Table 6.4 for the DAQ periods. The uncertainty bands include 68.27 % of the results in the defined period.

values for $\langle r_S \rangle$ are significantly different from the values for $\langle r_\phi \rangle$, which leads to the conclusion that N_{Trig} and $S_{LDF}(r)$ are not independent variables but correlate as expected.

The presented correlation between the data measured with the MD array and with the SD array is very encouraging for future studies. It could be shown, that the MD modules are sensitive to muons, and that they can be operated synchronously with the existing SD array.

Chapter 7

Conclusions and Outlook

The subject of this thesis was the successful commissioning of a muon detector prototype system for the AMIGA enhancement of the Pierre Auger Observatory.

To reach this aim, 26 readout electronics systems have been produced and tested in Siegen. From these, 19 systems were shipped to Argentina to be installed at the experimental site in Malargüe as part of the MD modules of AMIGA.

Besides the readout electronics systems, 20 pairs of auxiliary boards, which are necessary for the synchronisation of a MD module with the associated SD station, were produced and tested.

The system tests described in this thesis were developed such that they can be adapted for a possible mass production of the electronics to equip the full infill array with MD modules. A manual, describing the processing of all system tests, has been created for this purpose. The required amount of approximately 240 systems can be produced within 30 months at the presently possible production rate of two setups per week. An upgrade of the existing test facility, e.g. by setting up a second test stand (Section 5.1), decreases the total production time to a minimum of 15 months. However, the production rate of the electronics outnumbers the production rate of the scintillator modules. At least five years are required to produce all scintillator modules which are required to equip the full infill array using the existing facilities [Man12]. The production rate of the electronics at present includes the time for soldering and assembling as well as the time for tests. In a mass production scenario, the soldering part would be given to industry. Further, the time needed for the tests is mainly driven by the day-long threshold scan which could be shortened or even abandoned due to the calibration method as discussed in this thesis (Section 5.14).

In parallel to the testing of the readout systems and to prepare the combined analysis, discussed in this thesis (Section 6.6), a complete prototype setup, consisting of scintillator, PMT and the electronics has been set up in the laboratory. With this, the sensitivity of the MD modules to muons, that pass the scintillator, was shown. The scintillator of this prototype consists of 16 strips of approximately 1 m length. The 16 PMT pixels to which the wavelength shifting (WLS) fibres, which connect the scintillator strips and the PMT, were identified. For this purpose, a radioactive source was moved over the scintillating strips and the recorded signals of the AMIGA system were evaluated. A hodoscope system was set up with the prototype. Coincident signals

from the hodoscope were used as an external trigger to the AMIGA readout electronics, and thus mimicked the trigger by an SD station in the experimental configuration at Malargüe. As one result of the laboratory prototype setup, a clear correlation between the position of the hodoscope on the scintillator module and the activity of the strips below this hodoscope was derived from the data [Tig11, Lau12].

Seven full AMIGA MD modules were successfully installed at the experimental site in Malargüe, they are equipped with the readout electronics developed and tested in Siegen and constitute the pre-unitary cell (PUC) as a first hexagon of the future MD array. The PUC has been used for the development and enhancement of software which is needed for the synchronisation of the new MD array with the existing SD array and is now taking data.

Besides this, a calibration method for the new detector was developed. Its results are currently the basis for all configurations for the DAQ processes of the MD modules. The data, that was recorded after the implementation of the trigger synchronisation could be combined with the data of the SD array and analysed (Section 6.6).

The advanced test on the expected correlation between signal strengths in the MD modules and the corresponding SD stations from data triggered by the CDAS, which is described in this thesis (Section 6.6), goes beyond the preceding laboratory test and checks the synchronisation of the detectors in situ and thus all software modules involved.

The analysis discussed in the present thesis proves the expected correlation between the signal strength N_{Trig} in the MD module and the signal strength $S_{LDF}(r)$ at the associated SD station. The correlation estimator $\langle r_S \rangle$ is significantly different to the correlation estimator $\langle r_\phi \rangle$ for the two independent observables N_{Trig} and azimuth angle ϕ of the incoming EAS. As an example, $\langle r_S \rangle^{100\text{Hz}} = 0.8 \pm 0.2$ was determined in a data taking run in which the signal rate per channel in the electronics was adjusted to 100 Hz. With these data, the value of $\langle r_\phi \rangle^{100\text{Hz}} = 0.0 \pm 0.1$ results for the two independent variables (Section 6.6.8, in particular Tables 6.6 and 6.5).

In a next step, and with more data recorded with the MD modules, a correlation between the composition sensitive observable X_{\max} of the FD with the observable N_{Trig} defined here could be studied. So far, too few data were collected to give statistically significant results.

Besides, the correlation estimator presented here is not sensitive to the internal settings of the threshold levels in the MD modules. This should be studied again if the FPGA firmware is changed to [s4] or a similar version which provides a higher resolution in time of the recorded signals.

The 320 MHz DAQ firmware [s4] can be used for data taking in the existing systems. This revised version is based on the 80 MHz DAQ firmware [s3], which is in operation since 2009 and which therefore is well understood. Communication with the SBC is well established and remained unchanged. The firmware [s4] has been finalised and tested in laboratory measurements in August 2012 and could be used for the configurations of the FPGAs at the experimental site now.

Future options to simplify the existing readout electronics system are the combination of the DB and the MCUB into one board and a possible combination of the ABs and the MB into a new board, which would then reduce the number of boards in one setup to three, given that the PDB remains separated. This would simplify the production and assembling process and at the same time reduce the susceptibility to errors

due to the smaller amount of cable-bound connections in the final setup. The auxiliary boards can be extended by minor changes to support up to four MD electronics systems.

A self-calibration of the MD modules implemented in the FPGA on the DB is a possible option to simplify future re-calibration processes. The idea is to permanently monitor the background rate of the individual channels and to adjust the thresholds on the ABs automatically according to a given target rate. This adjustment of the thresholds could be implemented to work in parallel to the DAQ or while the DAQ is temporarily halted. It is recommended to repeat the calibration process described in this thesis (Section 5.14) at regular intervals to study possible variations. It is further recommended to only use the calibration curves obtained from those datasets which were cleaned from pathological data points (Section 6.4).

In summary, it can be said, that during the time of this thesis, 26 electronics readout systems for the MD modules have been successfully produced and tested. Seven of them were finally installed and commissioned at the Pierre Auger Observatory in Malargüe, Argentina. System tests for the electronics in view of a future mass production have been developed.

The analysis of the first data taken with the installed detectors shows the expected correlation between the signal strengths in the MD modules and in the SD stations and thus serves as a proof of principle. Further analysis will aim at precisely determining the number of muons event by event from the measured signals in the MD array. Counting strategies, which need to be tested in detailed detector simulations, have to be used for that.

A possible correlation between the composition sensitive observable X_{\max} of the FD with N_{Trig} could be studied next.

Acronyms

AB	analogue board.....	51
ADC	analogue-to-digital converter.....	53
ADST	advanced data summary tree.....	113
AERA	Auger Engineering Radio Array.....	17
AGASA	Akeno Giant Air Shower Array.....	13
AGN	active galactic nucleus.....	35
AGNs	active galactic nuclei.....	19
AIROBICC	Airshower Observation By angle Integrating Cherenkov Counters.....	13
AMBER	Air-shower Microwave Bremsstrahlung Experimental Radiometer.....	30
AMIGA	Auger Muon and Infill for the Ground Array.....	85
AuxLS	auxiliary board LS.....	54
AuxSBC	auxiliary board SBC.....	95
BLANCA	Broad Lateral Non-imaging Cherenkov Array.....	13
CAN	controller area network.....	95
CASA	Chicago Air Shower Array.....	13
CDAS	Central Data Acquisition System.....	119
CLF	Central Laser Facility	
CMB	cosmic microwave background.....	19
CODALEMA	Cosmic ray Detection Array with Logarithmic Electro-Magnetic Antennas.....	15
CPLD	complex programmable logic device.....	54
CRS	central radio station.....	28
DAC	digital-to-analogue converter.....	52
DAQ	data acquisition.....	94
DB	digital board.....	89
EAS	extensive air shower.....	113
EASIER	Extensive Air Shower Identification using Electron Radiometer30	

FAB	front-end analog board.....	26
FADC	flash analogue-to-digital converter	20
FD	fluorescence detector.....	119
FDWave	Fluorescence Detector Wave system	30
FEB	front end board	54
FLT	first level trigger.....	26
FM	frequency modulated	28
FPGA	field-programmable gate array.....	89
GPIB	general purpose interface bus	
GPS	Global Positioning System	45
GTS	GPS timestamp	78
GZK	Greisen-Zatsepin-Kuzmin	19
H.E.S.S.	High Energy Stereoscopic System	14
HE	head electronics	26
HEAT	High Elevation Auger Telescopes	17
HiRes	High Resolution Fly’s Eye	32
HV	high voltage.....	85
IEEE	Institute of Electrical and Electronics Engineers.....	114
ISA	industry standard architecture	54
JTAG	joint test action group	
KASCADE	Karlsruhe Shower Core and Array Detector	13
LDF	lateral density function	85
LED	light emitting diode	
LHC	Large Hadron Collider.....	43
LNA	low noise amplifier	28
LOFAR	Low Frequency Array	15
LOPES	LOFAR Prototype Station.....	15
LPM	Landau-Pomeranchuk-Migdal.....	11
LS	Local Station	97
LSB	least significant bit	
LTS	local timestamp.....	100
LVDS	Low voltage differential signal.....	51
MAGIC	Major Atmospheric Gamma-ray Imaging Cherenkov Telescopes 14	
MB	mother board	51
MCUB	microcontroller board	93
MD	muon detector.....	85

MIA	Michigan Muon Array	13
MibADC	multi buffered analogue-to-digital converter	92
MIDAS	Microwave Detection of Air Showers	30
MLDF	muon lateral density function	45
NKG	Nishimura, Kamata and Greisen	
OPERA	Oscillation Project with Emulsion-Tracking Apparatus	
PaB	pattern board	97
PDB	power distributor board	50
PMT	photo multiplier tube	85
PS	passive serial	52
PUC	pre-unitary cell	85
PVC	polyvinyl chloride	48
rbf	raw binary format	62
RDS	radio detection stations	27
RMS	root mean square deviation	34
SBC	single board computer	95
SCPI	standard commands for programmable instruments	
SD	surface detector	85
SLT	second level trigger	26
SM	Standard Model	5
SMA	SubMiniature version A	58
SPE	single photo-electron	48
SPI	serial peripheric interface	54
SUGAR	Sydney University Giant Air shower Recorder	13
TA	Telescope Array	14
TIB	test stand interface board	86
TLT	Third Level Trigger	26
ToT	time-over-threshold	28
TTL	transistor-transistor logic	52
UB	unified board	78
UC	unitary cell	47
UHECR	ultra-high-energy cosmic ray	19
USB	universal serial bus	
UTC	coordinated universal time	
VCV	Véron-Cetty and Véron 12 th	35
VEM	vertical equivalent muon	24

Acronyms

VERITAS	Very Energetic Radiation Imaging Telescope Array System	14
VR	Volcano Ranch	19
WLS	wavelength shifting	129

List of Figures

2.1	All-particle energy spectrum of cosmic rays as measured directly with several detectors.	6
2.2	Abundance of elements in primary cosmic rays as a function of their nuclear charge number Z	8
2.3	All-particle cosmic ray energy spectrum as obtained by direct and indirect measurements.	9
3.1	Status of the Pierre Auger Observatory near the city of Malargüe as of March 2009.	18
3.2	Image of the SD station <i>Voldemort</i> with explanatory labels applied. . . .	21
3.3	Schematic view of the optical system of the FD telescopes.	23
3.4	Trigger system hierarchy of the SD of the Pierre Auger Observatory. . . .	24
3.5	Event selection hierarchy of the SD of the Pierre Auger Observatory. . . .	24
3.6	Layout of the AERA enhancement at its different installation stages. . . .	27
3.7	The trigger efficiency for the 3ToT trigger for the infill and the regular array.	29
3.8	Example image of a low-energy event recorded in coincidence with HEAT and two <i>Coihueco</i> telescopes.	30
3.9	Combined energy spectrum as measured by the Pierre Auger Observatory between 2004 and 2008.	33
3.10	Measurement of $\langle X_{\max} \rangle$ and its <i>RMS</i> and representations of the predictions of air shower simulations based on different hadronic interaction models.	34
3.11	Search for point sources.	36
3.12	The degree of correlation ρ_{data} as a result of the point source research. . . .	37
3.13	Scatter plot of X_{\max} vs. $\log_{10}(S_b)$ for simulated showers of primary protons and photons.	38
3.14	Upper limits on the photon flux.	39
3.15	Neutrino observation at the Pierre Auger Observatory.	40
3.16	Upper limits on the flux of neutrinos.	41
4.1	Accessible energy ranges for KASCADE-Grande, the Pierre Auger Observatory, and the enhancements AMIGA and HEAT.	44
4.2	Distribution of $N_{\mu}(600)$ for proton and iron primaries for 30 m^2 MD modules.	46
4.3	The PUC inside the infill array of the SD.	47
4.4	Principle of particle detection in a scintillating strip.	48
4.5	During the installation of the first 5 m^2 MD module at <i>Corrientes</i>	49

4.6	A completely assembled setup of the underground readout electronics.	51
4.7	The two auxiliary boards AuxLS and AuxSBC.	55
5.1	Multiplexing scheme of the test stand setup.	59
5.2	Interconnection of the devices used in the test stand.	60
5.3	Channeltest evaluation for a fully operational setup.	65
5.4	Channeltest evaluation for a setup with typical failures.	66
5.5	Threshold scan for a single channel and one threshold voltage.	70
5.6	Linearity measurement for channel 2 of Setup 18.	71
5.7	Functional dependence between the programming value $code_{HV}$ for the DAC and the HV U_{HV} as directly measured.	73
5.8	Monitoring circuit for the 2.5 V voltage generated on the DB.	75
5.9	Schematics of the handling of an external trigger.	80
5.10	Trigger signals for the AMIGA electronics.	81
5.11	Signal rate $r_{41}(x)$ of channel 41 of the MD module at <i>Phil Collins</i> and exponential fit to the data.	83
5.12	Distribution of the fit functions for all 64 channels of the MD module at <i>Phil Collins</i> .	84
6.1	Various measurements of the internal resistance of the test stand.	86
6.2	Input circuit used for the tests that are to characterise the readout electronics.	87
6.3	Distribution of the minimal thresholds for which no electrical crosstalk could be observed yet.	88
6.4	Results of the threshold scans performed for channel 54 of Setup 11.	90
6.5	Results of the threshold scans: Distribution of the fit parameters of the linear fits for all setups under test and scatter plot for the fit parameters slope and offset.	91
6.6	Precision of the monitoring part for the digital voltages.	93
6.7	Precision of the monitoring part for the analogue voltages.	94
6.8	Interconnection of the devices used in the trigger test with the pattern board (PaB).	97
6.9	Interconnection of the devices used in the trigger test with the Local Station (LS).	99
6.10	Event request efficiency using the modified firmware for the FPGA on the LS.	99
6.11	Examples of events as displayed by the oscilloscope and as reconstructed in the analysis.	102
6.12	Position of the bit mismatches detected in the events that were recorded using the initial modification of the FPGA firmware for the LS electronics.	103
6.13	Measurement of the rate dependence $r_{11}(x)$ on the threshold for channel 11 of Setup 7.	105
6.14	Distribution of the fit parameters of $r_i(x)$ for all channels and scatter plot for p_0^i and p_1^i .	106
6.15	Distributions of the fit functions for all MD modules of the PUC.	107

6.16	Distribution of the programming values x to achieve the same signal rate per channel for all detectors.	108
6.17	Distribution of the differences in the fit parameters of $r_i(x)$ for data of the two calibration runs at <i>Phil Collins</i>	109
6.18	Monitoring values for the temperature sensors of the electronics Setup 8 at <i>Heisenberg</i>	110
6.19	Values of the HV monitoring voltage $U_{HV,mon} = U_{HV}/1000$ recorded with the electronics Setup 8 at <i>Heisenberg</i>	111
6.20	Monitoring temperature and HV monitoring voltage $U_{HV,mon} = U_{HV}/1000$ in a laboratory measurement with the electronics Setup 15. . .	112
6.21	Reconstructed energies of the primary particles in the selected SD data.	114
6.22	Reconstructed zenith angle Θ and reconstructed azimuth angle φ of the arrival directions of the incoming primary particles in the selected SD data.	115
6.23	Availability of the SBCs of the MD modules of the PUC.	116
6.24	Time distribution of the signals in all events recorded with the MD modules.	118
6.25	Number of recorded events per six hours for the SD and for the MD.	120
6.26	Number of recorded events per 30 minutes for the MD and uptimes of <i>Coihueco</i> and <i>HEAT</i>	120
6.27	The SD part of an example event.	122
6.28	Signal strengths in an example event recorded simultaneously with the SD and the MD.	123
6.29	Scatter plot of the two observables N_{Trig} and φ	125
6.30	Correlation coefficient r_φ between φ and N_{Trig} in bins of six hours.	126
6.31	Scatter plot of the two observables N_{Trig} and $S_{LDF}(r)$	127
6.32	Correlation coefficient r_S between $S_{LDF}(r)$ and N_{Trig} in bins of six hours.	127

List of Tables

5.1 Monitored voltages, the formulae to convert the digitised values A_{DIG} of the ADC to the corresponding voltages U_{mon} and the nominal values for A_{DIG}	76
6.1 Mean monitored voltages $\langle U_{mon} \rangle$ as determined in 15 single measurements with a digital multimeter.	92
6.2 Parameters of the HV characterisation determined for the single setups. .	95
6.3 Channels for which data points need to be ignored in the fit for the given reasons.	105
6.4 Data taking periods for the MD modules of the PUC.	117
6.5 Mean correlation estimator $\langle r_\phi \rangle$	126
6.6 Mean correlation estimator $\langle r_S \rangle$	128

Components and Devices

- [1] Agilent Technologies Inc.,
152A Active Probe.
- [2] Agilent Technologies Inc.,
1169A 12 GHz InfiniiMax II Series Probe Amplifier.
- [3] Agilent Technologies Inc.,
82357B USB/GPIB Interface High-Speed USB 2.0.
- [4] Agilent Technologies Inc.,
33250A Function / Arbitrary Waveform Generator, 80 MHz.
- [5] Agilent Technologies Inc.,
34941A Quad 1x4 50 Ohm 3 GHz Multiplexer Module for 34980A.
- [6] Agilent Technologies Inc.,
34980A Multifunction Switch/Measure Mainframe.
- [7] Agilent Technologies Inc.,
54845A Infinium Oscilloscope.
- [8] Altera Corporation,
CPLD: Altera MAX II, TMS570G100C5N.
- [9] Altera Corporation,
FPGA: Altera Cyclone III, EP3C25F324I7.
- [10] Analog Devices Inc.,
Voltage Output Temperature Sensor, AD22103.
- [11] Analog Devices Inc.,
Single 12-bit DAC, AD5620.
- [12] Auxiliary boards for the AMIGA MD electronics,
in cooperation with Almela, A., Kolotaev, Y., d. I. Vega, G. and Wainberg, O.,
Auxiliary Board LS and Auxiliary Board SBC.
- [13] Caddock Electronics, Inc.,
Ultra-Precision Voltage Divider: HVD5-A50M-050-05.

- [14] Fermilab,
*Scintillator material, Dow Styron 663W polystyrene ($[C_6H_5CHCH_2]_n$),
doped with 1 % PPO and 0.03 % POPOP, see [Aug06, Pla11].*
- [15] Hamamatsu Photonics K.K.,
Compact High Voltage Power Supply: C4900.
- [16] Hamamatsu Photonics K.K.,
Photomultiplier, H8804-200 MOD.
- [17] Microchip Technology Inc.,
2.5 V Voltage Reference, MCP1525.
- [18] LEMO S.A.,
Cables and connectors, 00 Series - Mini Coax.
- [19] Photonis,
Photomultiplier, XP3062, 8-stage, 40 mm hexagonal tube.
- [20] Saint-Gobain Ceramics & Plastics Inc.,
Optical Cement, BC-600.
- [21] Saint-Gobain Ceramics & Plastics Inc.,
Wavelength shifting fibre, BFC-99-29AMC.
- [22] Saint-Gobain Ceramics & Plastics Inc.,
Detector Assembly Materials, Optical Grease.
- [23] Technologic Systems Inc.,
Single Board Computer with CAN module: TS-7260 with TS-CAN1.
- [24] Texas Instruments Inc.,
Dual 10-bit DAC, TLV5617ACD.
- [25] Texas Instruments Inc.,
16/32-Bit RISC Flash Microcontroller (Rev. A), TMS470R1B1M.
- [26] Texas Instruments Inc.,
16/32-Bit RISC Flash Microcontroller (Rev. F) , SM470R1B1M-HT.
- [27] Texas Instruments Inc.,
DAC, TLV5630IPW.
- [28] Uni-Trend Group Ltd.,
Digital Multimeter UNI-T UT61B.
- [29] Voltcraft,
VOLTCRAFT R-200 Milliohm Meter.

List of Software

- [s1] in cooperation with Almela, A. and Kolotaev, Y.,
*AMIGA CPLD firmware for trigger synchronisation
for the auxiliary board SBC*, 2011.
- [s2] in cooperation with Dehn, C.
AMIGA connectivity firmware for the microcontroller, 2011.
- [s3] in cooperation with Fröhlich, U., Kolotaev, Y., Szadkowski, Z., and Wainberg, O.
*AMIGA DAQ firmware
for the FPGA of the underground readout electronics*, 2009.
- [s4] in cooperation with Fröhlich, U., Kolotaev, Y., Szadkowski, Z., and Wainberg, O.
*AMIGA DAQ firmware
for the FPGA of the underground readout electronics*, 2012.
- [s5] in cooperation with Kolotaev, Y.
revised modifications [s7] with stabilised signal outputs, 2012.
- [s6] in cooperation with Videla, M.
*AMIGA DAQ firmware
for the microcontroller of the underground readout electronics*, 2012.
- [s7] Wainberg, O.
*modifications on the standard DAQ firmwares
of the LS electronics for the SD stations*, 2010.

Bibliography

- [Abb08] Abbasi, R. U. et al. (The HiRes Collaboration), *First Observation of the Greisen-Zatsepin-Kuzmin Suppression*, Physical Review Letters **100** (2008), no. 10, 101101.
- [Abr04] Abraham, J. et al. (The Pierre Auger Collaboration), *Properties and performance of the prototype instrument for the Pierre Auger Observatory*, Nuclear Instruments and Methods in Physics Research A **523** (2004), 50–95.
- [Abr08a] ———, *Observation of the Suppression of the Flux of Cosmic Rays above 4×10^{19} eV*, Phys. Rev. Lett. **101** (2008).
- [Abr08b] ———, *Upper Limit on the Cosmic-Ray Photon Flux Above 10^{19} eV using the Surface Detector of the Pierre Auger Observatory*, Astropart.Phys. **29:243-256,2008** (2008).
- [Abr10a] ———, *Measurement of the energy spectrum of cosmic rays above 10^{18} eV using the Pierre Auger Observatory*, Physics Letters B **685** (2010), 239–246.
- [Abr10b] ———, *The fluorescence detector of the Pierre Auger Observatory*, Nuclear Instruments and Methods in Physics Research Section A: Accelerators, Spectrometers, Detectors and Associated Equipment **620** (2010), 227–251.
- [Abr10c] ———, *Trigger and aperture of the surface detector array of the Pierre Auger Observatory*, Nuclear Instruments and Methods in Physics Research Section A: Accelerators, Spectrometers, Detectors and Associated Equipment **613** (2010), no. 1, 29–39.
- [Abr10d] Abreu, P. et al. (The Pierre Auger Collaboration), *Update on the correlation of the highest energy cosmic rays with nearby extragalactic matter*, Astroparticle Physics **34** (2010), 314–326.
- [Abr11] ———, *The exposure of the hybrid detector of the Pierre Auger Observatory*, Astroparticle Physics **34** (2011), 368–381.
- [Ada07] Adam, T. et al., *The OPERA experiment Target Tracker*, Nuclear Instruments and Methods in Physics Research A **577** (2007), 523–539.
- [Agi12] Agilent Technologies, Inc., *Agilent 34980A Multifunction Switch/Measure Unit - Service Guide*, May 2012, Third Edition.

- [All06] Allard, D. et al., *A guide-line to the Auger-Surface-Detector Analysis*, Auger Internal Note **GAP-2006-024** (2006).
- [All07] Allard, D., Parizot, E. and Olinto, A. V., *On the transition from galactic to extragalactic cosmic-rays: Spectral and composition features from two opposite scenarios*, *Astroparticle Physics* **27** (2007), 61–75.
- [All08] Allekotte, I. et al. (The Pierre Auger Collaboration), *The surface detector system of the Pierre Auger Observatory*, *Nuclear Instruments and Methods in Physics Research A* **586** (2008), 409–420.
- [All11] Allison, P. for the Pierre Auger Collaboration, *Microwave detection of cosmic ray showers at the Pierre Auger Observatory*, *Proceedings of the 32nd Int. Cosmic Ray Conf.*, Beijing, China (2011).
- [Ant05] Antoni, T. et al. (The KASCADE Collaboration), *KASCADE measurements of energy spectra for elemental groups of cosmic rays: Results and open problems*, *Astroparticle Physics* **24** (2005), 1–25.
- [Ask65] Askaryan, G. A., *Soviet Physics JETP* **21** (1965), 988.
- [Aub11] Aublin, A. et al., *Evidence for a GHz emission from air-showers*, Auger Internal Note **GAP-2011-082** (2011).
- [Aug39] Auger, P. et al., *Extensive Cosmic-Ray Showers*, *Reviews of Modern Physics* **11** (1939), 288–291.
- [Aug06] Proposal by the Auger Assessment Committee, *AMIGA - Auger Muons and Infill for the Ground Array - Design Report*, (2006).
- [Aut12] Autolt Consulting Ltd., *autoit Automation and Scripting Language*, v3.3.6.1, August 2012, <http://www.autoitscript.com/>.
- [Ave07] Ave, M. et al. for the Pierre Auger Collaboration, *The accuracy of signal measurement with the water Cherenkov detectors of the Pierre Auger Observatory*, *Nuclear Instruments and Methods in Physics Research A* **578** (2007), 180–184.
- [Ben09] BenZvi, S., *Atmospheric Monitoring and its Use in Air Shower Analysis at the Pierre Auger Observatory*, *Proceedings of the 31st Int. Cosmic Ray Conf.*, Lodz, Poland (2009).
- [Ber07a] Berezinsky, V., *Transition from galactic to extragalactic cosmic rays*, *Proceedings of the 30th Int. Cosmic Ray Conf.*, Merida, Mexico (2007).
- [Ber07b] Bergman, D. R. and Belz, J. W., *TOPICAL REVIEW: Cosmic Rays: The Second Knee and beyond*, *Journal of Physics G Nuclear Physics* **34** (2007), 359.
- [Ber12] Beringer, J. et al. (Particle Data Group), *The Review of Particle Physics*, *Phys. Rev. D* **86** (2012), 010001, <http://pdg.lbl.gov/>.
- [Bha37] Bhabha, H. J. and Heitler, W., *The Passage of Fast Electrons and the Theory of Cosmic Showers*, *Royal Society of London Proceedings Series A* **159** (1937), 432–458.

- [Bir94] Bird, D. J. et al., *The cosmic-ray energy spectrum observed by the Fly's Eye*, *Astrophysical Journal* **424** (1994), 491–502.
- [Blu09] Bluemer, J., Engel, R. and Hörandel, J. R., *Cosmic rays from the knee to the highest energies*, *Progress in Particle and Nuclear Physics* **63** (2009), 293–338.
- [Bor04] Borer, K. and Wälchi, T., *Hamamatsu H8804MOD-1 multi anode PMT tests for OPERA*, University of Bern (2004), http://www.lhep.unibe.ch/opera/pm_test/pm_test.pdf.
- [Bot29] Bothe, W. and Kolhörster, W., *Das Wesen der Höhenstrahlung*, *Zeitschrift für Physik* **56** (1929), 751–777.
- [Bro12] Bronger, T., *Python GPIB etc. support with PyVISA, v1.3*, August 2012, <http://pyvisa.sourceforge.net/>.
- [Buc09] Buchholz, P. for The Pierre Auger Collaboratioin, *Hardware Developments for the AMIGA enhancement at the Pierre Auger Observatory*, Proceedings of the 31st Int. Cosmic Ray Conf., Lodz, Poland (2009).
- [Con10] Contreras, F., *private communication*, Malargüe (2010).
- [Con11] Conceição, R. et al. (The Pierre Auger Collaboration), *Results from the Pierre Auger Observatory*.
- [Con12a] PC/104 Consortium, *The PC/104 Bus System*, 2012, <http://www.pc104.org/>.
- [Con12b] Contreras, F., *private communication*, Malargüe (2012).
- [Cou11] Coutu, S., *Auger South Google Earth model*, downloaded in 2011, http://www.phys.psu.edu/~coutu/ge_models.htm.
- [Cow98] see e.g. Cowan, G. and references therein, *Statistical Data Analysis*, Oxford Science Publications, 1998.
- [Cro97] Cronin, J., Watson, A., *The Pierre Auger Observatory Design Report*, Tech. report, March 1997.
- [Dem12] Dembinski, H. et al., *The Auger Observer*, 2012, <http://augerobserver.fzk.de>.
- [Erl97] Erlykin, A. D. and Wolfendale, A. W., *A single source of cosmic rays in the range 10^{15} - 10^{16} eV*, *Journal of Physics G Nuclear Physics* **23** (1997), 979–989.
- [Etc10] Etchegoyen, A. et al. for The Pierre Auger Collaboration, *The Pierre Auger Project and Enhancements*, Proceedings of the 8th Latin American Symposium on Nuclear Physics and Applications, Santiago, Chile (2010).
- [Fro09] Froehlich, F., *Charakterisierung der Szintillatoren und der Ausleseelektronik des AMIGA-Myonsystems*, Master's thesis, Universität Siegen, Siegen, 2009.

- [Fro13] _____, *Studies of Hardware Components, Firmware Development and First Data of the AMIGA Muon Detectors for the Pierre Auger Observatory*, Ph.D. thesis, Universität Siegen, Siegen, 2013.
- [Gei28] Geiger, H. and Müller, W., *Elektronenzählrohr zur Messung schwächster Aktivitäten*, *Naturwissenschaften* **16** (1928), 617–618.
- [Goc10] Gockel, A., *Air electrical observations in a balloon journey*, *Phys. Zeit.* **11** (1910), 280–282.
- [Goo11] Google Earth, <http://earth.google.com>, information copied in 2011.
- [Gre56] Greisen, K., *Progress in cosmic ray physics*.
- [Gre66] _____, *End to the cosmic-ray spectrum?*, *Phys. Rev. Lett.* **16** (1966), 748.
- [Gri10] see e.g. Grieder, K. F. (and references therein), *Extensive Air Showers, High Energy Phenomen and Astrophysical Aspects*, vol. I, Springer Verlag Berlin Heidelberg, corrected 2nd printing 2010.
- [Gru93] see e.g. Grupen, C. (and references therein), *Teilchendetektoren*, BI-Wissenschaftsverlag, Mannheim, 1993.
- [Gru05] _____, *Astroparticle Physics*, Springer Verlag, Berlin, Germany; New York, U.S.A., 2005.
- [Gua11] Guardincerri, Y. for The Pierre Auger Collaboration, *The Pierre Auger Observatory and ultra-high energy neutrinos: upper limits to the diffuse and point source fluxes*, ICRC 2011 (2011).
- [Hes12] Hess, V. F., *Über Beobachtungen der durchdringenden Strahlung bei sieben Freiballonfahrten*, *Physikalische Zeitschrift* **13** (1912), 1084–1091.
- [Hof25] Hoffmann, G., *Measurements of penetrating radiation at sea level*, *Phys. Zeit.* **26** (1925), 669–672.
- [IVI12] IVI Foundation, *Standard Commands for Programmable Instrumentation (SCPI)*, August 2012, <http://www.ivifoundation.org>.
- [Kam58] Kamata, K. and Nishimura, J., *The Lateral and the Angular Structure Functions of Electron Showers*, *Progress of Theoretical Physics Supplement* **6** (1958), 93–155.
- [Kam04] Kampert, K. H. et al. (The KASCADE-Grande Collaboration), *Cosmic Rays in the 'Knee'-Region - Recent Results from KASCADE*, *Acta Phys. Polon. B* **35** (2004), 1799–1812.
- [Kam11] Kampert, K.-H. (The Pierre Auger Collaboration), *Highlights from the Pierre Auger Observatory*, Proceedings of the 32nd Int. Cosmic Ray Conf., Beijing, China (2011).
- [Kaz01] Kazanas, D. and Nicolaidis, A., *Cosmic Ray "Knee": A Herald of New Physics?*, Proceedings of the 27th Int. Cosmic Ray Conf., Hamburg, Germany (2001).

- [Kel11] Kelley, J. L. for The Pierre Auger Collaboration, *AERA: the Auger Engineering Radio Array*, Proceedings of the 32nd Int. Cosmic Ray Conf., Beijing, China (2011).
- [Kic08] Kickelbick, D., *The energy spectrum of primary cosmic rays measured with the KASCADE-Grande experiment*, Ph.D. thesis, Universität Siegen, 2008.
- [Kob08] Kobayakawa, K., Sato, Y. and Samura, T., *Acceleration by oblique shocks at supernova remnants and cosmic ray spectra around the knee region*, Phys. Rev. D **66** (2002, last update 2008), no. 8, 083004.
- [Kol14] Kolhörster, W., *Messungen der durchdringenden Strahlungen bis in Höhen von 9300 m*, Verhandlungen der DPG **16** (1914), 719.
- [Kol12] Kolotaev, Y., *private communication*, Siegen, 2008 - 2012.
- [Lan53] Landau, L. D. and Pomeranchuk, I. J., Dokl. Akad. Nauk SSSR **92** (1953), 535, 735.
- [Lau12] Lauber, F., *Aufbau eines Myon-Hodoskops für den AMIGA-Teststand*, Universität Siegen, 2012.
- [LEM12] LEMO S.A., *00 Series - Mini Coax*, August 2012, <http://www.lemo.ch>.
- [Lin04] Linke, F., *Luftelektrische Messungen bei zwölf Ballonfahrten*, Abhandlungen der Königlichen Gesellschaft der Wissenschaften Göttingen **3** (1904), [Nachdr. der Ausg.] Berlin, 1904, Verlag Kraus, Nendeln/Liechtenstein, 1971.
- [Lin63] Linsley, J., *Evidence for a Primary Cosmic-Ray Particle with Energy 10^{20} eV*, Physical Review Letters **10** (1963), 146–148.
- [Lon92] see e.g. Longair, M. S. (and references therein), *High Energy Astrophysics*, vol. 1, Cambridge University Press, Second Edition 1992.
- [Mal12] Maldera, S., *private communication*, 2012.
- [Man12] Mantsch, P. and the AMIGA Review Teams, *AMIGA Review Summary Report*, Auger Internal Note, 2012.
- [Mar06] Maris, I. C. et al., *Data Summary Trees and Shower Visualization for Reconstructed Auger Events*, Auger Internal Note **GAP-2006-081** (2006).
- [Mar11] Maris, I. C. for The Pierre Auger Collaboration, *The AMIGA infill detector of the Pierre Auger Observatory: performance and first data*, Proceedings of the 32nd Int. Cosmic Ray Conf., Beijing, China (2011).
- [Mat01] Matthews, J., *Energy Flow in Extensive Air Showers*, Proceedings of the 27th Int. Cosmic Ray Conf., Hamburg, Germany (2001), 261.
- [Mat05] ———, *A Heitler model of extensive air showers*, Astroparticle Physics **22** (2005), 387–397.

- [Mat11] Mathes, H.-J. M. for the Pierre Auger Collaboration, *The HEAT Telescopes of the Pierre Auger Observatory Status and First Data*, ICRC 2011 (2011).
- [Mig56] Migdal, A. B., *Phys. Rev.* **103** (1956), 1811.
- [Nie11] Niechciol, M., *Muon counter simulation studies for the AMIGA enhancement of the Pierre Auger Observatory*, Master's thesis, Universität Siegen, 2011.
- [Pac10] Pacini, D., *Penetrating Radiation at the Surface of and in Water*, *Nuovo Cimento VI* **3** (2010), 93.
- [Pla11] Platino, M. et al., *AMIGA at the Auger Observatory: the scintillator module testing system*, *Journal of Instrumentation* **6** (2011), 6006.
- [Pon11] Pontz, M., *AMIGA System Tests - Instructions*, Internal Publication, Universität Siegen, 2011.
- [Pyt12] Python Software Foundation, *Python Programming Language, v2.6.6 and Python's Integrated Development Environment IDLE, v2.6.6*, August 2012, <http://www.python.org/>.
- [Rau12] Rautenberg, J., *Auger Monitoring*, 2012, <http://paomon.physik.uni-wuppertal.de/>.
- [Ros11] Ros, G. et al., *A new composition-sensitive parameter for ultra-high energy cosmic rays*, *Astroparticle Physics* **35** (2011), 140–151.
- [Rot08] Roth, M., *Measurement of the UHECR Energy Spectrum using data from the Surface Detector of the Pierre Auger Observatory*, *Proceedings of the 30th Int. Cosmic Ray Conf., Merida, Mexico* **4** (2008), 327–330.
- [San12] Sanchez, F. et al., *The AMIGA extension of Auger Offline Software*, *Auger Internal Note* **GAP-2012-135** (2012).
- [Sch32] Schmidt, B., *Ein lichtstarkes komafreies Spiegelsystem*, *Mitteilungen der Hamburger Sternwarte in Bergedorf* **56.7** (1932), 15–17.
- [Set11] Settimo, M. for The Pierre Auger Collaboration, *An update on a search for ultra-high energy photons using the Pierre Auger Observatory*, *Proceedings of the 32nd Int. Cosmic Ray Conf., Beijing, China* (2011).
- [Set12] Settimo, M., *private communication*, Siegen, October 2012.
- [Sid12] Sidelnik, I. et al., *Deployment of 10 m² muon counter modules of the AMIGA Pre-Unitary Cell*, *Auger Internal Note* **GAP-2012-079** (2012).
- [Sok10] Sokolsky, P. et al., (The HiRes Collaboration), *Final Results from the High Resolution Fly's Eye (HiRes) Experiment*, Invited paper of the XVI International Symposium on Very High Energy Cosmic Ray Interactions ISVHECRI 2010, Batavia, IL, USA, arXiv:1010.2690v2 [astro-ph.HE] (2010).
- [Sua09] Suarez, F. et al., *Multi-pixel PMTs for the AMIGA project. Proposal for the testing facility and first measurements*, *Auger Internal Note* **GAP-2008-164** (2009).

-
- [Sza09a] Szadkowski, Z., *Triggers, data flow and the synchronization between the Auger surface detector and the AMIGA underground muon counters*, Proceedings of the 31st Int. Cosmic Ray Conf., Lodz, Poland (2009).
- [Sza09b] Szadkowski, Z. et al, *The 3rd generation Front-End cards of the Pierre Auger surface detectors: Test results and performance in the field*, Nuclear Instruments and Methods in Physics Research A **606** (2009), 439–445.
- [Tat12] Tatham, S., *PutTY: A Free Telnet/SSH Client*, August 2012, <http://www.putty.org>.
- [Tex05] Texas Instruments Inc., *TMS470R1x Multi-Buffered Analog-to-Digital Converter Reference Guide (spnu206c)*, September 2005.
- [Tig11] Tigges, M., *Systemtests der Ausleseelektronik der AMIGA-Erweiterung des Pierre-Auger-Observatoriums*, Master's thesis, Universität Siegen, Siegen, 2011.
- [Ull07] Ullrich, T. et al., *Treatment of Errors in Efficiency Calculations*, eprint (2007), arXiv:physics/0701199.
- [Veb09] Veberic, D. and Roth, M. et al., *Offline Reference Manual - SD Reconstruction, Rev. 8863*, Auger Internal Note (2009), based on GAP-2005-035.
- [Vé12] Véron-Cetty, M. P., Véron, P., *Astron. Astrophys.* **455** (2012), 773.
- [Wai11] Wainberg, O., *private communication*, September 2011.
- [Wal12a] Walter, M. (and references therein), *Ein Höhenflug der Physik*, *Physik Journal* **6** (2012), 53–57.
- [Wal12b] Walter, M. and Wolfendale, A.W., *Early history of cosmic particle physics*, *Eur. Phys. J. H* (2012).
- [You07] Younk, P. W., *Cosmic Rays at the Ankle - Composition Studies Using the Pierre Auger Observatory*, Phd thesis, Michigan Technological University, Houghton, Michigan, 2007.
- [Zat66] Zatsepin, G. T. and Kuz'min, V. A., *Upper limit of the spectrum of cosmic rays*, *Sov. J. Exp. Theor. Phys. Lett.* **4** (1966), 78.

Acknowledgements

There are many people who supported me while I was preparing and writing my thesis and to whom I am deeply indebted to. What follows is the attempt to set up a list of those people.

First of all, I would like to thank my supervisor Prof. Dr. Peter Buchholz for giving me the opportunity to do my PhD in Astroparticle Physics at the University of Siegen. Thank you for arranging several stays at the Pierre Auger Observatory in Argentina, for letting me do outreach work and teaching and finally for your overall support and continuing faith in me.

Further, I would like to thank Prof. Dr. Markus Risse for co-reviewing the thesis and for his constant willingness for help and discussions.

Thanks to Prof. Dr. Claus Grupen and Prof. Dr. Thomas Mannel for their immediate will to join the PhD board.

Special thanks deserves the working group for Particle and Astroparticle Physics for having such a friendly working atmosphere.

In particular I would like to mention Hendrik Czirr for sharing the office with me during the past four years; Uwe Fröhlich, thank you not only for the numerous discussions but also for the lots of funny moments we shared; Marcus Niechciol, many thanks for proofreading the thesis, for your patience and criticism; Dr. Mariangela Settimo, thanks for the various constructive discussions and good advises; Dr. Rodica Tcaciuc, thanks for your cooperation; Dr. Wolfgang Walkowiak, thanks for providing the computing environment and for your open ear for problems related with it; and Yury Kolotaev, thanks for having answers to all of my questions concerning electronics. I enjoyed working together with “my” students, Christian Dehn, Sebastian Keckert, Frederik Lauber, Sebastian Sonntag and Martin Tigges; further on good luck to you!

To the members of the electronics and the mechanical workshop of the Physics Department of the University of Siegen, thank you for your support and good advise whenever requested. Thank you Dr. Ulrich Werthenbach for your help in setting up one of our test stands and for your time for discussions.

I enjoyed to get to know so many nice people within the Pierre Auger Collaboration during conferences, schools and professional visits.

I would like to express my gratitude to the local staff of the Pierre Auger Observatory for your friendly support during all my stays in Malargüe and for your patience in my attempts to learn the Spanish language.

Thanks to my colleagues from Bariloche, Buenos Aires, Malargüe and Mendoza for

Acknowledgements

your collaboration; in particular, I would like to mention Dr. Ingomar Allekotte, Fernando Contreras, Dr. Alberto Etchegoyen, Dr. Beatrice García, Dr. Manuel Platino, Dr. Federico Sánchez, Dr. Ricardo Sato, Gonzalo A. de la Vega, Mariela Videla and Oscar Wainberg.

Thanks to Prof. Dr. Zbigniew Szadkowski from Łódź for collaborating on large parts of the FPGA firmware.

I wish to extend my thanks to the hotel staff around Mauricio Flores Ruminot of my favourite hotel in Malargüe. You were aiming to make my stays overseas comfortable and gave me the opportunity to talk non-physics from time to time. Thank you.

And last but not least: Cordial thanks to my family and friends for your encouraging backing during all phases of preparing and writing of the thesis, especially during the last stressful months. In particular I would like to express my appreciation to my grandmother Anneliese, to my mother Gisela and to my siblings Tobias and Stefanie for their continuous belief in me.

Thank you Ann-Christin, for sharing your life with me, thanks for your belief, trust and love! You and our son Paul were the greatest motivation to finish the thesis, it would have been impossible without you.

Thank you all!

Erratum:

System Tests, Initial Operation and First Data of the AMIGA Muon Detector for the Pierre Auger Observatory,

M. Pontz, Universität Siegen, Siegen, 2012.

An update of the analysis software in June 2013 and its application to the initial dataset results in Figure 6.25. Before the update, about every second event was accidentally skipped in the analysis. This results in a random choice of 50 % of all muon detector (MD) events. Since this cut was not applied to the surface detector (SD) data, about 50 % of these lacked their equivalent in the MD data. After the software update, almost all SD events have their equivalent in the MD data. This is a proof and a consequence of the correct functionality of the trigger processing and the event identification algorithms of the MD data acquisition software.

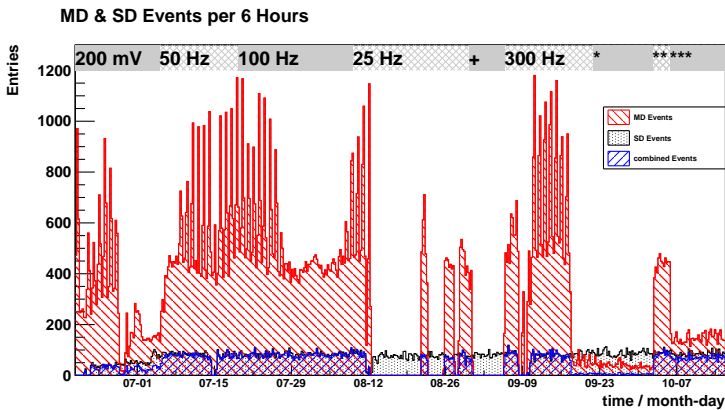


Figure 6.25: Updated analysis. Number of recorded events per six hours for the SD (black dotted area) and for the MD (red hatched area, see legend). Events that were recorded in the same GPS second are drawn as combined events (blue hatched area, see legend).

Further, values of the newly defined MD observable N_{Trig} were partly underestimated due to a misinterpretation of 64 bit long integer values with the most significant bit being set. This effect does not prefer any range of values in N_{trig} but is homogeneously distributed in the full range. Therefore, no significant impact on the correlation calculation as presented in Section 6.6.8 is expected. Updated versions of the Figures 6.29 through 6.32 are shown below.

One of the main parts of the analysis is the investigation of correlation between the signal strengths $S_{LDF}(r)$ in the SD station and N_{Trig} in the associated MD module. The results of this analysis can be found in Tables 6.6 and 6.5. The analysis was repeated with the increased statistics and the updated analysis software. In agreement with the expectation, the updated results do not differ significantly from the earlier ones. In particular, the correlation between the signal strength N_{Trig} for the MD module and the azimuth angle of the incoming air shower, as derived from the SD event reconstruction, remains compatible with zero, whereas the correlation between N_{Trig} and the reconstructed signal strength $S_{LDF}(r)$ at the position of the SD station stays the same.

I would like to express my gratitude to my colleague Dr. Uwe Fröhlich for his collaboration on the update of the analysis software.

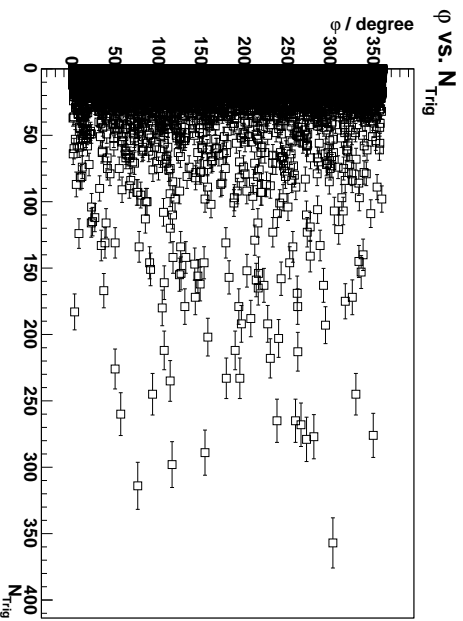


Figure 6.29: Updated analysis. Scatter plot of the two observables N_{Trig} and ϕ . The azimuth angle ϕ covers all possible values between 0 and 2π isotropically.

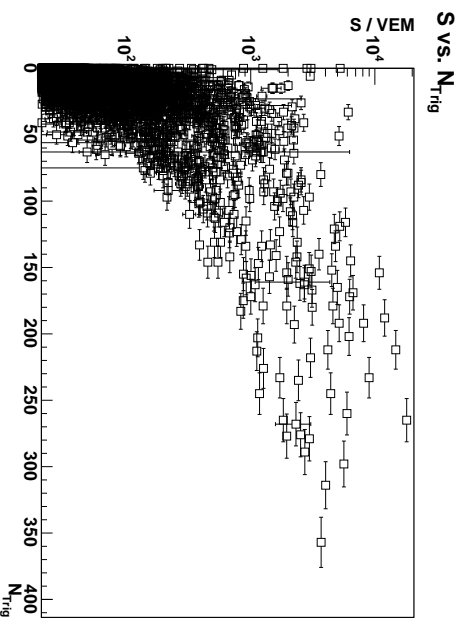


Figure 6.31: Updated analysis. Scatter plot of the two observables N_{Trig} and $S_{LDF}(r)$.

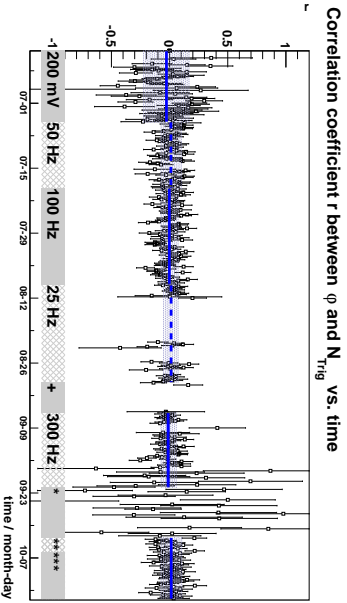


Figure 6.30: Updated analysis. Correlation coefficient r_ϕ between ϕ and N_{Trig} in bins of six hours. The uncertainties are calculated as explained in the thesis. Different measurement and maintenance periods are shown according to Table 6.4. The weighted means are compatible with zero, which is in agreement with the expectation.

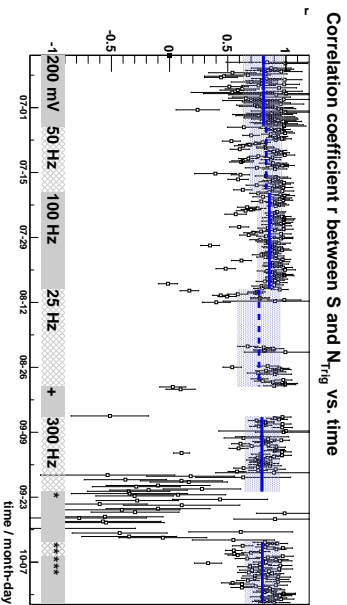


Figure 6.32: Updated analysis. Correlation coefficient r_S between $S_{LDF}(r)$ and N_{Trig} in bins of six hours. The uncertainties are calculated as explained in the text. Different measurement and maintenance periods are shown according to Table 6.4.